

UNIVERSITY OF OKLAHOMA

GRADUATE COLLEGE

PETROPHYSICAL INVERSION OF MULTIFREQUENCY RESISTIVITY AND  
PERMITTIVITY LOGS AND LABORATORY MEASUREMENTS

A THESIS

SUBMITTED TO THE GRADUATE FACULTY

in partial fulfillment of the requirements for the

Degree of

MASTER OF SCIENCE

By

YIFU HAN  
Norman, Oklahoma  
2017

PETROPHYSICAL INVERSION OF MULTIFREQUENCY RESISTIVITY AND  
PERMITTIVITY LOGS AND LABORATORY MEASUREMENTS

A THESIS APPROVED FOR THE  
MEWBOURNE SCHOOL OF PETROLEUM AND GEOLOGICAL ENGINEERING

BY

---

Dr. Siddharth Misra, Chair

---

Dr. Chandra S. Rai

---

Dr. Deepak Devegowda



*Dedicate to my dear mom and dad who gave me countless love and support.*

## **Acknowledgements**

First and the most, I would like to express my heartiest gratitude to my academic advisor, Dr. Siddharth Misra. Without his patient guidance and assistance, it would have been impossible for me to work on petrophysics and inversion algorithm.

I would like to thank Dr. Chandra S. Rai and Dr. Devegowda Deepak, the members of my thesis committee, for shaping the course of my graduate program. I greatly appreciate their time in reviewing this work and making valuable suggestions and comments.

I would also like to thank Hess Corporation and Chevron for providing me data and guidance to accomplish my research objectives.

Finally, I would like to thank my parents, Qi Han and Wenli Yu, for their constant support, which gives me courage. Throughout the last two years, they helped me focus on my research. Their unfailing support is exactly what I needed to accomplish my Master of Science degree at University of Oklahoma.

# Table of Contents

Acknowledgements .....	iv
List of Tables .....	vii
List of Figures.....	ix
Abstract.....	xiv
Chapter 1: Introduction.....	1
1.1    Motivation and problem statement.....	1
1.2    Objective of this study.....	3
1.3    Organization of thesis.....	3
Chapter 2: Literature Review .....	5
2.1    Dispersive EM properties, laboratory measurements and relaxation models	5
2.2    Broadband EM dispersion log.....	7
2.3    EM dispersion log interpretation models .....	8
Chapter 3: Unified Inversion Scheme of Various Relaxation Models.....	10
3.1    Introduction of polarization and relaxation models.....	10
3.2    Relaxation models of characterizing polarization mechanisms .....	11
3.3    Literature review of inversion using relaxation models.....	12
3.4    Improved bounded Levenberg inversion algorithm .....	14
3.5    Synthetic cases validation.....	23
3.6    Inversion of laboratory EM measurement .....	26
Chapter 4: Joint Broadband Conductivity and Permittivity Logs Inversion .....	33
4.1    Introduction to different EM log tools and limitation of this work.....	33
4.2    Literature review of EM log inversion .....	34

4.3	Modified Levenberg-Marquardt inversion algorithm .....	36
4.4	Synthetic case study .....	41
4.5	Application in organic-rich gas shale formation .....	52
Chapter 5: Dielectric Dispersion Log Interpretation in Bakken Petroleum System .....		59
5.1	Inconsistent water saturation in the Bakken Petroleum System.....	59
5.2	Dielectric dispersion log interpretation models.....	60
5.3	Modified Levenberg-Marquardt inversion algorithm .....	62
5.4	Synthetic case study .....	66
5.5	Application in Bakken Petroleum System.....	70
5.6	Validation of inversion-derived estimates.....	82
Chapter 6: Conclusion .....		91
References .....		93
Appendix: Nomenclature.....		99

## List of Tables

Table 3.1 The inversion-derived estimates of Havrilak-Negami model, Cole-Cole model and dual Cole-Cole model parameters for inversion of synthetic dispersive data.....	24
Table 3.2 Inversion-derived estimates of dual Cole-Cole model parameter required to fit synthetic resistivity data containing various levels of Gaussian noise .....	26
Table 3.3 Dual Cole-Cole resistivity model estimates for the silica-sand sample obtained using our proposed inversion method and those obtained by Chen et al. (2008) .....	32
Table 4.1 Assumed petrophysical properties of the three synthetic layers used for this study. The parameters shown with a gray background were also used as the inversion-derived estimates .....	42
Table 4.2 Relative errors in water saturation estimates obtained using the joint inversion of multifrequency conductivity and permittivity data containing 5% Gaussian noise for three synthetic layers .....	51
Table 4.3 Relative errors in brine conductivity estimates obtained using the joint inversion of multifrequency conductivity and permittivity data containing 5% Gaussian noise for three synthetic layers .....	51
Table 4.4 Relative errors in clay surface conductance estimates obtained using the joint inversion of multifrequency conductivity and permittivity data containing 5% Gaussian noise for three synthetic layers .....	52
Table 4.5 Relative errors in clay radius estimates obtained using the joint inversion of multifrequency conductivity and permittivity data containing 5% Gaussian noise for two synthetic layers .....	52



Table 4.6 Relative errors in pyrite radius estimates obtained using the joint inversion of multifrequency conductivity and permittivity data containing 5% Gaussian noise for one synthetic layer .....	52
Table 4.7 Inversion-derived and assumed petrophysical properties of two depths in the organic-rich formation. Joint inversion of induction, propagation and dielectric dispersion logs was performed at the two depths. The five inversion-derived estimates are shown with a gray background .....	54
Table 4.8 Estimated petrophysical properties and data misfit in depth XX52 m in an organic-rich formation when performing petrophysical inversion of various combinations of logging tools .....	56
Table 4.9 Estimated petrophysical properties and data misfit in depth XX09 m in an organic-rich formation when performing petrophysical inversion of various combinations of logging tools .....	56
Table 5.1 Assumed physical properties of the Synthetic Formation 1. Inversion was performed to estimate the parameters highlighted in grey .....	67
Table 5.2 Assumed physical properties of the Synthetic Formation 2. Inversion was performed to estimate the parameters highlighted in grey .....	69
Table 5.3 Inversion results of Synthetic Case 2 without 5% Gaussian noise by using different values of radius of spherical clay grains and surface conductance of clay .....	79

## List of Figures

Figure 3.1 Flowchart of the unified inversion scheme .....	18
Figure 3.2 Flowchart of the jump back-in step.....	21
Figure 3.3 Flowchart of the jump out step for the first reflection .....	22
Figure 3.4 Convergence of estimates of relaxation-model parameters and error as a function of iteration for inversion of multi-frequency measurement of complex permittivity .....	28
Figure 3.5 Comparisons of real and imaginary permittivity measurements on poly (methyl acrylate) solution reported by Havriliak and Negami (1966) against the Havriliak-Negami relaxation model predictions based on the estimated parameters .....	29
Figure 3.6 Convergence of parameter estimates and error as a function of iteration for inversion of multi-frequency measurement of complex resistivity of an unconsolidated silica-sand sample, published by Kemna et al. (2000) .....	30
Figure 3.7 Comparison of multi-frequency measurements of real and negative imaginary resistivity of an unconsolidated silica-sand sample against dual Cole-Cole model predictions based on inversion estimates .....	31
Figure 4.1 Synthetic data with and without 5% Gaussian noise at one laterolog (~Hz), two induction (~kHz), two propagation (~MHz), and four dielectric frequencies (~MHz to 1 GHz) generated assuming parameters for Synthetic Layer 1 .....	44
Figure 4.2 Changes in (A) water saturation and brine conductivity estimates and those in (B) surface conductance of clay and radius of spherical clay with associated relative error of data misfit obtained during the modified LMA-based inversion of synthetic data shown in Fig. 4.1 (representing the conductivity and permittivity response of Synthetic Layer 1).	

The dash line identifies the estimates generated by the modified LMA. The start point for both the methods is  $S_w = 0.5$ ,  $C_w = 7$  S/m,  $\lambda_c = 5 \times 10^{-7}$  S,  $r_c = 0.2 \mu\text{m}$ , and  $r_i = 50 \mu\text{m}$

Figure 4.3 Convergence of modified LMA-based inversion estimates of PS-model parameters and relative error (between modeled data based on the estimated parameters and the synthetic data) as a function of iteration during the inversion of synthetic data with 5% Gaussian noise generated for the Synthetic Layer 1. Inversion results for five different sets of initial guesses of the model parameters are shown in the figure.....46

Figure 4.4 Synthetic data with and without 5% Gaussian noise at one induction (~kHz) and four dielectric (~MHz to 1 GHz) frequencies generated assuming parameters of Synthetic Layer 3. Data at induction frequency does not have a corresponding relative permittivity value, in accordance with current practices in log acquisition ..... 49

Figure 4.5 Synthetic data with and without 5% Gaussian noise at two propagation (~MHz) and four dielectric (~MHz to 1 GHz) frequencies generated assuming parameters of Synthetic Layer 2..... 51

Figure 4.6 Comparison of broadband conductivity- and permittivity-dispersion measurements against those modeled using the inversion-derived estimates for depth XX09 m in the organic-rich shale formation..... 57

Figure 4.7 Comparison of broadband conductivity- and permittivity-dispersion measurements against those modeled using the inversion-derived estimates for depth XX52 m in the organic-rich shale formation..... 58

Figure 5.1 Convergence of inversion-derived estimates of unknown integrated model parameters and relative error as a function of iteration for the inversion of synthetic data

with 5% Gaussian noise generated for the Synthetic Formation 1 using the integrated model.....	67
Figure 5.2 Convergence of inversion-derived estimates of unknown integrated model parameters and relative error as a function of iteration for the inversion of synthetic data with 5% Gaussian noise generated for the Synthetic Formation 2 using the integrated model.....	69
Figure 5.3 Global-search modified-LMA inversion.....	71
Figure 5.4 Flow chart of the proposed dielectric-dispersion log interpretation method.....	72
Figure 5.5 Comparison of effective conductivity and permittivity measurements and model predictions for depth XX864 ft in Three Forks formation .....	73
Figure 5.6 Frequency of inversion-derived $S_w$ estimates for depth XX736 ft along with data misfit for 250 randomly generated sets of initial guesses of integrated model parameters.....	74
Figure 5.7 Frequency of inversion-derived $C_w$ estimates for depth XX736 ft along with data misfit for 250 randomly generated sets of initial guesses of integrated model parameters.....	75
Figure 5.8 Frequency of inversion-derived $m$ estimates for depth XX736 ft along with data misfit for 250 randomly generated sets of initial guesses of integrated model parameters.....	75
Figure 5.9 Frequency of inversion-derived $\alpha$ estimates for depth XX736 ft along with data misfit for 250 randomly generated sets of initial guesses of integrated model parameters.....	76

Figure 5.10 Comparison of effective conductivity and permittivity measurements and model predictions for depth XX736 ft in the Middle Bakken formation ..... 76

Figure 5.11 Comparison of effective conductivity and permittivity measurements and model predictions for depth XX874 ft in the Three Forks formation ..... 78

Figure 5.12 Frequency of inversion-derived  $S_w$  estimates for depth XX677 ft along with data misfit for 250 randomly generated sets of initial guesses of integrated model parameters..... 80

Figure 5.13 Frequency of inversion-derived  $C_w$  estimates for depth XX677 ft along with data misfit for 250 randomly generated sets of initial guesses of integrated model parameters..... 81

Figure 5.14 Frequency of inversion-derived  $S_w$  estimates for depth XX630.5 ft along with data misfit for 250 randomly generated sets of initial guesses of integrated model parameters..... 81

Figure 5.15 Frequency of inversion-derived  $S_w$  estimates for depth XX630.5 ft along with data misfit for 250 randomly generated sets of initial guesses of integrated model parameters..... 82

Figure 5.16 Track 1 is the depth, Track 2 contains the top and bottom of various formations in BPS, Track 3 is the gamma ray, Track 4 contains the neutron porosity, density porosity and ELAN total porosity, Track 5 is the induction resistivity in horizontal direction and formation anisotropy, Track 6 contains the volume fractions of various minerals, Track 7 contains the dielectric dispersion conductivity logs at four frequencies, Track 8 contains the dielectric dispersion permittivity logs at four frequencies, and Track 9 contains water saturation estimated using various methods, wherein the red curve is

water saturation estimate obtained using the proposed global-search inversion and the blue curve is that obtained by Schlumberger dielectric inversion..... 85

Figure 5.17 Track 1 contains the top and bottom of various formations in BPS, Track 2 is the depth, Track 3 contains water saturation estimated using various methods, wherein the red curve is water saturation estimate obtained using the proposed global-search inversion and the blue curve is that obtained by Schlumberger dielectric inversion, Track 4 is the formation water conductivity estimate and the black curve is that obtained by Schlumberger dielectric inversion, Track 5 is the inversion-derived homogeneity index, Track 6 is the formation homogeneity index calculated using mineral contents, Track 7 is the inversion-derived cementation index, Track 8 contains the permeability and isolated porosity (total-effective) of the formation, Track 9 is NMR T2 distribution..... 89

Figure 5.18 Track 1 contains the top and bottom of various formations in BPS, Track 2 is the depth, Track 3 contains estimated water saturation range within a desired accuracy, Track 4 is the range of estimated formation water conductivity, Track 5 is the range of estimated inversion-derived homogeneity index, Track 6 is the range of estimated cementation index, Track 7 contains the relative error of the inversion of field data using the integrated model and the relative error of the SMD and LR, respectively, Track 8 contains the total porosity and the ratio of effective porosity and total porosity of the formation, Track 9 is the formation homogeneity index calculated using mineral contents, Track 10 is NMR T2 distribution ..... 90

## **Abstract**

In this thesis, we develop a unified inversion scheme that can be coupled to various type of relaxation models to process multi-frequency measurement of varied electromagnetic (EM) properties for purposes of improved EM-based geomaterial characterization. The proposed inversion scheme is firstly tested in few synthetic cases in which different relaxation models are coupled with the inversion scheme. Then, the inversion is applied to multi-frequency complex resistivity and complex permittivity measurements acquired in laboratory and in subsurface borehole environments. For purposes of inversion of laboratory-based EM measurements, the unified inversion scheme estimates up to seven relaxation-model parameters exhibiting convergence and accuracy for random initializations of the relaxation-model parameters within up to 3-orders of magnitude variation around the true parameter values. The inversion-derived estimates of relaxation-model parameters can be used for materials characterization.

The inversion scheme is then improved for purposes of joint petrophysical inversion of multifrequency effective electrical conductivity and dielectric permittivity logs derived from various combinations of downhole EM logs acquired in clay- and pyrite-rich shale formations at multiple frequencies. The proposed joint interpretation method uses a single mechanistic model that accounts for the IP effect arising from clay and conductive mineral grains; thereby generating physically consistent water saturation estimates in shales. The proposed inversion-based interpretation also generates estimates of formation water salinity, surface conductance of clay, and average radius of clay and conductive mineral grains. The proposed method is firstly applied to three synthetic geological formations, with varying clay type, conductive mineral properties, and water

saturation. Then the joint petrophysical inversion algorithm is applied to field broadband dispersion EM data acquired in a European Lower Paleozoic organic-rich shale formation.

Finally, the inversion-based joint petrophysical interpretation is implemented for processing dielectric dispersion logs acquired in Bakken Petroleum System acquired at four discrete frequencies in the range of 10 MHz – 1 GHz. The newly developed interpretation method is applied to process the dielectric dispersion log acquired in Bakken formation to estimate water saturation, formation salinity, cementation index and homogeneity index. Water saturation estimates for a specific depth obtained using the proposed interpretation method is not one single value but a range of possible values within a desired accuracy. These water saturation estimates were compared against those obtained from resistivity induction log, NMR log, Quanti-ELAN solver, service company's dielectric inversion, and Dean-Stark core measurements. Our estimates of water saturation and those obtained using the service company's dielectric inversion exhibit best match with Dean-Stark's core water saturation in Middle Bakken and Three Forks formations. The estimated water salinity is very high which agrees with core measurements. Homogeneity index obtained using our method indicates the presence of layering and heterogeneity in Lower Three Forks and Middle Bakken. The cementation index indicates high tortuosity and cementation in Upper and Lower Bakken.



## **Chapter 1: Introduction**

This thesis presents work performed for a Master of Science degree that was conducted at Mewbourne School of Petroleum and Geological Engineering of the University of Oklahoma. The research presented herein develops inversion schemes to process the resistivity and permittivity laboratory measurements and logs. The petrophysical properties of formations or laboratory samples can be characterized or estimated. The following sections present the motivation and problem statement, objective, and organization of this thesis.

### **1.1 Motivation and problem statement**

Multi-frequency laboratory measurement of a dispersive electromagnetic (EM) property, such as electrical conductivity, dielectric permittivity, or magnetic permeability, is commonly analyzed for purposes of material characterization. Such an analysis requires inversion of the multi-frequency measurement based on a specific relaxation model, such as Cole-Cole model or Pelton's model. In doing so, the estimated parameters of the relaxation model serve as characteristics/identifiers of the geomaterial. Although there are several published methods for deterministic inversion of multi-frequency EM measurements that were developed for one specific type of relaxation model under investigation, there is no unified and robust inversion scheme that can be coupled to various type of relaxation models to process multifrequency measurement of various EM properties.

Borehole-based subsurface electromagnetic (EM) measurements, namely galvanic resistivity (laterolog), induction, propagation, and dielectric dispersion logs, are

commonly used for water saturation estimation in hydrocarbon-bearing formations. Organic-rich shale formations generally exhibit high clay content and significant variations in lithology, rock texture, and total organic carbon accompanied by high connate water salinity and presence of disseminated pyrite grains. These petrophysical attributes affect water saturation estimates in shales. EM logs exhibit frequency dependence due to the interfacial polarization (IP) effects arising from clay grain surfaces, conductive minerals, and charge blockage in pore throats. IP effects in shale formations adversely affect the log-derived water saturation estimates, especially in the presence of low porosity, high salinity, and high clay concentration. Conventional EM log interpretation methods estimate water saturation in shale formations by separately interpreting the galvanic, induction, propagation, and dielectric dispersion logs using various empirical models or mixing laws. This approach leads to significant variations and uncertainties in petrophysical estimations.

Bakken Petroleum System (BPS) is composed of both conventional and unconventional units exhibiting significant variations in lithology, rock texture, clay content, total organic carbon (TOC), accompanied by high connate water salinity, presence of disseminated pyrite grains, and low values of porosity. These petrophysical attributes of BPS lead to inconsistency water saturation estimation obtained from different logging measurements. Dielectric dispersion log was applied in a science well in BPS to more accurately estimate water saturation while there is limited information about how service company process the dielectric dispersion log.

## **1.2 Objective of this study**

- (1) Develop a unified inversion scheme that can be coupled to various type of relaxation models to independently process multi-frequency measurement of varied EM properties for purposes of improved EM-based geomaterial characterization.
- (2) Develop an inversion-based joint petrophysical interpretation of multifrequency effective electrical conductivity and dielectric permittivity logs derived from various combinations of laterolog, induction, propagation, and dielectric dispersion logs acquired in clay- and pyrite-rich shale formations.
- (3) Develop an inversion-based interpretation method to process dispersive electrical conductivity and dielectric permittivity logs acquired at dielectric-dispersion tool operation frequency.

## **1.3 Organization of thesis**

The following is an outline and brief description of the remainder this thesis:

Chapter 2 contains a literature review about the various dispersive electromagnetic properties laboratory measurements and broadband EM dispersion logs and interpretation models;

Chapter 3 introduces a unified inversion scheme that can be coupled to various type of relaxation models to independently process multi-frequency measurement of varied EM properties;

Chapter 4 elucidates our proposed inversion-based joint petrophysical interpretation of multifrequency effective electrical conductivity and dielectric permittivity logs derived

from various combinations of the four aforementioned downhole EM logs acquired in clay- and pyrite-rich shale formations;

Chapter 5 elucidates the proposed open source inversion-based interpretation method to process dielectric dispersion log acquired in Bakken Petroleum System.

Chapter 6 includes conclusions that can be drawn from the results presented in previous chapter.

## Chapter 2: Literature Review

### 2.1 Dispersive EM properties, laboratory measurements and relaxation models

Dispersive electromagnetic (EM) properties of a geomaterial refer to electrical conductivity, dielectric permittivity, and magnetic permeability as a function of operating frequency (Marshall and Madden, 1959; Wong, 1979). Additionally, various polarization phenomena, such as membrane polarization (de Lima and Sharma, 1992), concentration polarization (Sumi, 1965), induced polarization (Seigel, 1959), Maxwell-Wagner polarization (Schurr, 1964), and dipolar/orientation polarization (Fuller and Ward, 1970), occur in geomaterials in the presence of external electromagnetic field that give rise to the frequency dispersions (frequency dependence) of electrical conductivity and dielectric permittivity measurements (Misra et al., 2016b). There are several experimental (e.g., Misra et al., 2015) and field-scale studies (e.g., Misra et al., 2016c) on frequency dispersions of conductivity and permittivity arising from polarization phenomena. Recently, there has been a push towards understanding the polarization phenomena and their effects on EM properties of geomaterials in the presence of conductive minerals (Revil et al., 2015; Misra et al., 2016a) and that in volcanic rocks (Revil et al., 2017).

A relaxation model generally processes the multi-frequency conductivity, permittivity, or magnetic permeability measurements for purposes of EM-based geomaterial characterization, which involves estimation of empirical/physical parameters that are unique to the geomaterial with respect to the measured physical process. A relaxation model describes a measurable spectral property of a perturbed physical system returning to equilibrium using descriptive empirical parameters specific to the system and the property being measured. Relaxation models have been used for characterization of

soil (Lesmes and Friedman, 2005), mineral (Wong, 1979), hydrocarbon reservoirs (Revil et al., 2013), groundwater (Revil, 2012), subsurface contaminant, and geological formations. The dispersive EM measurement can be processed to estimate hydraulic conductivity (Binley et al., 2005), pore or grain size distribution (Revil and Florsch, 2010), and mineral content (Gurin et al., 2015; Misra and Han, 2016a). In order to process a dispersive EM measurement, a deterministic or stochastic inversion algorithm can be applied to iteratively minimize the difference between the measurements and the numerical predictions of a relaxation model for a set of relaxation model parameters.

Kemna et al. (1999) developed an inversion algorithm coupled with a finite-element EM forward model to jointly invert for resistivity magnitude and phase, which were further analyzed based on an inversion algorithm coupled with Cole-Cole relaxation model to obtain additional petrophysical information. The inversion process was used by Kemna et al. (1999) to delineate subsurface hydrocarbon contamination at a former jet fuel depot and to image sulfide deposit in a metamorphic formation. Slater et al. (2006) conducted induced polarization measurements on saturated kaolinite-, iron-, and magnetite-sand mixtures for various weight fraction of the disseminated mineral constituents at various frequencies. The SIP measurements on the magnetite and iron mixtures were fitted using the Cole-Cole model predictions. The global polarization magnitude obtained from the Cole-Cole modeling of the IP measurements exhibited a single, near-linear dependence on the ratio of surface area to pore volume for the iron and magnetite mixtures. This relationship between SIP measurements and the ratio of surface area to pore volume was first identified by Börner and Schön (1991).

## **2.2 Broadband EM dispersion log**

Borehole-based EM measurements are regularly used to evaluate water saturation in geological formations for applications in hydrocarbon reservoir characterization, soil science, and hydrology. In the upstream oil and gas industry, water saturation estimates along the depth of a geological formation enables the estimation of original oil in place (Misra and Han, 2016a). Borehole-based EM measurements include four logs, namely galvanic resistivity (laterolog), induction, LWD propagation, and dielectric dispersion logs, operating at four distinct frequency ranges from 10 Hz to 1 GHz. Deployment of all the four EM tools in a single well followed by a joint interpretation of the multi-frequency conductivity and permittivity acquired over a broadband frequency range for water saturation estimation is not a common practice.

It is not a common practice to measure permittivity along with resistivity when using the laterolog and induction logging tools. Moreover, it is not usual to run all the four types of EM tools in a single well followed by a joint interpretation of the broadband EM measurements; therefore, water saturation is generally estimated using only one of the four EM logging tool measurements. Conventional petrophysical interpretation of a single-frequency EM log tends to generate inconsistent water saturation estimation, primarily due to the IP effects on complex conductivity. Wang and Poppitt (2013) reported first-of-its-kind continuous broadband multifrequency conductivity and permittivity logs derived from EM induction, EM propagation and dielectric dispersion logs acquired in an organic-shale formation. Wang and Poppitt (2013) recommended a joint interpretation of broadband EM logs for improved estimations of water saturation and clay properties.

### **2.3 EM dispersion log interpretation models**

For purposes of water saturation estimation, several EM-measurement interpretation methods use frequency-independent empirical models to separately process the effective electrical conductivity and dielectric permittivity. There also exist several frequency-dependent geoelectromagnetic interpretation models, such as Stroud-Milton-De (SMD) model (Stroud et al., 1986) and bimodal model (Sen et al., 1981), suited for dielectric dispersion logging measurements. Complex-refractive index (CRI) model and its modification Lichtenecker-Rother model (Sabouroux and Ba, 2011) are widely used to interpret the effective conductivity and permittivity of homogeneous and layering materials at frequencies close to 1 GHz to obtain water saturation estimates. SMD model accounts for the Maxwell-Wagner IP effect arising in brine-saturated sandstones and aids in the estimations of water saturation, formation water salinity, and tortuosity of the water phase (Donadille et al., 2016). SMD model breaks down for clay- and conductive-mineral-rich formations. Dielectric relaxation models, such as Cole-Cole model, are frequency-dependent phenomenological model that can predict the conductivity and permittivity spectra arising due to the IP effects. However, being phenomenological model, the parameters of dielectric relaxation models do not represent petrophysical properties. All the above-mentioned models neglect the physical mechanism of IP effects of clays and conductive minerals; thereby generating inaccurate estimation of water saturation and total organic carbon (TOC) in clay- and conductive-mineral-rich mudrock formations (Misra and Han, 2016a; Misra and Han, 2016b). The IP effects arising from clay and conductive mineral grains influence charge carrier migration, accumulation/depletion and diffusion processes in brine saturated porous geological



formations; thereby altering the electrical and dielectric properties of the porous media (Misra et al., 2017).

Misra et al. (2016a) derived a mechanistic electrochemical model, referred as the PS model, for geological mixtures containing clay and conductive minerals to evaluate the dependence of effective complex conductivity of the homogeneous conductive-mineral-bearing geomaterials on the conductivity of host and inclusion material, size and shape of inclusions, and the measurement frequency. PS model is calibrated to honor Archie's equation at low frequency ( $\sim 1$  Hz) and CRI model at high frequency ( $\sim 1$  GHz).

In this thesis, the joint interpretation of the multifrequency conductivity and permittivity logs derived from EM induction, EM propagation and dielectric dispersion logs acquired in a North European organic-shale formation is accomplished using an inversion algorithm coupled with the PS model. The inversion-based interpretation method can estimate water saturation ( $s_w$ ), brine conductivity ( $C_w$ ), surface conductance of clays ( $\lambda_c$ ), average grain radius of clays ( $r_c$ ), and average grain radius of pyrite inclusions ( $r_i$ ) which are parameters in PS model, in clay- and pyrite-rich formations. A similar mechanistic joint interpretation of the multi-tool, multifrequency EM logs generates consistent water saturation estimates (Misra and Han, 2016b). Consistent water saturation estimates improve formation evaluation, reservoir characterization, and reservoir development strategy.

## **Chapter 3: Unified Inversion Scheme of Various Relaxation Models**

### **3.1 Introduction of polarization and relaxation models**

Conductivity is a measure of a material's ability to conduct an electric current and dielectric permittivity is the measure of resistance that is encountered when forming an electric field in a material and quantifies the sensitivity of a medium to an electric field excitation (Hizem et al., 2008). Conductivity and permittivity of geomaterials depend on water saturation, connate water salinity, porosity, tortuosity, wettability, clay content and distribution, conductive mineral content and distribution, grain sizes, grain texture, and pore size distribution. There are three main physical phenomena contribute to the dielectric permittivity: the electronic cloud of atoms displacement, electric dipoles coherent orientation, and IP effects. All these effects can be integrated into a macroscopic polarization density which expresses the density of permanent or induced electric dipole moments in dielectric materials (Hizem et al., 2008). The dielectric permittivity is a function of applied electric field frequency because there is a lag between changes in polarization and changes in electric field, which is referred as dielectric dispersion. Similar to this, conductivity dispersion can exist due to the lag between application of electric field and the transport of charge carriers, which is assumed to be negligible in our studies.

Relaxation usually means the return of a perturbed system into equilibrium and each relaxation process can be characterized by one or combination of relaxation times. Relaxation models are phenomenological or mechanistic models used to describe the relaxation processes.

Dielectric relaxation models, such as Cole-Cole model, are frequency-dependent phenomenological model that can predict the conductivity and permittivity spectra arising due to the IP effects. However, being phenomenological model, the parameters of dielectric relaxation models do not directly represent petrophysical properties. There are also some physics based (mechanistic) mixing-models such as CRI and effective medium models, wherein the parameters of mechanistic models represent petrophysical properties that govern relaxation process and dispersion phenomena.

### 3.2 Relaxation models of characterizing polarization mechanisms

Cole-Cole model is the most frequently used relaxation model that was formulated to quantify the multi-frequency complex permittivity response of polar liquids and dielectrics. Cole-Cole model (Cole and Cole, 1941) is expressed as

$$\varepsilon^* = \varepsilon_{r\infty} + \frac{\varepsilon_{r0} - \varepsilon_{r\infty}}{1 + (i\omega\tau)^{1-\alpha}} \dots\dots\dots(3.1)$$

where  $\varepsilon_{r0}$  and  $\varepsilon_{r\infty}$  are the low-frequency and high-frequency permittivity values, respectively,  $\tau$  is the central relaxation time,  $\omega = 2\pi f$  is the angular frequency of EM measurement,  $f$  is the frequency of EM measurement, and exponent  $\alpha$  controls the width of the loss peak, such that  $0 < \alpha \leq 1$ . For porous material,  $\tau$  is typically between  $10^{-3}$  to  $10^3$  s (Kemna,2000). Cole-Cole model constitute special case of the Havriliak-Negami model that accounts for the broadness and asymmetry of dielectric dispersion curves. The Havriliak-Negami model (Havriliak and Negami, 1966) can be expressed as

$$\varepsilon^* = \varepsilon_{r\infty} + \frac{\varepsilon_{r0} - \varepsilon_{r\infty}}{[1 + (i\omega\tau)^{1-\alpha}]^\beta} \dots\dots\dots(3.2)$$

where  $\alpha$  and  $\beta$  are shape characteristics of the dielectric dispersion curve, such that  $0 < \alpha, \beta \leq 1$ .

Pelton et al. (1978) modified the Cole-Cole model to obtain an impedance model to analyze complex impedance measurements over  $10^{-2}$  Hz to  $10^5$  Hz made on 26 mineral deposits. The Pelton model can also be formulated in terms of resistivity as

$$\rho^* = \rho_0 \left[ 1 - m \left( 1 - \frac{1}{1+(i\omega\tau)^c} \right) \right] \dots\dots\dots(3.3)$$

where  $\rho^*$  is the measured complex resistivity,  $\rho_0$  is the low-frequency resistivity and  $m$  is the chargeability, and  $c = 1 - \alpha$  is the Cole-Cole model exponent. The value of the Cole-Cole model exponent  $c$  is typically in the range 0.1 to 0.6 for mineral-bearing rocks (Pelton et al., 1978). The low-frequency resistivity values of sedimentary rocks are typically between 10 to 10000  $\Omega\text{m}$  with most values less than 1000  $\Omega\text{m}$  (Loke, 2001).

A multiple Cole-Cole model for complex resistivity is expressed as

$$\rho^* = \rho_0 \left[ 1 - \sum_{l=1}^L m_l \left( 1 - \frac{1}{1+(i\omega\tau_l)^{c_l}} \right) \right] \dots\dots\dots(3.4)$$

where  $L$  is the number of Cole-Cole models that are required to compositely match with complex resistivity measurements. Dual Cole-Cole model is often encountered in practice either to describe an IP response with two relaxation domains or to describe a single relaxation IP response contaminated by inductive and/or capacitive coupling associated with the measurement layout (Pelton et al., 1978; Kemna et al., 1999). The symbols  $m_l$ ,  $\tau_l$  and  $c_l$  represent chargeability, relaxation time and exponent value for the  $l$ -th dispersion term in the multiple Cole-Cole model, respectively.

### 3.3 Literature review of inversion using relaxation models

For purposes of EM-based geomaterial characterization, a multi-frequency EM measurement on a geomaterial is generally inverted using a specific relaxation model to estimate certain relaxation model parameters that generate best match between the

relaxation model predictions and the measured data (e.g., Revil et al., 2013). In doing so, the estimated parameters of the relaxation model serve as characteristics/identifiers of the geomaterial. Relaxation-model-based inversion methods commonly implement the Gauss-Newton algorithm (GNA) or Levenberg-Marquardt algorithm (LMA) (e.g., Kemna et al., 1999).

Kemna (2000) proposed a single-frequency complex-resistivity inversion algorithm based on Tikhonov approach, which involves a univariate line search to find an optimum value of the regularization parameter for the stabilization functional. The minimization of data misfit is performed iteratively by a regularized Gauss-Newton approach. Cole-Cole model was then fitted to the multi-frequency inversion-derived complex resistivity values of each block in the mineral-bearing formation by means of a nonlinear least-squares inversion procedure, using simple Marquardt-regularization.

Xiang et al. (2001) inverted the complex impedance using Cole-Cole model. The proposed inversion algorithm consists of two parts: (a) multi-fold least-squares estimation that uses an assumed parameter for the frequency dependence of the Cole-Cole model,  $c$ , to estimate other Cole-Cole model parameters, namely the DC resistivity,  $\rho_0(c)$ , polarizability or chargeability,  $m(c)$ , and relaxation time,  $\tau(c)$  from the SIP data, and (b) search the optimal value of  $c$  using the golden section minimization algorithm. Cao et al. (2005) inverted complex resistivity data using an improved genetic algorithm to overcome the instability and non-convergence issues associated with the estimation of Cole-Cole model parameters based on linear inversion theory. The proposed method does not need an initial model and gives global search solution.

As mentioned above, several published methods for deterministic inversion of multi-frequency EM measurements were found to be highly sensitive to the initial guesses of the unknown relaxation-model parameters (Chen et al., 2008), such that unique estimates of the relaxation-model parameters are generated for initial guesses lying in close vicinity to the optimal solution (Roy, 1999). Notably, we found several publications on the deterministic inversion of multi-frequency EM measurements did not report the model sensitivity to initial guesses of the unknown relaxation-model parameters (e.g., Tarasov and Titov, 2013). Several published inversion methods for multi-frequency EM measurements that implement regularization parameters or adaptive parameters in the mathematical formulation of the inversion scheme do not mention the chosen values of such parameters, for instance, the initial values and rate of change of damping parameter  $\lambda$  and factor  $\nu$  in LMA (e.g., Lazović et al., 2014).

### **3.4 Improved bounded Levenberg inversion algorithm**

#### **3.4.1 Introduction of the unified inversion scheme**

In order to address all the above-mentioned shortcomings, we develop a unified inversion scheme that can be coupled to various type of relaxation models to process multifrequency measurement of various EM properties for purposes of consistent EM-based geomaterial characterization. We implement a bounded Levenberg nonlinear inversion algorithm based on a fixed damping parameter and its iterative adjustment factor, irrespective of the type of measured property and the type of relaxation model, with jump-back-in and jump-out sequences. These features ensure that the inversion

scheme is universal and converges for initial guesses with uncertainty within 3-orders of magnitude freeing the inversion scheme from user inputs, biases, and errors.

### 3.4.2 Nonlinear inversion as minimization

The non-linear inverse problem discussed in this section involves estimation of relaxation model parameters that generate least misfit between the measured and modeled multi-frequency geoelectromagnetic measurements. The measurements used in this section are real and imaginary part of complex permittivity, or complex resistivity of a geomaterial measured at several frequencies. A bounded Levenberg algorithm (LA) is implemented to find the solution of this nonlinear inverse problem by simultaneously matching the real and imaginary part of the measured data with the relaxation model predictions for all the measurement frequencies. Fig. 3.1 illustrates the flowchart of the inversion scheme.

In the proposed inversion scheme, a relaxation model  $R^*(\mathbf{m}, \omega)$  is first chosen to model the frequency-dispersive complex permittivity or complex resistivity of the geomaterial at a specific angular frequency  $\omega$  of measurement. The relaxation model is described using a specific  $l$ -sized relaxation-model parameter vector  $\mathbf{m}$ . Then, an  $n$ -sized modeled data vector  $\mathbf{D}^{\text{mod}}(\mathbf{m})^*$  is built as a collection of relaxation model predictions for the  $n$  frequencies of measurements and a specific relaxation-model parameter vector  $\mathbf{m}$ , such that  $\mathbf{D}^{\text{mod}}(\mathbf{m})^* = [R^*(\mathbf{m}, \omega_1); R^*(\mathbf{m}, \omega_2); \dots \dots; R^*(\mathbf{m}, \omega_n)]$ . Following that, the measured data  $\mathbf{D}^{\text{meas}*}$  is matched with modeled data vector  $\mathbf{D}^{\text{mod}}(\mathbf{m})^*$  to find the vector  $\mathbf{m}$  comprising the estimates of  $l$  relaxation-model parameters that quantitatively characterize the geomaterial under investigation. To that end, the inversion algorithm iteratively computes the  $l$ -sized vector  $\mathbf{m}^{\text{est}}$  comprising the estimates of  $l$  relaxation-model

parameters, such that the  $n$ -sized modeled data vector  $\mathbf{D}^{\text{mod}}(\mathbf{m}^{\text{est}})^*$  best matches the measured data vector  $\mathbf{D}^{\text{meas}*}$ . In other words, the inversion algorithm iteratively adjusts the vector of relaxation-model parameters  $\mathbf{m}$  to compute the inverted relaxation-model parameter vector  $\mathbf{m}^{\text{est}}$  that minimizes the error between the measured data vector  $\mathbf{D}^{\text{meas}*}$  and the modeled data vector  $\mathbf{D}^{\text{mod}}(\mathbf{m}^{\text{est}})^*$ . This requires minimizing quadratic cost function  $C(\mathbf{m})$  at each iteration defined as

$$C(\mathbf{m}) = \|\text{real}[\mathbf{D}^{\text{mod}}(\mathbf{m}^{\text{est}})^* - \mathbf{D}^{\text{meas}*}]\|_2^2 + w \cdot \|\text{imag}[\mathbf{D}^{\text{mod}}(\mathbf{m}^{\text{est}})^* - \mathbf{D}^{\text{meas}*}]\|_2^2 \dots \dots \dots (3.5)$$

where  $\|\cdot\|_2^2$  is the square of the  $L2$  norm (or Euclidean length) and  $w$  is the  $n$ -sized weight factor which is expressed as

$$w = 10^a \dots \dots \dots (3.6)$$

where  $a$  is a positive integer computed as the ratio of magnitude of the real part to that of the imaginary part of the measured EM property. The weight factor  $w$  in Eq. 3.5 is used to normalize the errors in real part and imaginary part to ensure that the inversion scheme honors both the errors.

In this unified inversion scheme, the  $n$ -sized vector  $\mathbf{D}^*$  is replaced with vectors  $\boldsymbol{\varepsilon}^*$  or  $\boldsymbol{\rho}^*$  when the measurement is complex permittivity or complex resistivity, respectively. For purposes of minimization, we define a  $n$ -sized cost function vector  $\mathbf{F}(\mathbf{m})$ . Individual components of the vector  $\mathbf{F}(\mathbf{m})$  are referred as  $f_i(\mathbf{m}^k)$ , where superscript  $k$  is used as the iteration count for the inversion scheme,  $\mathbf{m}^k$  is the  $l$ -sized relaxation-model parameter vector computed at the  $k$ -th iteration, and subscript  $i$  denotes one of the  $n$  frequencies of measurements.  $\mathbf{F}(\mathbf{m}^k)$  is then expressed as

$$\mathbf{F}(\mathbf{m}^k) = [f_1(\mathbf{m}^k), f_2(\mathbf{m}^k), \dots, f_n(\mathbf{m}^k)]^T \dots \dots \dots (3.7)$$



where  $f_i(\mathbf{m}^k)$  is expressed in the form of the cost function formulation of Eq. 3.7 as

$$f_i(\mathbf{m}^k) = [\text{real}(\mathbf{D}^{\text{mod}}(\mathbf{m}^k)^* - \mathbf{D}^{\text{meas}^*})]_i^2 + w \cdot [\text{imag}(\mathbf{D}^{\text{mod}}(\mathbf{m}^k)^* - \mathbf{D}^{\text{meas}^*})]_i^2 \dots \dots \dots (3.8)$$

Based on the Levenberg nonlinear inversion method (Aster et al., 2005), the inversion scheme can be expressed as

$$[(\mathbf{W}_d \mathbf{J}(\mathbf{m}^k))^T \cdot (\mathbf{W}_d \mathbf{J}(\mathbf{m}^k)) + \lambda \mathbf{I}] \cdot \Delta \mathbf{m}^k = -(\mathbf{W}_d \mathbf{J}(\mathbf{m}^k))^T \cdot (\mathbf{W}_d \mathbf{F}(\mathbf{m}^k)) \dots \dots \dots (3.9)$$

where  $\mathbf{J}(\mathbf{m}^k)$  is the  $n \times l$  Jacobian matrix of  $\mathbf{F}(\mathbf{m}^k)$ ,  $\mathbf{I}$  is  $l \times l$  identity matrix, superscript T is matrix transpose operator,  $\Delta \mathbf{m}^k$  is the  $l$ -sized correction vector that determines the direction toward the convergence of relaxation-model parameter estimation.  $\mathbf{W}_d$  is the  $n \times n$  data weight matrix and is the inverse of the data covariance matrix (e.g., Torres-Verdín et al., 2000) and  $\lambda$  is the damping parameter. Using  $\Delta \mathbf{m}^k$  computed in Eq. 3.9, we can calculate the successive estimates for the relaxation-model parameters as

$$\mathbf{m}^{k+1} = \mathbf{m}^k + \Delta \mathbf{m}^k \dots \dots \dots (3.10)$$

such that all elements of the  $l$ -sized vector  $\mathbf{m}^{k+1}$  lie within the predefined lower and upper limits for each of the relaxation-model parameters.

The Jacobian matrix of  $\mathbf{F}(\mathbf{m}^k)$  is formulated as

$$\mathbf{J}(\mathbf{m}^k) = \begin{pmatrix} \frac{\partial f_1(\mathbf{m}^k)}{\partial m_1} & \dots & \frac{\partial f_1(\mathbf{m}^k)}{\partial m_l} \\ \vdots & \ddots & \vdots \\ \frac{\partial f_n(\mathbf{m}^k)}{\partial m_1} & \dots & \frac{\partial f_n(\mathbf{m}^k)}{\partial m_l} \end{pmatrix} \dots \dots \dots (3.11)$$

We implemented the first order central-difference formula to numerically approximate the derivative of  $f_i(\mathbf{m}^k)$  with respect to  $j$ -th unknown relaxation-model parameters formulated as

$$\frac{\partial f_i(\mathbf{m}^k)}{\partial m_j} \approx \frac{f_i(m_j^k + \Delta mc_j^k) - f_i(m_j^k - \Delta mc_j^k)}{2\Delta mc_j^k} \dots \dots \dots (3.12)$$

where  $\mathbf{m}^k = [m_1^k; m_2^k; \dots; m_l^k]$ ,  $\Delta mc_j^k = 0.001 m_j^k$ ,  $1 \leq j \leq l$ , and  $1 \leq i \leq n$ .

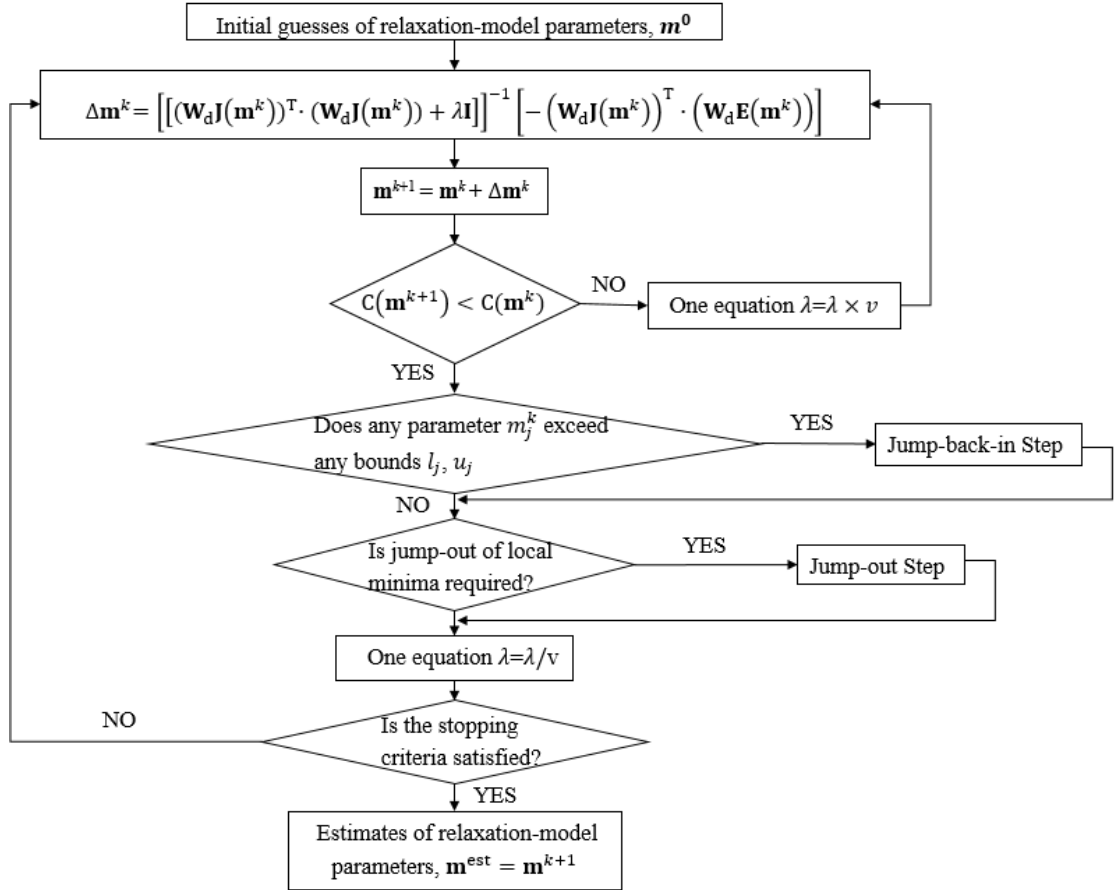


**Figure 3.1 Flowchart of the unified inversion scheme**

In this proposed scheme, we do not search for global minimum. Rather, we randomly initialize the inversion scheme to perform multiple inversions within pre-defined ranges for the unknown relaxation-model parameters. During the inversion, the estimates for the model parameters are selected as the solution of the inverse problem when: (a) the data misfit goes below a pre-defined threshold and (b) the frequency of occurrence of estimates are the highest among the multiple random initializations. As shown in Table 3.1 (synthetic case inversion), this selection criterion successfully

identifies the estimates that are closest to the true values, which were defined a priori to generate the synthetic measurements.

### **3.4.3 Damping parameter and iterative adjustment factor**

Roy (1999) showed that an adaptive damping parameter made the inversion scheme more efficient and robust. The positive damping parameter  $\lambda$  is adjusted by the iterative adjustment factor  $\nu$  at each iteration to ensure fast convergence and accuracy of the estimated values of relaxation-model parameters. The damping parameter prevents singularities or near-singularities of the matrix  $(\mathbf{W}_d \mathbf{J}(\mathbf{m}^k))^T \cdot (\mathbf{W}_d \mathbf{J}(\mathbf{m}^k))$ . The inversion formulation proposed in Eq. 3.9 simply moves down-gradient along the residual surface area for very large values of  $\lambda$ . Conversely, for very small values of  $\lambda$ , Eq. 3.9 reverts to GNA, which gives potentially fast but uncertain convergence (Aster et al., 2005). The general strategy is to use small values of  $\lambda$  but to switch to larger values of  $\lambda$  when the GNA-dominated inversion fails to make progress. That is to say, when the LMA leads to a reduction in  $C(\mathbf{m})$ ,  $\lambda$  is reduced by dividing by the factor  $\nu$  after each iteration. However, when the LMA doesn't lead to a reduction in  $C(\mathbf{m})$ ,  $\lambda$  is increased by multiplying by the factor  $\nu$  after each iteration. One challenge associated with LMA is determining the value of  $\lambda$  and  $\nu$ . The inversion results for both synthetic and measured data cases exhibit good convergence and accuracy for only specific combinations of initial values of  $\lambda$  and  $\nu$ . We chose the initial value of  $\lambda$  and  $\nu$  to be equal to 10 as inversion generates low data misfit error.

### **3.4.4 Bounds of relaxation-model parameters and jump-back-in step**

Unlike incorporating the transformations functions of model parameters into cost function (e.g., Kim and Kim, 2011), we propose an alternative method to ensure the estimates are bounded during the inversion. For the estimation of each relaxation-model parameter, upper and lower bounds are set to ensure that the estimated values of the parameters are physically consistent, such that  $l_j \leq m_j^k \leq u_j$ , where  $l_j$  and  $u_j$  are the lower and upper bounds, respectively, of the  $j$ -th relaxation-model parameter to be estimated,  $m_j^k$ . The mid-point of the lower and upper bounds of the  $j$ -th relaxation-model parameter is  $M_j$  and  $m_j^{k-1}$  is the estimated value of the  $j$ -th parameter at the  $k-1$ -th iteration. At  $k$ -th iteration, when  $m_j^k$  exceeds the set bounds, a jump-back-in step is initiated using  $m_j^{k-1}$  and the upper and lower boundaries for the  $j$ -th model parameter.

Fig. 3.2 illustrates the algorithm of the jump back-in step aimed at automating the step based on the distance between the estimated value of the  $j$ -th parameter  $m_j^{k-1}$  at the  $k-1$ -th iteration and the boundary. The  $j$ -th relaxation-model parameter after the jump back-in step is  $m_j^{k'}$ .

In Fig. 3.2, there are four different scenarios when  $m_j^k$  exceeds the set bounds, algebraic manipulation will be applied to  $m_j^{k-1}$  that was within the bounds. After the algebraic manipulation,  $m_j^{k'}$  will be obtained as the value of the  $j$ -th relaxation-model parameter at the  $k$ -th iteration that will be within the bounds. For the algebraic manipulation applied to  $m_j^{k-1}$ , we use an exponential function of the distance between  $m_j^{k-1}$  and one of the bounds, such that when the distance between the  $m_j^{k-1}$  and the bound, which  $m_j^k$  exceeds, is small the  $m_j^{k'}$  after jump back-in step will also close to that

bound. There is a factor ‘0.25’ before the exponential function to guarantee that after the algebraic manipulation the estimates do not exceed the bounds.

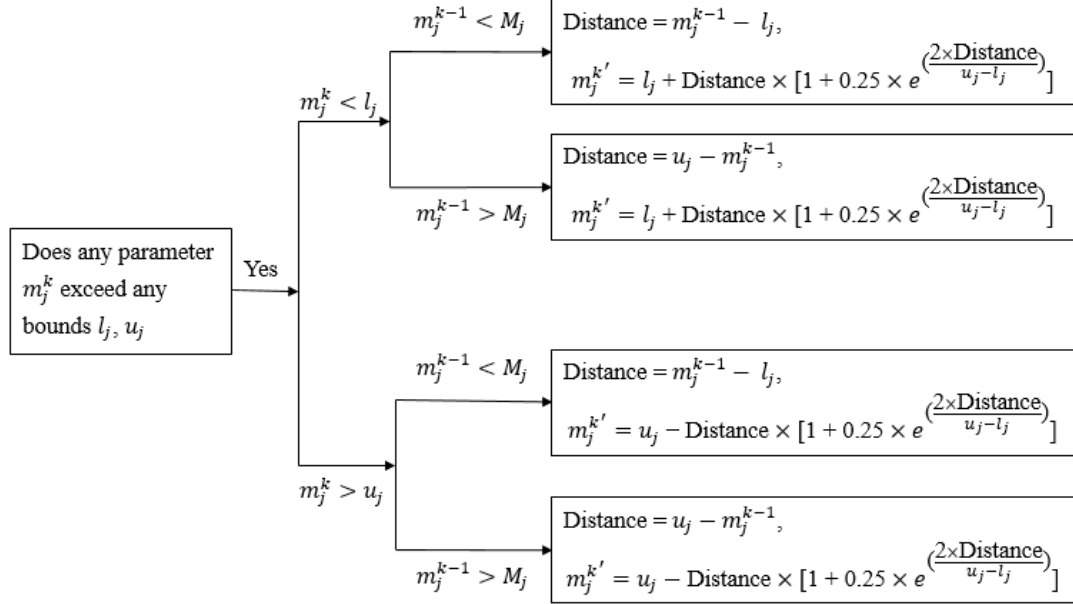


**Figure 3.2 Flowchart of the jump back-in step**

### 3.4.5 Jump-out of local minima step

We implement a scheme to jump out of local minima when the rate of change in the difference between modeled data and measured data with iteration is below a certain threshold in a window of 50 iterations. When a jump-out of local minima step is invoked, all the relaxation-model parameters are altered based on an automated algorithm. Fig. 3.3 illustrates the criteria of initiating jump out step. When the data misfit error is larger than a pre-defined threshold and the rate of change in error stabilizes for 50 iterations, the inversion-derived estimates for the parameters have reached a local minimum. This requires initiation of the jump out step to get out of local minimum and reach the global minimum. To be specific, the jump out is initiated when the decline rate  $r_1$  for the misfit errors between adjacent iterations is lower than 0.01 and the decline rate  $r_2$  between  $k$ -th

and  $k-50$ -th iterations is lower than 0.1. For the  $j$ -th relaxation-model parameter, the midpoint of  $l_j$  and  $M_j$ , which is the midpoint of the lower and upper bounds, is  $P_j$  and the midpoint of  $M_j$  and  $u_j$  is  $Q_j$ . The jump out step includes reflection of inversion-derived estimates along a plane, which is an algebraic manipulation of the parameter about a reflection point. The jump out algorithm can accommodate moving out of three local minima during the inversion. This requires three reflections (algebraic manipulation) along  $P_j$ ,  $M_j$ , and  $Q_j$  planes, respectively. Fig. 3.3 shows the process for the first reflection along the  $P_j$  plane. The  $j$ -th relaxation-model parameter after the jump out step is  $m_j^{k'}$ . The second reflection is similar to the first one but along the  $M_j$  plane. The third reflection uses either the lower boundary or upper boundary, i.e.  $m_j^k$  and  $m_j^{k'}$  are equidistant from  $l_j$  and  $u_j$ , respectively, or vice versa. The three consecutive reflections are initiated only when the error remains higher than the pre-defined threshold.

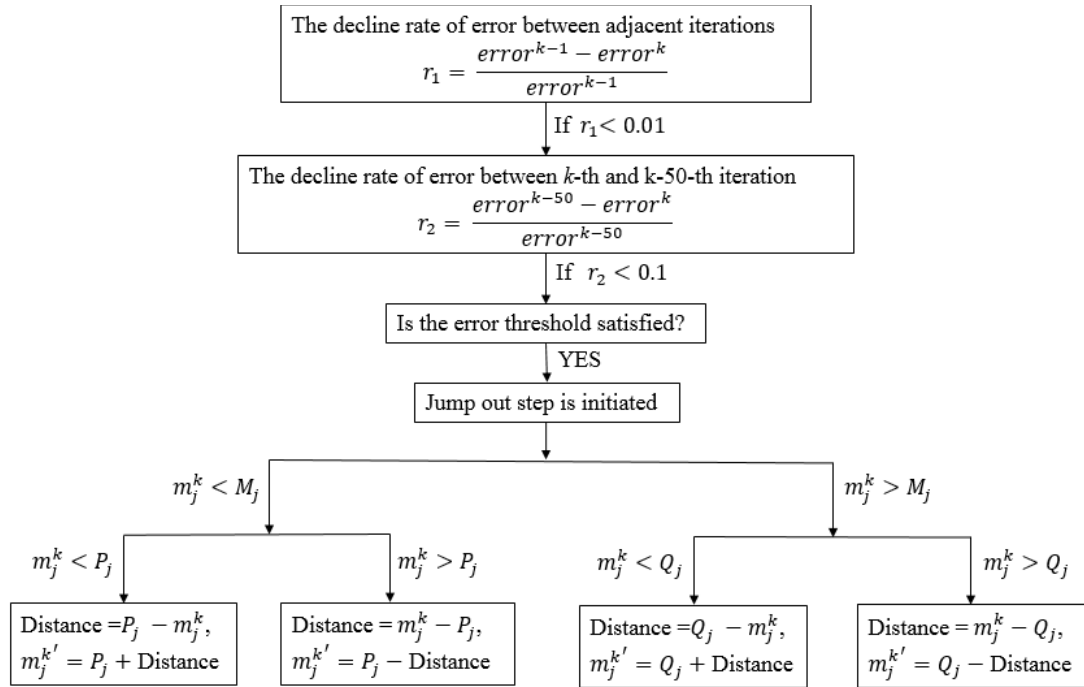


**Figure 3.3 Flowchart of the jump out step for the first reflection**

### 3.4.6 Error in model predictions based on the estimated parameters

Data misfit error is described in terms of the difference between modeled data based on the estimated relaxation-model parameters and the measured EM data. This data misfit error is expressed as

*Error* =

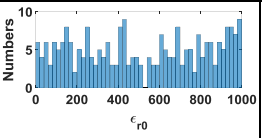
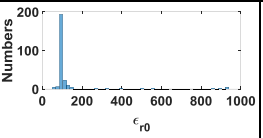
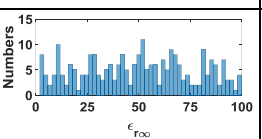
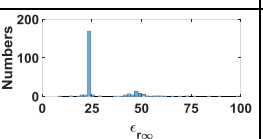
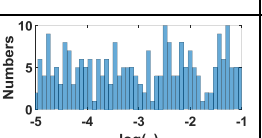
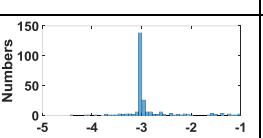
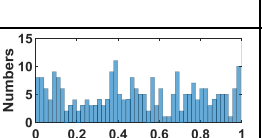
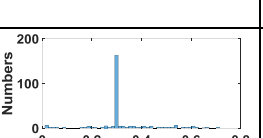
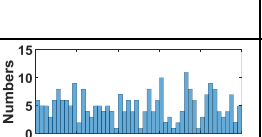
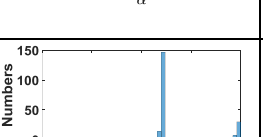
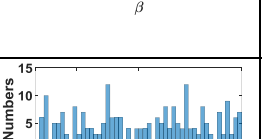
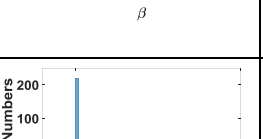
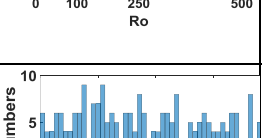
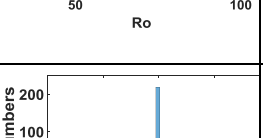
$$\sqrt{\frac{1}{n} \cdot \sum_{i=1}^n \{[\text{real}(\mathbf{D}^{\text{mod}}(\mathbf{m}^k) - \mathbf{D}^{\text{meas}})]_i^2 + [\text{imag}(\mathbf{D}^{\text{mod}}(\mathbf{m}^k) - \mathbf{D}^{\text{meas}})]_i^2\}} \dots \dots \dots (3.13)$$

### 3.5 Synthetic cases validation

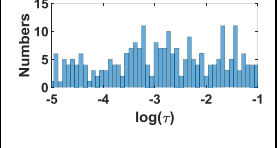
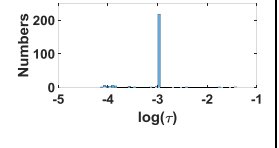
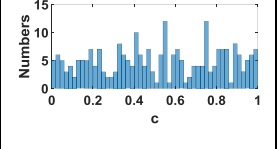
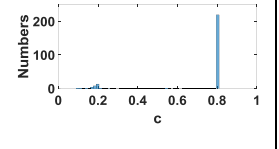
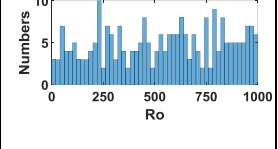
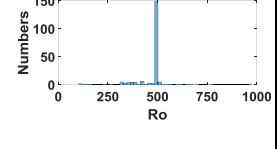
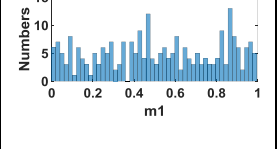
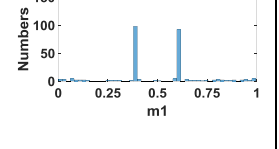
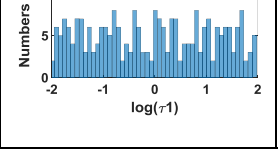
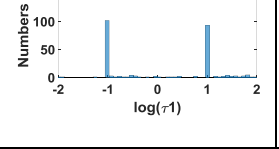
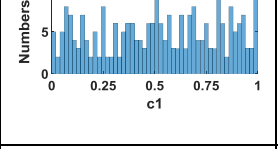
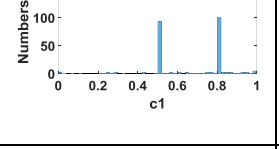
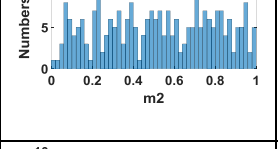
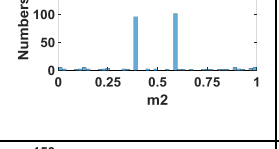
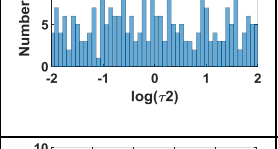
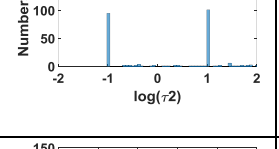
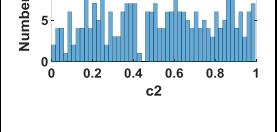
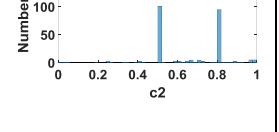
In order to show the robustness of the newly developed inversion algorithm, we tested its performance by means of numerical simulation or synthetic case inversion. Three sets of synthetic data were generated using Havrilak-Negami model (complex permittivity data), Cole-Cole model, and dual Cole-Cole model (complex resistivity data). Synthetic data is generated based on the parameter values listed in Column 3 of Table 3.1 and contain 2% Gaussian noise. Following that, the synthetic data were inverted using the proposed inversion scheme coupled with a corresponding relaxation model. Column 4 of Table 3.1 lists the histogram for the 250 randomly chosen initial guesses for each of the model parameters. Column 5 lists the histogram of inversion-derived estimates that exhibit great convergence to the true parameter values. The performance of the inversion algorithm with the jump back-in and jump out step is not sensitive to the initial guesses. Table 3.2 focusses on the robustness of the inversion algorithm in the presence of various levels of Gaussian noise ranging from 0% to 5%. The inversion was performed on synthetic data generated using the dual Cole-Cole model of resistivity with

seven unknown model parameters. In the presence of 5% noise, the estimation of model parameter  $\tau_2$  exhibited highest inaccuracy of 10%, whereas the estimates of rest of the parameters exhibited less than 1% inaccuracy.

**Table 3.1 The inversion-derived estimates of Havriliak-Negami model, Cole-Cole model and dual Cole-Cole model parameters for inversion of synthetic dispersive data.**

Model	Parameters	Parameters true values	Parameters initial guess	Estimated values	Inverted values
Havriliak-Negami	$\epsilon_{r0}$	100			99.85
	$\epsilon_{r\infty}$	25			24.34
	$\tau$ (s)	$1 \times 10^{-3}$			$1 \times 10^{-3}$
	$\alpha$	0.3			0.302
	$\beta$	0.7			0.682
Cole-Cole model	$R_o$ ( $\Omega$ )	50			49.9
	$m$	0.5			0.498



Cole-Cole model	$\tau$ (s)	$1 \times 10^{-3}$			$1 \times 10^{-3}$
	$c$	0.8			0.805
Dual Cole-Cole model	$R_o(\Omega)$	500			499.2
	$m_1$	0.4			0.3974
	$\tau_1$ (s)	$1 \times 10^{-1}$			0.0989
	$c_1$	0.5			0.5097
	$m_2$	0.6			0.5976
	$\tau_2$ (s)	$1 \times 10^1$			10.0885
	$c_2$	0.8			0.814

**Table 3.2 Inversion-derived estimates of dual Cole-Cole model parameter required to fit synthetic resistivity data containing various levels of Gaussian noise.**

Noise level	Estimated $R_o(\Omega)$	Estimated $m_1$	Estimated $\tau_1$ (s)	Estimated $c_1$	Estimated $m_2$	Estimated $\tau_2$ (s)	Estimated $c_2$
Without noise	500	0.4	0.1	0.5	0.6	10	0.8
1% Gaussian noise	499.6	0.407	0.1	0.51	0.592	10.57	0.8
2% Gaussian noise	499.2	0.397	0.099	0.51	0.598	10.1	0.814
5% Gaussian noise	498	0.375	0.104	0.506	0.615	9	0.83

### 3.6 Inversion of laboratory EM measurement

Two laboratory measurement data inversion cases are illustrated to show the efficiency of the proposed unified inversion scheme. The first case is multifrequency complex permittivity inversion and the second case is complex resistivity inversion.

#### *Case 1: Five-Parameter Inversion of Havriliak-Negami Model Parameters*

We use the multi-frequency permittivity measurements on poly (methyl acrylate) at 30 °C reported by Havriliak and Negami (1966). The complex permittivity was measured using the General Radio Bridge (Type 1610-B) and Cell (Type 1690-A). The complex permittivity measurements were acquired at seven frequencies: 31Hz, 100Hz,

310Hz, 1kHz, 3.1kHz, 10kHz, and 150kHz. They demonstrated that the  $\alpha$ -relaxation process for poly (methyl acrylate) can be modeled using the Havriliak-Negami model, as described in Eq. 3.2. They graphically analyzed the plot of real part vs. imaginary part of the complex permittivity measurements to determine the five parameters of Havriliak-Negami relaxation model that characterize the poly (methyl acrylate) sample under investigation.

Our estimates of  $\varepsilon_{r0}$ ,  $\varepsilon_{r\infty}$ ,  $\tau_0$ ,  $\alpha$ , and  $\beta$  using the proposed unified inversion scheme are all close to those reported by the authors ( $\varepsilon_{r0} = 6.48$ ,  $\varepsilon_{r\infty} = 3.705$ ,  $\alpha = 0.345$ ,  $\tau_0 = 2 \times 10^{-3}$  s, and  $\beta = 0.392$ ). The Havriliak-Negami relaxation model predictions of real relative permittivity ( $\varepsilon_r'$ ) and imaginary relative permittivity ( $\varepsilon_r''$ ) based on inversion-derived estimates of five parameters match the measured complex relative permittivity measurements with an absolute error less than 0.017 as shown in Fig. 3.5, which is smaller than the error based on the reported parameter values by Havriliak and Negami (1966). Fig. 3.4 shows successful convergence of the inversion-derived estimates for 5 randomly chosen initial guesses of model parameter  $\varepsilon_{r0}$ ,  $\varepsilon_{r\infty}$ ,  $\alpha$ ,  $\tau_0$ , and  $\beta$ .

Efficacy of the jump out step can be explained based on the convergence for one of the initial guesses indicated by the dash line. The error of that inversion run (dashed line) remains higher than the pre-defined threshold and gets stable for more than 50 iterations, which initiates the jump out sequence. The jump out step is initiated around 75-th iteration, and the inversion run then converges to the global minimum where all other inversion runs converge.

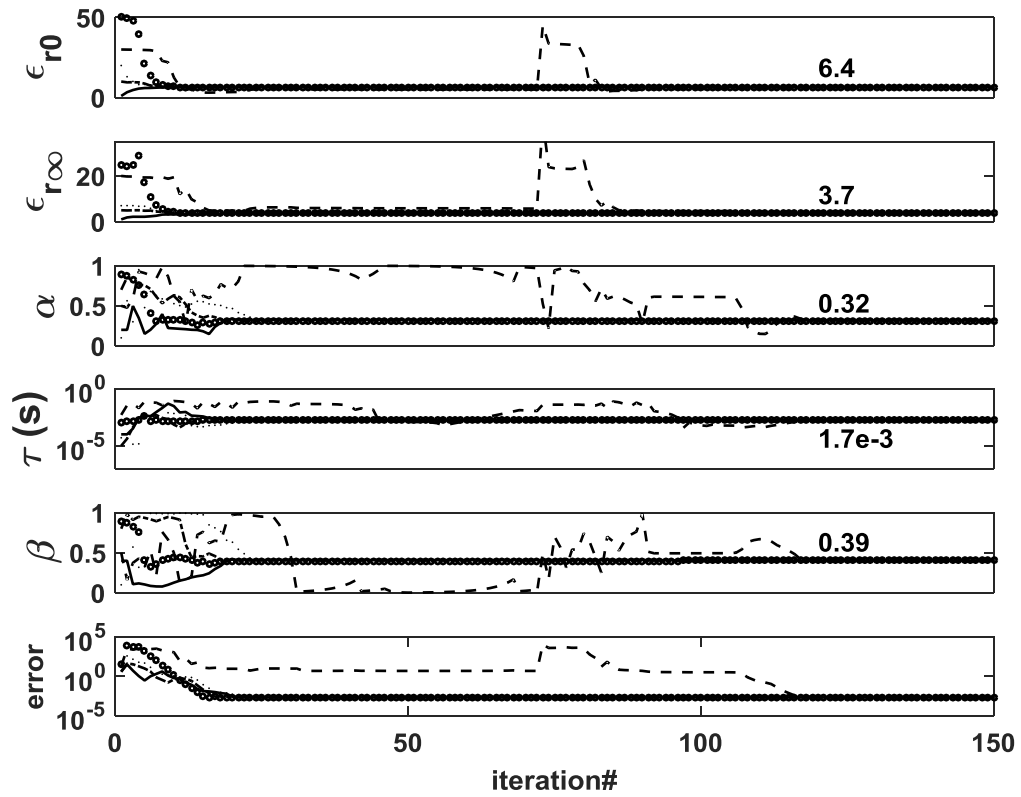


**Figure 3.4** Convergence of estimates of relaxation-model parameters and error as a function of iteration for inversion of multi-frequency measurement of complex permittivity.

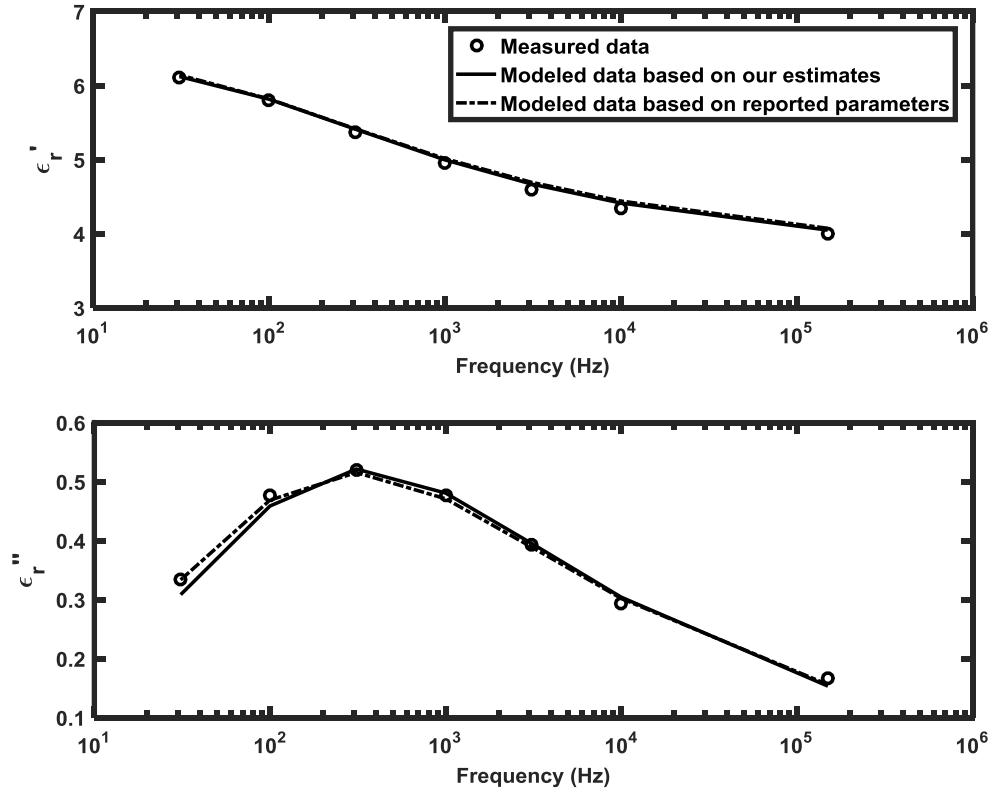


**Figure 3.5 Comparisons of real and imaginary permittivity measurements on poly (methyl acrylate) solution reported by Havriliak and Negami (1966) against the Havriliak-Negami relaxation model predictions based on the estimated parameters.**

*Case 2: Seven-Parameter Inversion of Dual Cole-Cole Model Parameters*

The proposed inversion scheme is applied to the multi-frequency resistivity measurements on unconsolidated silica-sand samples reported by Kemna et al. (2005). We use Eq. 3.4 for  $L=2$  to model the measured data. The samples have grain size of 125-250  $\mu\text{m}$  and were saturated with  $3 \times 10^{-4}$  molar KCl solution (Kemna et al. 2005). They measured complex resistivity at 71 frequencies from  $1 \times 10^{-3}$  Hz to  $1 \times 10^5$  Hz. The inversion-derived estimates successfully converged for broad range of initial guesses which are random chosen. Our estimates for the seven unknown relaxation-model parameters are:  $\rho_0 = 773 \Omega\text{m}$ ,  $m_1 = 0.0069$ ,  $\log(\tau_1) = -1.1$  ( $\tau_1$  in s),  $c_1 = 0.4$ ,  $m_2 = 0.45$ ,

$\log(\tau_2) = -7.1$  ( $\tau_2$  in s), and  $c_2 = 0.78$ , as shown in Fig. 3.6. The Cole-Cole relaxation model prediction based on our estimates of the seven parameters match the measured complex resistivity measurements with an absolute error of less than  $1 \Omega\text{m}$ , as shown in Fig. 3.7.

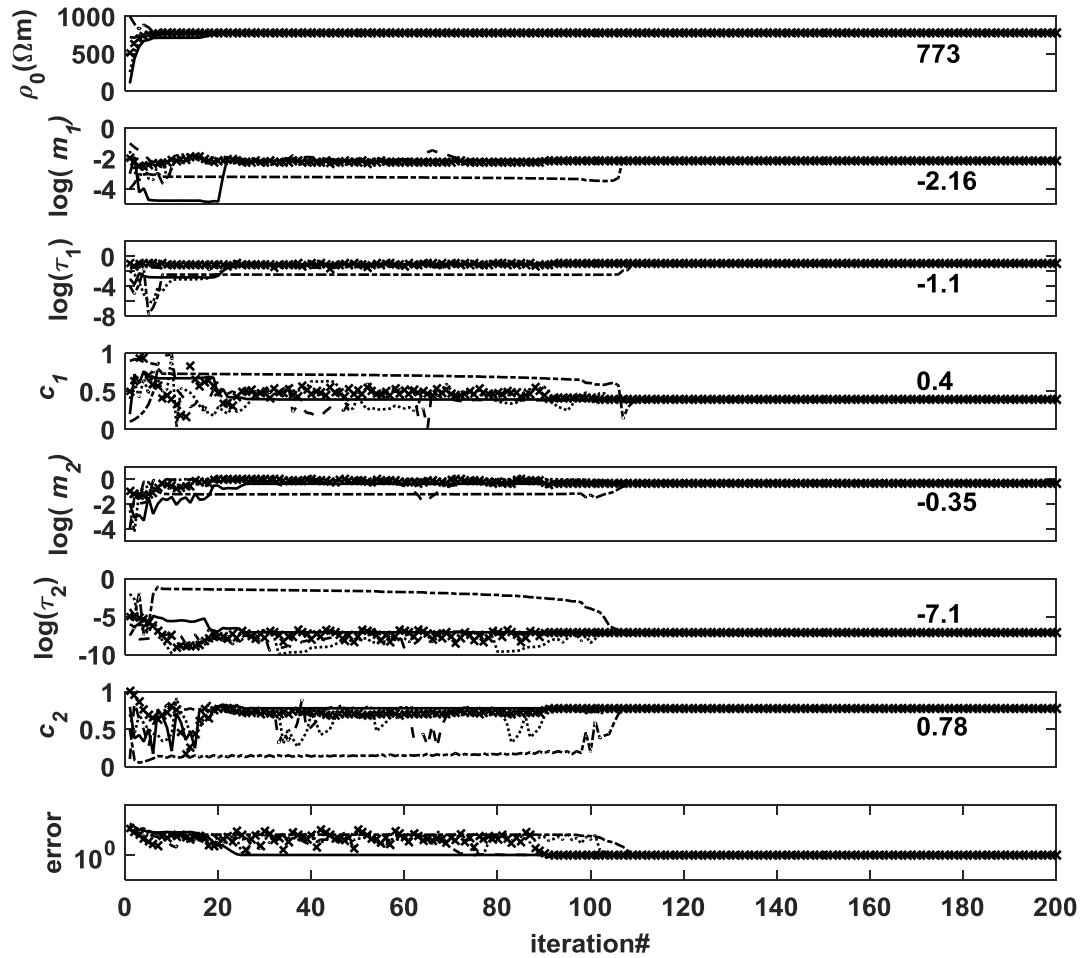


**Figure 3.6** Convergence of parameter estimates and error as a function of iteration for inversion of multi-frequency measurement of complex resistivity of an unconsolidated silica-sand sample, published by Kemna et al. (2000).

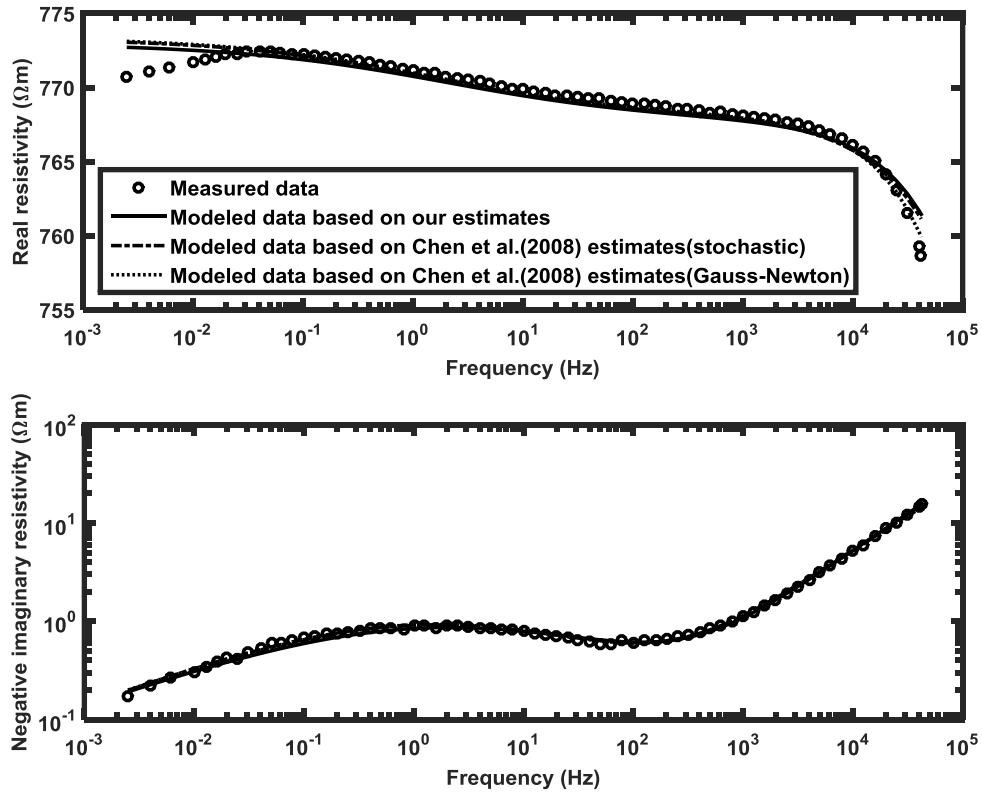


**Figure 3.7 Comparison of multi-frequency measurements of real and negative imaginary resistivity of an unconsolidated silica-sand sample against dual Cole-Cole model predictions based on inversion estimates.**

Table 3.3 compares the parametric estimates for the unconsolidated silica-sand sample by our proposed unified inversion algorithm and those obtained by Chen et al. (2008). The values of inverted parameters by our proposed unified inversion algorithm are almost all within the 95% highest probability domains (HPD) for stochastic method and 95% confidence interval (CI) in the Gauss-Newton method using initial guess close to stochastic inversion medians, which were both obtained by Chen et al. (2008). Although the Markov-chain Monte Carlo-based methods (stochastic methods) work well for a wide range of initial guesses, this method is computationally expensive. The initial guess for the deterministic Gauss-Newton-based inversion used by Chen et al. (2008) are:

$\rho_0 = 770.77 \Omega\text{m}$ ,  $m_1 = 0.001$ ,  $\log(\tau_1) = -1$  ( $\tau_1$  in s),  $c_1 = 0.5$ ,  $m_2 = 0.1$ ,  $\log(\tau_2) = -6$  ( $\tau_2$  in s), and  $c_2 = 1$ , which are close to the solution of the inversion problem.

**Table 3.3 Dual Cole-Cole resistivity model estimates for the silica-sand sample obtained using our proposed inversion method and those obtained by Chen et al. (2008).**

Cole-Cole model parameters	Our estimates	Chen <i>et al.</i> (2008) estimated medians based on stochastic method	95% HPD	Chen <i>et al.</i> (2008) estimates based on Gauss-Newton	95% CI
$\rho_0(\Omega\text{m})$	773	773.33	(772.38,774.37)	773.40	(752.96,794.39)
$m_1$	6.9e-3	6.9e-3	(6.7e-3,7e-3)	6.94e-3	(6.77e-3,7.11e-3)
$\log(\tau_1)$ ( $\tau_1$ in s)	-1.1	-0.972	(-1.005,-0.933)	-0.992	(-1.095,-0.889)
$c_1$	0.4	0.423	(0.413,0.433)	0.418	(0.406,0.429)
$m_2$	0.45	0.671	(0.305,1)	0.129	(0,0.262)
$\log(\tau_2)$ ( $\tau_2$ in s)	-7.1	-7.462	(-7.734,-6.948)	-6.406	(-7.989,-4.823)
$c_2$	0.78	0.736	(0.719,0.754)	0.765	(0.725,0.804)



## **Chapter 4: Joint Broadband Conductivity and Permittivity Logs Inversion**

### **4.1 Introduction to different EM log tools and limitation of this work**

Laterolog tools are used in conductive borehole environments and operated at few discrete frequencies lower than 10 kHz with a depth of investigation ranging from 30 inches to 90 inches. EM induction tools have similar depth of investigation as the laterolog tools, and they are designed primarily for resistivity measurements in wells drilled with moderately conductive muds or oil-based mud. EM induction tools typically operate at two discrete frequencies between 10 kHz and 60 kHz. Laterolog tool measures voltage potential at electrodes and induction tool measures the secondary voltage induced in the receiver coil that are converted to the resistivity (inverse of conductivity) of the formation. EM propagation resistivity tools generally operate at two discrete frequencies between 400 kHz and 2 MHz. EM propagation tools measure the attenuation, phase shift, and travel time for EM waves traveling through the formation from source to receiver located in the tool body. The new-generation EM dielectric dispersion tool operate at multiple frequencies in the range of 10 MHz to 1GHz. Dielectric tools can measure continuous dielectric dispersion logs at 1-in vertical resolution and are suitable for low salinity, low contrast, carbonate, and heavy oil reservoirs. EM propagation and dielectric tools measure attenuation and phase shift that is transformed to effective conductivity and permittivity at multiple frequencies.

The broadband conductivity and permittivity logs can be obtained by using combination of EM logging tools. In this chapter, we applied a mechanistic model (PS model) to process the broadband EM dispersion logs and the petrophysical parameters such as water saturation estimations can be obtained. PS model is a frequency-dependent

effective medium model and can be used to process multifrequency EM data. However, the EM dispersion logs are obtained by different EM tools which has different depth of investigation and vertical resolution. The vertical resolution of dielectric dispersion log is only 1-in, while for laterolog or EM induction tool the vertical resolution is more than 1 ft. The inversion-based interpretation method doesn't consider these effects and this method can only be applied in homogeneous formations. For formations that have thin-bed layers, the method can't be applied to estimate petrophysical parameters.

#### **4.2 Literature review of EM log inversion**

A joint inversion of galvanic resistivity (laterolog) and EM induction log was proposed by Mezzatesta et al. (1994) to improve the resolution of true formation resistivity estimates for improved evaluation of residual and movable hydrocarbon saturation. Glinskikh et al. (2014) implemented the Nelder-Mead simplex (direct search) algorithm coupled with dispersed clay mixing models (de Lima and Sharma, 1990) for petrophysical inversion of high frequency induction logs in the range between 0.875 and 14 MHz acquired in a shaly sandstone formation in oilfields of West and East Siberia to estimate water saturation, porosity and clay fraction in the formation. LWD propagation deep resistivity tool operating at 125 kHz, 500 kHz and 2 MHz, was implemented to drill a high-angle well in a carbonate reservoir in onshore Abu Dhabi (Al-Ameri et al., 2015). They implemented an inversion technique to estimate the horizontal resistivity, vertical resistivity, and dip angle by minimizing a cost function consisting of the sum of data misfit and sum of constraints of formations models. In the inversion scheme, Levenberg-Marquardt algorithm (LMA) was preferred over the steepest-descent method to increase

the speed of inversion. Hizem et al. (2008) used CRI model and SMD model to jointly invert the four-frequency dielectric dispersion logs in the range of 20 MHz to 1GHz to estimate the water saturation, formation water conductivity, and textural parameters. Han et al. (2017) combined Lichtenecker-Rother model and SMD model to process the four-frequency dielectric dispersion logs for estimating water saturation, brine conductivity, homogeneity index and cementation index in Bakken Petroleum System.

Various inversion algorithms have been developed to process the conductivity (resistivity) and permittivity measurements. The least square method is widely used and  $L2$  norm objective function can include the data misfit term, regularization term (Al Marzooq et al., 2014), and constraints of formations models (Al-Ameri et al., 2015). The  $L2$  norm objective function may only contain data misfit term (e.g. Lin et al., 1984). The Levenberg-Marquardt type algorithms have been implemented as the least square method in EM induction log inversion (Lin et al., 1984), LWD propagation resistivity log inversion (Al-Ameri et al., 2015) and multifrequency complex conductivity lab measured data inversion (Revil et al., 2015). Other inversion algorithms used to process the conductivity (resistivity) and permittivity data are Nelder-Mead simplex (direct search) algorithm (Glinskikh et al., 2014) and a combination of modified Gauss-Newton method and Monte Carlo algorithm (Zhou et al., 2016). Thiel et al. (2012) developed a robust Gauss-Newton inversion algorithm by introducing Huber error function to handle outliers in LWD propagation log measurements. The Huber function behaves like the  $L2$  norm for small error values and approaches the  $L1$  norm for large error values. In this section, we propose a modified LMA-based inversion method coupled with PS model (Misra et al., 2016a) to simultaneously process multifrequency permittivity and conductivity logs

acquired in the broadband frequency range of 1 kHz to 1 GHz. The proposed inversion algorithm has good convergence for wide range of initial guesses and the algorithm can be generalized because we identified a set of fixed parameters required for the robust and reliable joint inversion.

### 4.3 Modified Levenberg-Marquardt inversion algorithm

We modified the Levenrg-Marquardt inversion algorithm and the proposed inversion algorithm coupled with a mechanistic model (PS model) is applied to process the broadband EM dispersion logs to estimate the petrophysical parameters. In synthetic inversion cases, we introduce the data weight matrix which ensures that the error-minimization process equally honors all data misfits, and scaling matrix which scales the different parameters. In field data inversion cases, the standard deviations of relative permittivity and conductivity logs are included in the inversion scheme.

The nonlinear inverse problem discussed in this chapter involves the estimation of 3-5 PS model parameters that generate least misfit between the measured logs and the PS model predictions of multi-frequency effective permittivity and conductivity of clay- and pyrite-bearing formations. To demonstrate the efficacy of the proposed inversion scheme, synthetic logs with 5% Gaussian noise are simulated using the PS model at the log-acquisition frequencies of various combinations of the four aforementioned EM tools for pyrite- and clay-bearing formations.

In the proposed inversion scheme,  $n$ -sized measured data vectors **Perm**<sup>meas</sup> and **Cond**<sup>meas</sup> represent the log-derived or synthetically generated effective permittivity and conductivity values of a pyrite- and clay-bearing formation acquired at  $n$  distinct EM log-

acquisition angular frequencies, namely,  $\omega_1, \omega_2, \dots, \omega_n$ . The goal is to estimate  $l$ -sized PS model parameter vector  $\mathbf{m}^{\text{prop}}$  that best represents the petrophysical properties, such as water saturation, brine salinity, clay surface conductance, and average size of IP-causing grains, of the subsurface formation under investigation. To that end, PS model is used to generate the  $n$ -sized modeled data vectors  $\mathbf{Perm}^{\text{mod}}(\mathbf{m})$  and  $\mathbf{Cond}^{\text{mod}}(\mathbf{m})$ , comprising PS model predictions at  $n$  distinct log-acquisition frequencies for a specific  $l$ -sized PS model parameter vector  $\mathbf{m}$ . The modeled data vectors can be expressed as

$$\mathbf{Perm}^{\text{mod}}(\mathbf{m}) = [Perm(\mathbf{m}, \omega_1), Perm(\mathbf{m}, \omega_2), \dots, Perm(\mathbf{m}, \omega_n)] \dots \dots \dots (4.1)$$

and

$$\mathbf{Cond}^{\text{mod}}(\mathbf{m}) = [Cond(\mathbf{m}, \omega_1), Cond(\mathbf{m}, \omega_2), \dots, Cond(\mathbf{m}, \omega_n)] \dots \dots \dots (4.2)$$

where the PS model-generated  $Perm(\mathbf{m}, \omega_i)$  and  $Cond(\mathbf{m}, \omega_i)$  represent the modeled effective permittivity and conductivity of a pyrite- and clay-bearing formation computed at a specific log-acquisition angular frequency  $\omega_i$  for a specific  $l$ -sized PS model parameter vector  $\mathbf{m}$ . Following that, the modeled data vectors  $\mathbf{Perm}^{\text{mod}}(\mathbf{m}^{\text{est}})$  and  $\mathbf{Cond}^{\text{mod}}(\mathbf{m}^{\text{est}})$  are matched with the measured data vectors  $\mathbf{Perm}^{\text{meas}}$  and  $\mathbf{Cond}^{\text{meas}}$  to find the PS model parameter  $l$ -sized vector  $\mathbf{m}^{\text{est}}$  that best characterizes the pyrite- and clay-bearing formation under investigation.

We defined an  $n$ -sized data misfit vector  $\mathbf{F}(\mathbf{m})$  for purposes of minimization. Individual components of the vector  $\mathbf{F}(\mathbf{m})$  are referred as  $f_i(\mathbf{m}^k)$ , where superscript  $k$  is used as the iteration count for the inversion scheme,  $\mathbf{m}^k$  is the  $l$ -sized PS model parameter vector computed at the  $k$ -th iteration of the inversion, and subscript  $i$  denotes one of the  $n$  log-acquisition frequencies.  $\mathbf{F}(\mathbf{m}^k)$  is thus expressed as

$$\mathbf{F}(\mathbf{m}^k) = [f_1(\mathbf{m}^k), f_2(\mathbf{m}^k), \dots, f_n(\mathbf{m}^k)]^T \dots \dots \dots (4.3)$$

where  $f_i(\mathbf{m}^k)$  is expressed as

$$f_i(\mathbf{m}^k) = [\mathbf{Perm}^{\text{mod}}(\mathbf{m}^k) - \mathbf{Perm}^{\text{meas}}]_i^2 + [\mathbf{w} \cdot (\mathbf{Cond}^{\text{mod}}(\mathbf{m}^k) - \mathbf{Cond}^{\text{meas}})]_i^2 \dots \dots \dots (4.4)$$

where  $i = 1, 2, \dots, n$  and  $\mathbf{w}$  is the  $n$ -sized weight factor vector formulated as

$$\mathbf{w} = \frac{\mathbf{Perm}^{\text{meas}}}{\mathbf{Cond}^{\text{meas}}} \dots \dots \dots (4.5)$$

The weight factor vector in Eq. 4.5 is used to normalize the errors in effective permittivity and conductivity to ensure that the inversion scheme equally honors both the errors in conductivity and permittivity. For the synthetic cases studied in this paper, the elements of weight factor vector are typically in the range of 20-700 at log-acquisition frequencies of dielectric tools,  $1 \times 10^3$  to  $2 \times 10^4$  at propagation log-acquisition frequencies, and  $1 \times 10^5$  to  $1 \times 10^6$  at induction log acquisition frequencies.

We modified the LMA by introducing  $n \times n$  data weight matrix  $\mathbf{W}_d$  and  $l \times l$  scaling matrix  $\mathbf{W}_s$  into the mathematical formulation of the LMA inversion scheme. During the error-minimization process of an inversion scheme, the total data misfit, computed based on the inversion-derived estimates, is a function of data misfits computed at each frequency of the EM measurement. The weight-factor vector  $\mathbf{w}$  ensures that the data misfit at a given frequency equally honors the measured/modeled values of permittivity and conductivity. On the other hand, the  $\mathbf{W}_a$  matrix ensures that the error-minimization process equally honors all data misfits computed at each of the EM-measurement frequencies. To that end,  $\mathbf{W}_a$  scales the data-misfit vector  $\mathbf{F}(\mathbf{m})$ , whereas the vector  $\mathbf{w}$  scales the errors in permittivity and conductivity components at any given frequency. The data at low frequencies get more weight compared to those at high frequencies without

the  $\mathbf{W}_d$  matrix, whereas permittivity components get more weight compared to the conductivity components without vector  $\mathbf{w}$ .

To ensure the generality of the inversion algorithm, we did not implement a reference vector  $\mathbf{m}_R$ , which represents the prior knowledge of parameter values that mitigates the non-uniqueness issues in the modified LMA. The modified LMA scheme used for error minimization is expressed as

$$[(\mathbf{W}_d \mathbf{J}(\mathbf{m}^k) \mathbf{W}_s)^T \cdot (\mathbf{W}_d \mathbf{J}(\mathbf{m}^k) \mathbf{W}_s) + \lambda \mathbf{I}] \cdot \mathbf{W}_s^{-1} \cdot \Delta \mathbf{m}^k = -(\mathbf{W}_d \mathbf{J}(\mathbf{m}^k) \mathbf{W}_s)^T \cdot (\mathbf{W}_d \mathbf{F}(\mathbf{m}^k)) \dots \dots \dots (4.6)$$

where  $\mathbf{J}(\mathbf{m}^k)$  is the  $n \times l$  Jacobian matrix derived of  $\mathbf{F}(\mathbf{m}^k)$ ,  $\mathbf{I}$  is  $l \times l$  identity matrix, superscript T is matrix transpose operator,  $\Delta \mathbf{m}^k$  is the  $l$ -sized correction vector generated at the  $k$ -th iteration that determines the direction towards the convergence of the unknown PS-model parameters during the estimation process, and  $\lambda$  is the damping parameter, which is adaptively adjusted by a constant damping factor  $\nu$  during the course of the iteration to ensure faster convergence. Based on the damping parameter, the proposed modified LMA interpolates between Gauss-Newton algorithm (GNA) and gradient descent method. We applied the same values of damping parameter  $\lambda$  and constant damping factor  $\nu$  in all cases in Chapter 4 as those in Chapter 3. The Jacobian matrix  $\mathbf{J}(\mathbf{m}^k)$  is formulated in the same form as it in Chapter 3. Using the correction vector generated in Eq. 4.6, we can calculate the successive estimates for the unknown PS-model parameters as

$$\mathbf{m}^{k+1} = \mathbf{m}^k + \Delta \mathbf{m}^k \dots \dots \dots (4.7)$$

such that all elements of the  $l$ -sized vector  $\mathbf{m}^{k+1}$  lie within the predefined lower and upper limits. The way to define the bounds of PS model parameters and the jump-back-in step are similar to those in Chapter 3.

The matrix  $\mathbf{W}_d$  is the  $n \times n$  data weight matrix which is a diagonal matrix with elements equal to the inverse of the sum of measured effective permittivity square and weighted conductivity square formulated as

$$\mathbf{W}_d = \begin{pmatrix} \frac{1}{(\text{Perm}^{\text{meas}})_1^2 + (\mathbf{w} \cdot \text{Cond}^{\text{meas}})_1^2} & \cdots & 0 \\ \vdots & \ddots & \vdots \\ 0 & \cdots & \frac{1}{(\text{Perm}^{\text{meas}})_n^2 + (\mathbf{w} \cdot \text{Cond}^{\text{meas}})_n^2} \end{pmatrix} \dots\dots\dots(4.8)$$

In several published inversion schemes, the weight matrix  $\mathbf{W}_d$  is the inverse of the data covariance matrix (e.g., Torres-Verdín et al., 2000) describing the estimated variance for each particular measurement and the estimated correlation between measurements or the estimated uncertainties in the data due to noise contamination. However, in our inversion scheme, the only function of proposed formulation of  $\mathbf{W}_d$  is to scale the effective permittivity and conductivity at various logging frequency. Scaling is required because the effective permittivity at galvanic resistivity tool frequency is nearly 4 orders of magnitude larger than that at the highest dielectric dispersion tool frequency and the effective conductivity at highest dielectric dispersion frequency is generally 2 orders of magnitude larger than that at galvanic tool frequency.

$\mathbf{W}_s$  is  $l \times l$  scaling diagonal matrix that ensures that the Jacobian matrix in Equation 6 remains non-singular during the inversion iterations.  $\mathbf{W}_s$  is expressed as

$$\mathbf{W}_s = \begin{pmatrix} 10^{\alpha_1} & \cdots & 0 \\ \vdots & \ddots & \vdots \\ 0 & \cdots & 10^{\alpha_l} \end{pmatrix} \dots\dots\dots(4.9)$$



where the parameters  $(\alpha_1, \alpha_2, \dots, \alpha_l)$  are the exponents in the diagonal denote the order of magnitude difference between the expected estimates for the  $l$  unknown PS-model parameters. The values of  $\alpha_1, \alpha_2, \dots, \alpha_l$  correspond to the unknown PS-model parameters, namely water saturation, brine conductivity, surface conductance of clay, clay grain size, and pyrite grain size, that was assumed to be -1, 0, -6, -6, and -4, respectively, for the cases investigated in this paper. Without the first-of-its-kind scaling matrix  $\mathbf{W}_s$ , the Jacobian matrix tends to become singular or badly scaled during the inversion iteration. There can be an order of 6 variation in the magnitudes of PS model parameters; consequently, without the scaling matrix, the inversion scheme can generate inconsistent estimates for some parameters because the corresponding elements in the Jacobian matrix tend to become much larger than the other elements. Rather than scaling parameters in the first, we propose another way to scale parameters by introducing the scaling matrix into the inversion scheme. For example, the range of water saturation is between 0 to 1 and the range of surface conductance is between  $1 \times 10^{-8}$  S to  $1 \times 10^{-5}$  S, which is 5 orders of magnitude variation in the parameter values. In such a case,  $\alpha_1$  corresponding to water saturation is assumed to be -1 and  $\alpha_3$  corresponding to surface conductance of clay is assumed to be -6.

#### **4.4 Synthetic case study**

Synthetic data inversion was applied on three specific synthetic layers. Table 4.1 displays the assumed petrophysical properties of the three synthetic formations. Synthetic Layer 1 is a pyrite-rich and smectite-type conductive clay-bearing oil-filled formation; Synthetic Layer 2 is a pyrite-rich and kaolinite-type nonconductive clay-rich water-filled

formation; and Synthetic Layer 3 is a smectite-type conductive clay-rich brine-filled formation.

**Table 4.1 Assumed petrophysical properties of the three synthetic layers used for this study. The parameters shown with a gray background were also used as the inversion-derived estimates.**

Parameters	Unit	Layer 1	Layer 2	Layer 3
Volume fraction of pyrite grains, $V_i$	%	5	3	1
Bulk conductivity of pyrite, $S_i$	S/m	1000	5000	1000
Relative permittivity of pyrite, $\epsilon_{ri}$		30	30	30
Diffusion coefficient of pyrite, $D_i$	m <sup>2</sup> /s	10 <sup>-6</sup>	5×10 <sup>-6</sup>	10 <sup>-6</sup>
Radius of pyrite grains, $r_i$	μm	30	100	50
Volume fraction of clay, $V_c$	%	30	60	50
Relative permittivity of clay, $\epsilon_{rc}$		5	5	5
Surface conductance of clay, $\lambda_c$	S	5×10 <sup>-6</sup>	10 <sup>-6</sup>	5×10 <sup>-6</sup>
Radius of spherical clay grains, $r_c$	μm	0.3	1	0.5
Volume fraction of sand, $V_s$	%	45	20	30
Surface conductance of sand, $\lambda_s$	S	10 <sup>-9</sup>	10 <sup>-9</sup>	10 <sup>-9</sup>
Radius of sand grains, $r_s$	μm	500	500	500
Porosity of rock, $\phi$	%	20	17	19
Bulk conductivity of brine, $C_w$	S/m	3	1	10
Relative permittivity of brine, $\epsilon_{rb}$		80	80	80
Diffusion coefficient of brine, $D_b$	m <sup>2</sup> /s	10 <sup>-9</sup>	10 <sup>-9</sup>	2×10 <sup>-9</sup>
Relative permittivity of hydrocarbon, $\epsilon_{rhy}$		3	3	3
Water saturation, $s_w$	%	20	90	80

*Case 1: Inversion of synthetic data generated at laterolog, induction, propagation and dielectric dispersion frequencies without Gaussian noise*

The inversion method was applied to synthetic effective permittivity and conductivity data for a pyrite- and clay-bearing formation generated using the PS model at laterolog (1kHz), induction (26 kHz, 52 kHz), propagation (400 kHz, 2 MHz) and dielectric (20 MHz, 100 MHz, 400 MHz, 1 GHz) log-acquisition frequencies. This presents an ideal situation when effective conductivity and permittivity of a given depth in a pyrite- and clay-bearing geological formation are measured at 9 frequencies using the four EM downhole tools available in the industry. For this comparative study, the synthetic data is generated for a formation that is assumed to be similar to Synthetic Layer

1, which is pyrite-rich and smectite-type conductive clay-bearing oil-filled formation. The method was tested for its accuracy in estimating  $s_w$ ,  $C_w$ ,  $\lambda_c$ ,  $r_c$ , and  $r_i$ . Fig. 4.1 shows the synthetic effective permittivity and conductivity data generated using PS model at four aforementioned EM logs frequencies. When plotting the relative permittivity as a function of frequency, logarithmic scale is used in y-axis that compresses the effect of noise in permittivity.

The inversion-derived estimates successfully converged after 13 iterations for broad range of initial guesses of  $s_w$ ,  $C_w$ ,  $\lambda_c$ ,  $r_c$ , and  $r_i$  in the ranges of 0.1 to 0.9, 0.5 to 10 S/m,  $5 \times 10^{-7}$  to  $1 \times 10^{-5}$  S, 0.1 to 3  $\mu\text{m}$ , and 10 to 300  $\mu\text{m}$ , respectively. Our estimates for the five unknown PS model parameters are:  $s_w = 0.2$ ,  $C_w = 3$  S/m,  $\lambda_c = 5 \times 10^{-6}$  S,  $r_c = 0.3$   $\mu\text{m}$ , and  $r_i = 30$   $\mu\text{m}$ . These estimates match well with the original parameter values, listed in Table 4.1, assumed for Synthetic Layer 1, which were used to generate the synthetic data without Gaussian noise shown in Fig. 4.1. The PS model prediction based on our estimates of the five parameters match the synthetic effective permittivity and conductivity with relative error of less than  $1 \times 10^{-6}$ . The bounds of the unknown PS model petrophysical parameters during inversion were:  $0 \leq s_w \leq 1$ ,  $0 \leq C_w \leq 15$  S/m,  $1 \times 10^{-8} \leq \lambda_c \leq 1 \times 10^{-5}$  S,  $0 \leq r_c \leq 10$   $\mu\text{m}$ , and  $1 \leq r_i \leq 1000$   $\mu\text{m}$ . Contour plots in Fig. 4.2(A) and 4.2(B) depict LMA-based inversion method in terms of error minimization for a specific set of initial guesses of the model parameters, namely  $s_w = 0.5$ ,  $C_w = 7$  S/m,  $\lambda_c = 5 \times 10^{-7}$  S,  $r_c = 0.2$   $\mu\text{m}$ , and  $r_i = 50$   $\mu\text{m}$ . The contours present relative error of data misfit in logarithmic scale; for example, contour of -1 indicates a relative error of 0.1. Fig. 4.2(A) illustrates the changes in water saturation and brine conductivity estimates and Fig. 4.2(B) illustrates the changes in the estimates of clay properties: surface

conductance of clay and radius of spherical clay grains during the first 15 iterations that resulted in the convergence of inversion-derived estimates. To avoid repetition in reporting the observed trends, we do not present the changes in the estimates of radius of pyrite grains.

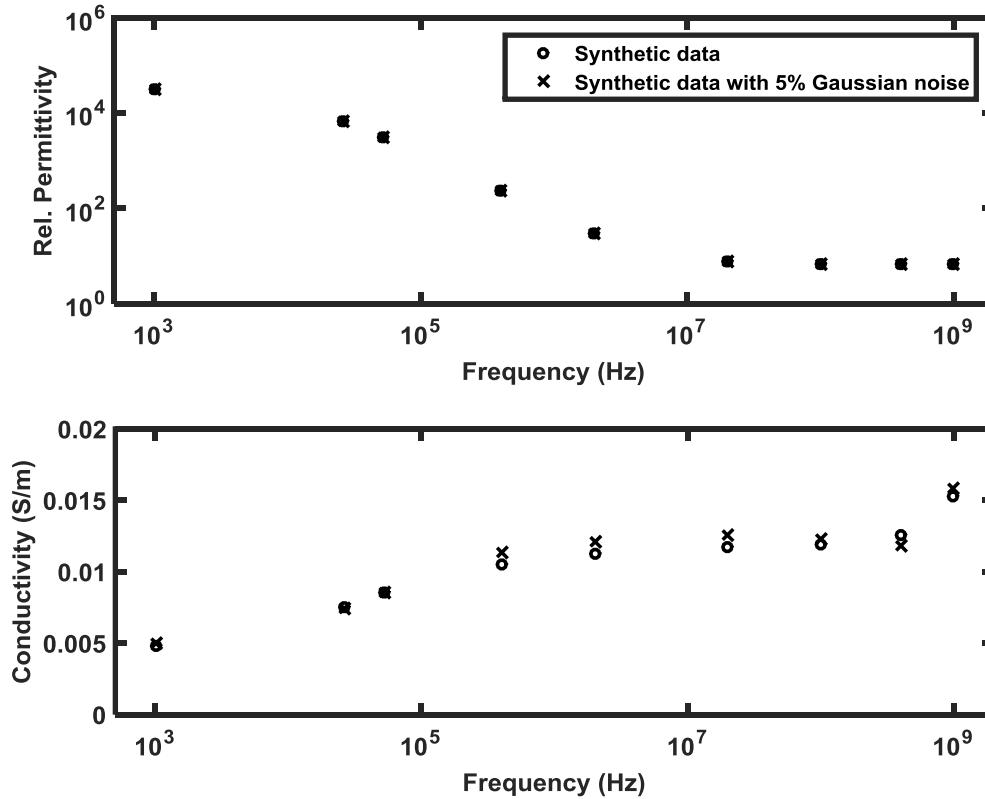


**Figure 4.1 Synthetic data with and without 5% Gaussian noise at one laterolog (~Hz), two induction (~kHz), two propagation (~MHz), and four dielectric frequencies (~MHz to 1 GHz) generated assuming parameters for Synthetic Layer 1.**

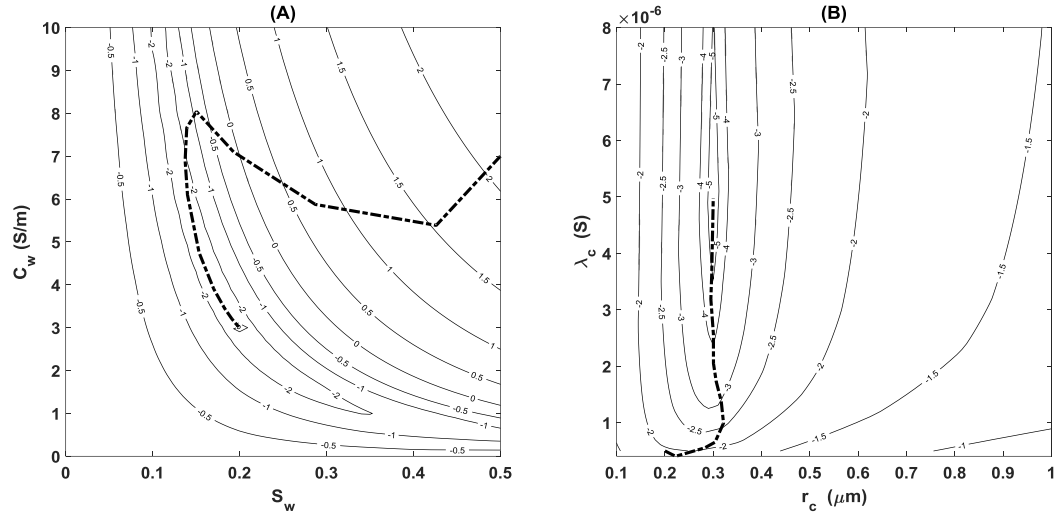


**Figure 4.2** Changes in (A) water saturation and brine conductivity estimates and those in (B) surface conductance of clay and radius of spherical clay with associated relative error of data misfit obtained during the modified LMA-based inversion of synthetic data shown in Fig. 4.1 (representing the conductivity and permittivity response of Synthetic Layer 1). The dash line identifies the estimates generated by the modified LMA. The start point for both the methods is  $S_w = 0.5$ ,  $C_w = 7$  S/m,  $\lambda_c = 5 \times 10^{-7}$  S,  $r_c = 0.2 \mu\text{m}$ , and  $r_i = 50 \mu\text{m}$ .

*Case 2: Inversion of synthetic data generated at laterolog, induction, propagation and dielectric dispersion frequencies with 5% Gaussian noise*

Fig. 4.3 shows that, in the presence of 5% Gaussian noise in the synthetic data (Fig. 4.1), the inversion-derived estimates for modified LMA successfully converged for the broad range of initial guesses, which is similar to that adopted for the previous case involving synthetic data without Gaussian noise. Row 1 in Tables 4.2-4.6 list the inversion-derived estimates obtained by processing the synthetic response of Synthetic Layer 1 containing 5% Gaussian noise. Water saturation estimates followed by brine conductivity estimates are generated at higher accuracy compared to the  $\lambda_c$ ,  $r_c$ , and  $r_i$  estimates. The modified LMA-based estimates for the five unknown PS model parameters are (also, listed in Tables 4.2-4.6)  $s_w = 0.201$ ,  $C_w = 2.97$  S/m,  $\lambda_c = 5.2 \times 10^{-6}$  S,  $r_c = 0.285 \mu\text{m}$ , and  $r_i = 35.4 \mu\text{m}$ . These estimates are close to the original parameter values, listed

in Table 4.1, assumed for Synthetic Layer 1 that were used to generate the synthetic data with 5% Gaussian noise, as shown in Fig. 4.1. The PS model prediction based on our estimates of the five parameters match the synthetic effective permittivity and conductivity with relative error of close to  $1 \times 10^{-2}$ .

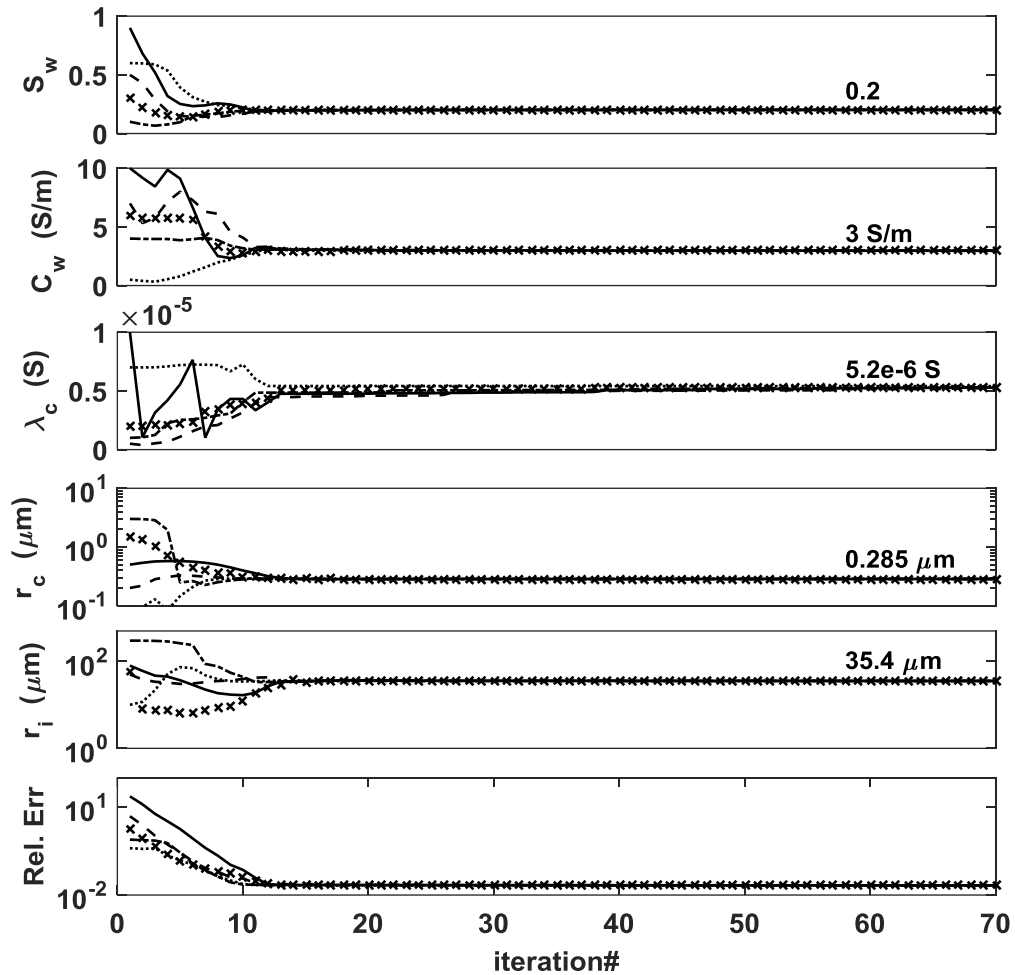


**Figure 4.3** Convergence of modified LMA-based inversion estimates of PS-model parameters and relative error (between modeled data based on the estimated parameters and the synthetic data) as a function of iteration during the inversion of synthetic data with 5% Gaussian noise generated for the Synthetic Layer 1. Inversion results for five different sets of initial guesses of the model parameters are shown in the figure.

*Case 3: Inversion of synthetic data generated at one induction and four dielectric dispersion frequencies with 5% Gaussian noise*

As mentioned earlier, a subsurface log acquisition plan generally does not involve all the four types of logging tools. There have been several oil-field log-acquisition efforts involving induction and dispersion logs (e.g., Pirrone et al., 2011; Han et al., 2017), induction and propagations logs (e.g., Altman et al., 2008; Misra et al., 2016c), and propagation and dispersion logs (e.g., Wang and Poppitt, 2013; Little et al., 2010). Notably, most of the existing induction log interpretation techniques only generate resistivity estimates and assume the permittivity of the formation to be 1 (Misra and Han, 2016a) that is unrealistic in the presence of large volume fractions of clays and pyrite. Application of the proposed inversion technique is challenging due to the following reasons: (1) the EM logs are acquired in a well at limited number of frequencies, generally between 2 to 5 frequencies (Han and Misra, 2017), (2) permittivity logs are not generated during the interpretation of laterolog and induction log interpretation, and (3) different volumes of a formation are investigated at different log-acquisition frequencies. Therefore, in this section, we apply the modified LMA-based inversion method to synthetic conductivity and permittivity data generated under the constraints of measurements obtained at less than 6 discrete frequencies and in absence of permittivity data at induction and laterolog frequencies, wherein the effective relative permittivity is assumed to be 1. The inversion algorithm is tested on synthetic data with 5% Gaussian noise.

Synthetic permittivity and conductivity data (Fig. 4.4) is generated using the PS model at one induction (26 kHz) and four dielectric (20 MHz, 100 MHz, 400 MHz, 1 GHz) log-acquisition frequencies. The proposed inversion algorithm is applied to the five-frequency synthetic data to estimate three model parameters, namely, water

saturation, bulk conductivity of brine, and surface conductance of clay. 5% Gauss noise to the synthetic effective permittivity and conductivity data, as shown in Fig. 4.4. Inversion-derived estimates for the three unknown PS model parameters assumed for this study are:  $s_w = 0.79$ ,  $C_w = 10.6$  S/m, and  $\lambda_c = 4.7 \times 10^{-6}$  S, which are reported in Tables 4.2-4.4 in and are close to the original parameter values, listed in Table 4.1, assumed for Synthetic Layer 3. The PS model predictions based on inversion-derived estimates of the three parameters match the synthetic effective permittivity and conductivity (with 5% Gauss noise) with relative error of less than  $3 \times 10^{-2}$ . Inversion-derived estimates for Synthetic Layer 3 are consistently less inaccurate compared to those for Synthetic Layer 1 because the data for Synthetic Layer 1 were acquired at 9 frequencies compared to 5 frequencies for Synthetic Layer 3.



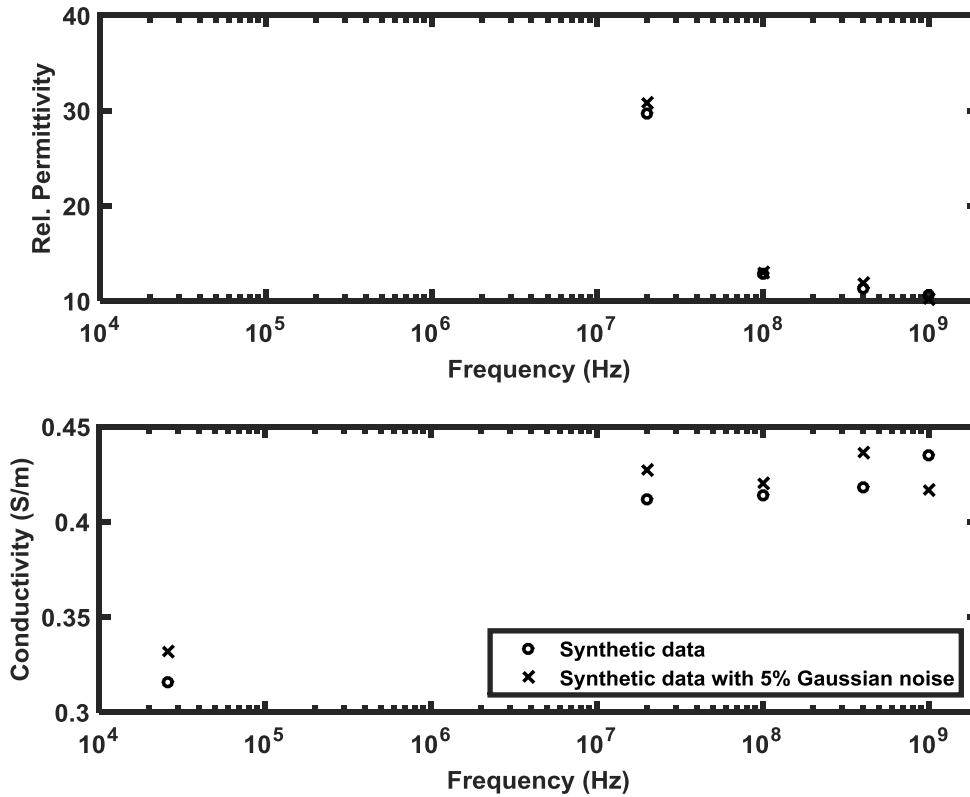


**Figure 4.4 Synthetic data with and without 5% Gaussian noise at one induction (~kHz) and four dielectric (~MHz to 1 GHz) frequencies generated assuming parameters of Synthetic Layer 3. Data at induction frequency does not have a corresponding relative permittivity value, in accordance with current practices in log acquisition.**

*Case 4: Inversion of synthetic data generated at two propagation and four dielectric dispersion frequencies with 5% Gaussian noise*

As mentioned earlier, there is oil-field log-acquisition effort to deploy EM propagation tool during logging while drilling (LWD) followed by dielectric dispersion tool as a wireline logging run. Such tool deployment in a well will typically provide conductivity and permittivity data at six frequencies in the range of 1 MHz to 1 GHz. In order to simulate this scenario, PS model is used to generate synthetic effective permittivity and conductivity data at propagation (400 kHz, 2 MHz) and dielectric (20

MHz, 100 MHz, 400 MHz, 1 GHz) log-operation frequencies acquired in a pyrite- and clay-bearing formations. Parameters mentioned in Table 4.1 for the Synthetic Layer 2 are used as default parameters and the objective of inversion of the six-frequency synthetic data is to accurately estimate the  $s_w$ ,  $C_w$ ,  $\lambda_c$ , and  $r_c$ . Fig. 4.5 shows the synthetic effective permittivity and conductivity data predicted by PS model for Synthetic Layer 2 at propagation and dielectric dispersion log acquisition frequencies.

Our estimates for the four PS model parameters are:  $s_w = 0.89$ ,  $C_w = 1.03$  S/m,  $\lambda_c = 1.05 \times 10^{-6}$  S, and  $r_c = 1.03 \mu\text{m}$ , which are reported in Tables 4.2 – 4.5 and are close to the original parameter values, listed in Table 4.1, assumed for Synthetic Layer 2 that were used to generate the synthetic data shown in Fig. 4.5. The PS model prediction based on our estimates of the four parameters match the synthetic effective permittivity and conductivity with relative error of less than  $5 \times 10^{-2}$ . Inversion-derived estimates for Synthetic Layer 2 are consistently less inaccurate compared to those for Synthetic Layer 1 because the data for Synthetic Layer 1 were acquired at 9 frequencies compared to 6 frequencies for Synthetic Layer 2.

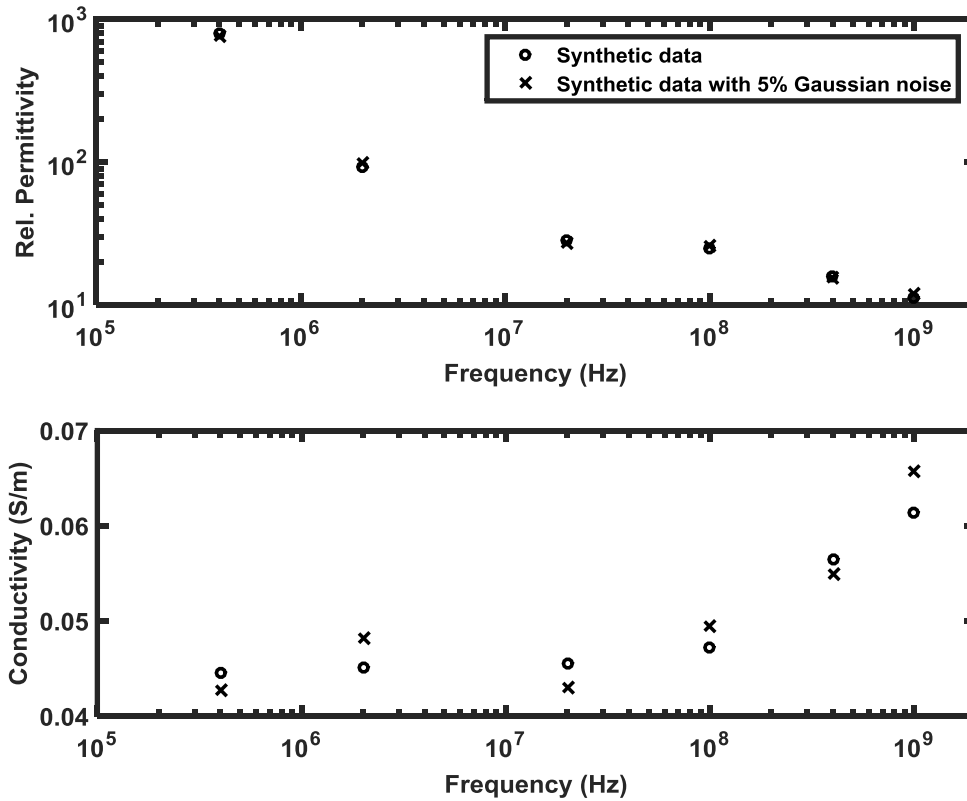


**Figure 4.5 Synthetic data with and without 5% Gaussian noise at two propagation (~MHz) and four dielectric (~MHz to 1 GHz) frequencies generated assuming parameters of Synthetic Layer 2.**

**Table 4.2 Relative errors in water saturation estimates obtained using the joint inversion of multifrequency conductivity and permittivity data containing 5% Gaussian noise for three synthetic layers.**

Synthetic Layer	Estimated $s_w$	True $s_w$	Error in $s_w$ (%)
1	0.201	0.2	0.65
2	0.89	0.9	1.1
3	0.79	0.8	1.25

**Table 4.3 Relative errors in brine conductivity estimates obtained using the joint inversion of multifrequency conductivity and permittivity data containing 5% Gaussian noise for three synthetic layers.**

Synthetic Layer	Estimated $C_w$ (S/m)	True $C_w$ (S/m)	Error in $C_w$ (%)
1	2.97	3	1
2	1.03	1	3
3	10.6	10	6

**Table 4.4 Relative errors in clay surface conductance estimates obtained using the joint inversion of multifrequency conductivity and permittivity data containing 5% Gaussian noise for three synthetic layers.**

Synthetic Layer	Estimated $\lambda_c$ (S)	True $\lambda_c$ (S)	Error in $\lambda_c$ (%)
1	$5.2 \times 10^{-6}$	$5 \times 10^{-6}$	4
2	$1.05 \times 10^{-6}$	$1 \times 10^{-6}$	5
3	$4.7 \times 10^{-6}$	$5 \times 10^{-6}$	6

**Table 4.5 Relative errors in clay radius estimates obtained using the joint inversion of multifrequency conductivity and permittivity data containing 5% Gaussian noise for two synthetic layers.**

Synthetic Layer	Estimated $r_c$ ( $\mu\text{m}$ )	True $r_c$ ( $\mu\text{m}$ )	Error in $r_c$ (%)
1	0.285	0.3	5
2	1.03	1	3

**Table 4.6 Relative errors in pyrite radius estimates obtained using the joint inversion of multifrequency conductivity and permittivity data containing 5% Gaussian noise for one synthetic layer.**

Synthetic Layer	Estimated $r_i$ ( $\mu\text{m}$ )	True $r_i$ ( $\mu\text{m}$ )	Error in $r_i$ (%)
1	35.4	30	18

#### 4.5 Application in organic-rich gas shale formation

Broadband EM measurements in the frequency range of 1 Hz to 1 GHz are generally performed on geological core samples in laboratory environment. However, there is only one example of subsurface broadband EM dispersion data acquisition reported by Wang and Poppitt (2013), which was processed later by Han and Misra (2017). Wireline induction logging tool operating at 26 kHz, LWD propagation logging tool operating at 1 MHz and 2 MHz, and wireline dielectric-dispersion logging tool operating at 20 MHz, 100 MHz, 260 MHz, and 1 GHz were deployed in an organic-rich shale formation in Northern Europe for acquiring broadband conductivity- and permittivity-dispersion logs. We improved and revised the proposed inversion algorithm for inverting this broadband conductivity and permittivity dispersion logs. In this field

case, contrary to conventional acquisition practices, permittivity log was acquired at the induction-log acquisition frequency.

Data misfit vector for field data inversion was modified because the standard deviations of relative permittivity and conductivity logs are notably different. In doing so, the inversion scheme requires minimizing quadratic cost function  $C(\mathbf{m})$  formulated as

$$C(\mathbf{m}) = \left\| \frac{\mathbf{D}^{\text{mod}}(\mathbf{m}^{\text{est}}) - \mathbf{D}^{\text{meas}}}{\boldsymbol{\sigma}} \right\|_2^2 \dots \dots \dots (4.10)$$

where  $\mathbf{D}^{\text{mod}}(\mathbf{m}^{\text{est}})$  represents modeled data vector based on estimated model parameters,  $\mathbf{D}^{\text{meas}}$  represents the measured data vectors, and  $\boldsymbol{\sigma}$  is the standard deviation vector for the broadband permittivity and conductivity logs. The first seven elements in the vectors are related to permittivity, and the remaining seven are related to conductivity for the seven frequencies of measurement. The data misfit vector  $\mathbf{F}'(\mathbf{m})$  is thus expressed as a combination of 7 conductivity and 7 permittivity measurements in the broadband frequency as follows -

$$\mathbf{F}'(\mathbf{m}^k) = [f'_1(\mathbf{m}^k), f'_2(\mathbf{m}^k), \dots, f'_{14}(\mathbf{m}^k)]^T \dots \dots \dots (4.11)$$

where  $f'_i(\mathbf{m}^k)$  is expressed as

$$f'_i(\mathbf{m}^k) = \frac{\mathbf{D}^{\text{mod}}(\mathbf{m}^{\text{est}})_i - \mathbf{D}^{\text{meas}}_i}{\sigma_i} \dots \dots \dots (4.12)$$

where  $i = 1, 2, \dots, 14$ , where the first seven elements ( $i = 1, 2, \dots, 7$ ) are related to permittivity measurements and the remaining seven elements ( $i = 8, 9, \dots, 14$ ) are related to conductivity measurements. The elements in data misfit vector  $\mathbf{F}'(\mathbf{m})$  are in similar order of magnitude after dividing the broadband permittivity and conductivity logs with the standard deviation vector into the cost function. Therefore, the weight

matrix  $\mathbf{W}_d$  and weight factor  $\mathbf{w}$  are not needed for the field case study. For the field case study, the modified Levenberg-Marquardt inversion scheme is revised to

$$[(\mathbf{J}(\mathbf{m}^k)\mathbf{W}_s)^T \cdot (\mathbf{J}(\mathbf{m}^k)\mathbf{W}_s) + \lambda\mathbf{I}] \cdot \mathbf{W}_s^{-1} \cdot \Delta\mathbf{m}^k = -(\mathbf{J}(\mathbf{m}^k)\mathbf{W}_s)^T \cdot (\mathbf{F}(\mathbf{m}^k)) \dots \dots \dots (4.13)$$

We selected two depths in the organic-rich shale formation under investigation. XX09 m is a pyrite- and clay-rich zone and XX52 m is clay rich zone. The joint petrophysical inversion algorithm processed the broadband conductivity and permittivity dispersion logs acquired at these two depths. Table 4.7 displays the  $s_w$ ,  $C_w$ ,  $\lambda_c$ ,  $r_c$  and  $r_i$  estimates and other petrophysical properties for these two depths. Based on the estimations, depth XX09 m is low salinity, water-bearing zone, whereas depth XX52 m is low-salinity, oil-bearing zone. For those two depths, the radius of clay is around 0.1  $\mu\text{m}$  and surface conductance of clay is low, which is lower than  $1 \times 10^{-7}$  S. The radius of pyrite in depth XX09 m is around 170  $\mu\text{m}$ .

**Table 4.7 Inversion-derived and assumed petrophysical properties of two depths in the organic-rich formation. Joint inversion of induction, propagation and dielectric dispersion logs was performed at the two depths. The five inversion-derived estimates are shown with a gray background.**

Parameters	Unit	Depth XX52	Depth XX09
Volume fraction of pyrite grains, $V_i$	%	0	2.3
Bulk conductivity of pyrite, $S_i$	S/m	-	1000
Relative permittivity of pyrite, $\epsilon_{ri}$		-	30
Diffusion coefficient of pyrite, $D_i$	$\text{m}^2/\text{s}$	-	$1 \times 10^{-5}$
Radius of pyrite grains, $r_i$	$\mu\text{m}$	-	172
Volume fraction of clay, $V_c$	%	60	47
Relative permittivity of clay, $\epsilon_{rc}$		6	6
Surface conductance of clay, $\lambda_c$	S	$6.6 \times 10^{-8}$	$2.5 \times 10^{-8}$
Radius of spherical clay grains, $r_c$	$\mu\text{m}$	0.13	0.1
Volume fraction of sand, $V_s$	%	31	43
Surface conductance of sand, $\lambda_s$	S	$10^{-9}$	$10^{-9}$
Radius of sand grains, $r_s$	$\mu\text{m}$	500	500
Porosity of rock, $\varphi$	%	9	7.7
Bulk conductivity of brine, $C_w$	S/m	0.48	0.38
Relative permittivity of brine, $\epsilon_{rb}$		80	80
Diffusion coefficient of brine, $D_b$	$\text{m}^2/\text{s}$	$1.5 \times 10^{-9}$	$1.5 \times 10^{-9}$
Relative permittivity of hydrocarbon, $\epsilon_{rhy}$		3	3
Water saturation, $s_w$	%	100	46

Inversion-derived estimates obtained using different combinations of EM logs were compared to find out the best combination of EM logging tools for the desired near-wellbore characterization. Tables 4.8 and 4.9 display the  $s_w$ ,  $C_w$ ,  $\lambda_c$  and  $r_c$  estimates for the depths XX52 m and XX09 m, respectively, for the various combination of EM logs. Fig. 4.6 and 4.7 present the comparison of modeled and measured broadband permittivity and conductivity data for depths XX09 m and XX52 m, respectively. The water saturation and brine conductivity estimates are relatively similar for all the log combinations. For the depth XX52 m, the combination of induction and dielectric dispersion logs and the combination of induction, propagation and dielectric dispersion logs led to the largest data misfit. The combination of induction and dielectric dispersion logs generated 1-order of magnitude higher surface conductance and radius of clay estimates compared to those obtained from other combinations. For the depth XX09 m, water saturation estimates are slightly different for the various combinations, such that the largest difference is 0.14 saturation unit. Dielectric dispersion log interpretation generates the highest water saturation of 0.53, and the combination of LWD propagation and dielectric dispersion logging tool generates the lowest water saturation of 0.39, as listed in Table 4.9. Brine conductivity, surface conductance, and radius of clay estimates are relatively similar when using different combinations of EM logs for the depth XX09 m. Radius of pyrite estimates vary with log combinations ranging from 172  $\mu\text{m}$  to 350  $\mu\text{m}$ . The combination of induction, propagation, and dielectric dispersion logs and the combination of propagation and dielectric dispersion logs exhibit high data misfit for the second field cases. Estimates derived from only dielectric dispersion logs exhibit smallest data misfit

in both the cases; however, the application dielectric dispersion logs are suitable in low-salinity formation and in wells with low borehole rugosity. Combining various EM logs accounts for the effects due to polarization mechanisms in various frequency ranges; thereby facilitating improved water saturation estimates.

**Table 4.8 Estimated petrophysical properties and data misfit in depth XX52 m in an organic-rich formation when performing petrophysical inversion of various combinations of logging tools.**

Logging tool combination	Est. $s_w$ (fraction)	Est. $C_w$ (S/m)	Est. $\lambda_c$ (S)	Est. $r_c$ ( $\mu\text{m}$ )	Data misfit (fraction)
Induction + Propagation + Dielectric dispersion	1	0.48	$6.6 \times 10^{-8}$	0.13	0.2316
Dielectric dispersion	1	0.58	$7.2 \times 10^{-8}$	0.13	0.1272
Induction + Dielectric dispersion	1	0.35	$5.9 \times 10^{-7}$	1.31	0.2587
Propagation + Dielectric dispersion	1	0.49	$7.2 \times 10^{-8}$	0.14	0.1327

**Table 4.9 Estimated petrophysical properties and data misfit in depth XX09 m in an organic-rich formation when performing petrophysical inversion of various combinations of logging tools.**

Logging tool combination	Est. $s_w$ (fraction)	Est. $C_w$ (S/m)	Est. $\lambda_c$ (S)	Est. $r_c$ ( $\mu\text{m}$ )	Est. $r_i$ ( $\mu\text{m}$ )	Data misfit (fraction)
Induction + Propagation + Dielectric dispersion	0.46	0.38	$2.5 \times 10^{-8}$	0.1	172	0.2275
Dielectric dispersion	0.53	0.43	$2.6 \times 10^{-8}$	0.1	392	0.1367
Induction + Dielectric dispersion	0.43	0.42	$2.5 \times 10^{-8}$	0.1	194	0.1386
Propagation + Dielectric dispersion	0.39	0.54	$2.8 \times 10^{-8}$	0.1	352	0.2385



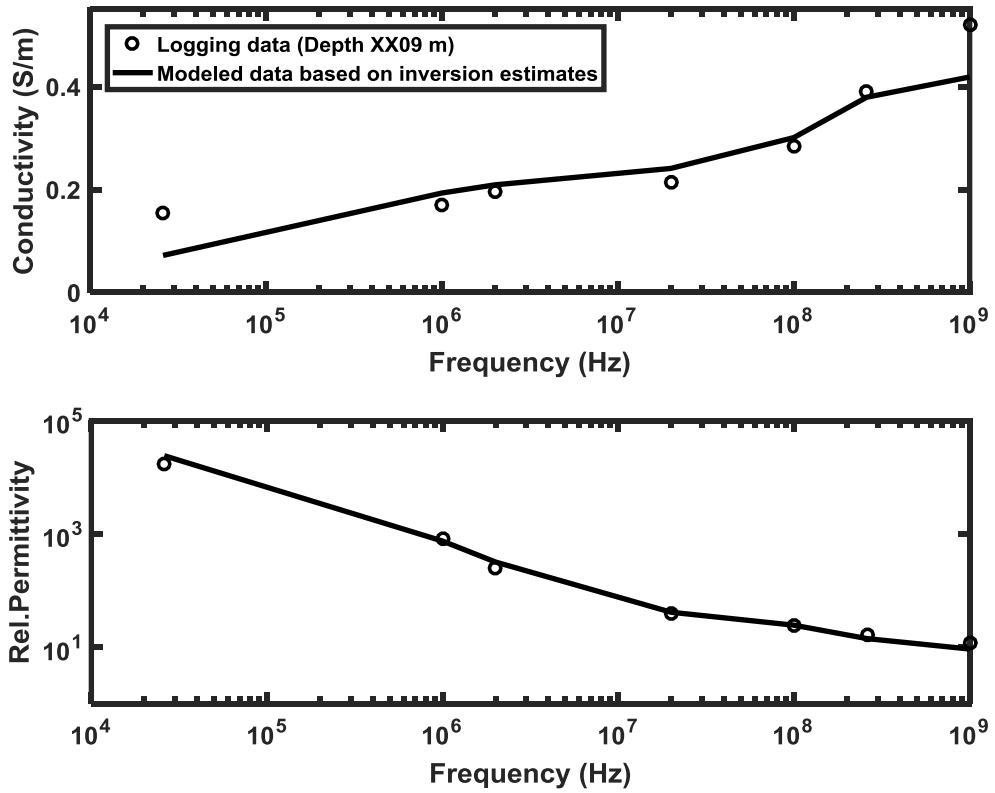


**Figure 4.6 Comparison of broadband conductivity- and permittivity-dispersion measurements against those modeled using the inversion-derived estimates for depth XX09 m in the organic-rich shale formation.**

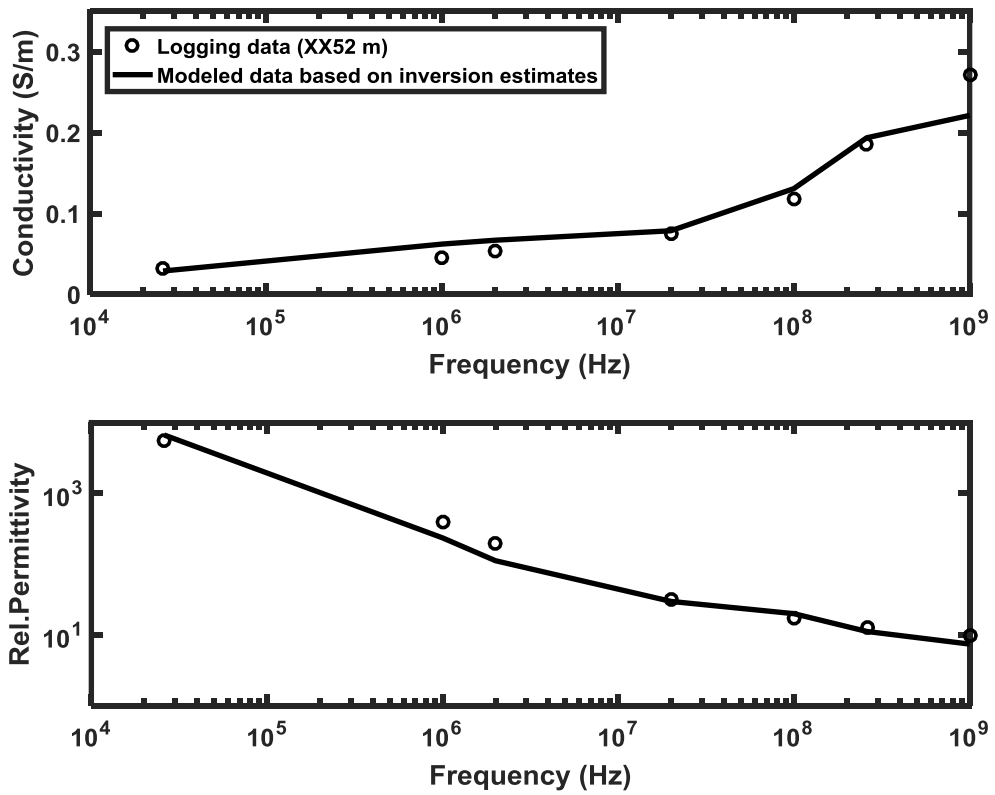


**Figure 4.7 Comparison of broadband conductivity- and permittivity-dispersion measurements against those modeled using the inversion-derived estimates for depth XX52 m in the organic-rich shale formation.**

## **Chapter 5: Dielectric Dispersion Log Interpretation in Bakken Petroleum System**

### **5.1 Inconsistent water saturation in the Bakken Petroleum System**

The Bakken formation is one of the largest contiguous deposits of oil and natural gas in the North America and is late Devonian to early Mississippian in age occupying about 200,000 square miles of the subsurface. This formation is a three-member succession that includes an upper black shale (Upper Bakken), a middle sandy siltstone (Middle Bakken), and a lower black shale (Lower Bakken). The BPS integrates the three-member succession with overlying Mississippian-aged limestone of Lodgepole formation and underlying dolostone of Three Forks formation. The BPS is a hybrid play with conventional formations, which include Scallion, Middle Bakken, Sanish and Three Forks formations, and source rock intervals, which include the Lower and Upper Bakken shales. The unconventional aspects of BPS include very low permeability conventional reservoir sections, as well as combined shale-rich source and reservoir intervals. This is contrast to most unconventional shale plays, in which a single stratigraphic interval comprises both the reservoir and source rock (Gary et al., 2015).

For improved characterization of the BPS, conventional triple combo logs and advanced downhole measurements were run in a vertical well. The advanced measurements include: (1) triaxial induction resistivity for thin-bed analysis; (2) multifrequency dielectric dispersion for water saturation estimation; (3) NMR measurements for porosity, free fluid and kerogen identification; (4) geochemical spectroscopy for mineralogy and total organic carbon (TOC); and (5) dipole sonic for

dynamic rock properties estimation. The water-filled porosity was measured on cores by Dean-Stark analysis.

Gary et al. (2015) reported that water saturation estimates obtained from triaxial resistivity induction log, NMR log, dielectric dispersion log, Techlog Quanti-ELAN, and Dean-Stark core measurements are not consistent and can vary up to 0.6 water saturation units. In this chapter, we develop a global search inversion algorithm coupled with three geoelectromagnetic mixing models to interpret the dielectric dispersion logs at four frequencies acquired across the BPS to estimate water saturation, water salinity of the formation, homogeneity index, and cementation index in the BPS. Unlike service company's dielectric inversion results, water saturation estimates obtained using the proposed interpretation method are not an exact value but a range of possible values within a desired accuracy. These estimates were compared against those obtained from induction resistivity log, NMR log, Quanti-ELAN solver, service company's dielectric inversion, and Dean-Stark core measurements.

## **5.2 Dielectric dispersion log interpretation models**

Mixing models are used to process the effective conductivity and permittivity data obtained using subsurface logs for purposes of water saturation estimation. The frequency-invariant complex-refractive index method (CRIM) is widely used to interpret the effective conductivity and permittivity of homogeneous materials at frequency close to 1 GHz. Experimental investigations have shown that the effective permittivity and conductivity of fluid-filled granular materials can be modeled using the frequency-invariant Lichtenecker-Rother's model (LR model), which is expressed as

$$(\varepsilon^*)^\alpha = (1 - \Phi)\varepsilon_m^\alpha + S_w \Phi \varepsilon_w^*{}^\alpha + (1 - S_w)\Phi \varepsilon_o^\alpha \dots\dots\dots(5.1)$$

where the complex quantity is identified by \* superscript,  $\varepsilon^*$  is the complex permittivity of a geomaterial or formation,  $\varepsilon_m$  is the matrix permittivity,  $\varepsilon_w^*$  is the complex permittivity of pore-filling water,  $\varepsilon_o$  is the pore-filling hydrocarbon permittivity,  $\Phi$  is the total porosity of the geomaterials,  $S_w$  is water saturation, and  $\alpha$  is the geometrical arrangement factor ranging from -1 to 1. In this chapter, the parameter  $\alpha$  is used as the homogeneity index, such that  $\alpha = 1/2$  indicates a non-layered homogeneous medium,  $\alpha = 1$  indicates a layered medium with layers parallel to the propagating electric field, and  $\alpha = -1$  indicates a layered medium with layers perpendicular to the propagating electric field. Notably,  $\alpha = 1/2$  transforms the LR model to CRI model. In order to respect the complexity of the formations in BPS, we implement LR model instead of CRI model.

Application of LR model to interpret the 1-GHz permittivity and conductivity logs generates inaccurate water saturation because the parameter estimation is unconstrained with two log inputs due to the lack of information on the formation water conductivity (salinity), permittivity of the formation water, rock matrix, and hydrocarbon, and the parameter  $\alpha$ . We couple LR model with two dielectric dispersion models, namely SMD model and PS model, which can be applied at four dielectric-dispersion log-acquisition frequencies. The resulting integrated model generates more accurate water saturation estimates because the parameter estimation is now constrained with eight log inputs. The SMD model was developed for clean brine-saturated rocks and is expressed as

$$\varepsilon^* = (\Phi_w)^m + [1 - \Phi_w^m]\varepsilon_m - \varepsilon_m \Gamma\left(\Phi_w, m, \frac{\varepsilon_w^*}{\varepsilon_m}\right) \dots\dots\dots(5.2)$$

where  $\Phi_w$  is water-filled porosity, such that  $\Phi_w = S_w\Phi$ , and  $m$  is the rock textural parameter that indicates cementation/tortuosity describing the rock geometry (Han et al., 2012). In this chapter, we estimate  $m$  as a cementation index. However, SMD model is not applicable for clay- and pyrite-rich formation. The LR, CRIM, and SMD models neglect the interfacial polarization (IP) effects of clays and conductive minerals; thereby generating inaccurate estimation of water saturation and TOC in clay- and conductive-mineral-rich mudrock formations (Misra and Han, 2016a; Misra and Han, 2016b). Misra et al. (2016a) derived a mechanistic electrochemical model, referred as PS model, to evaluate the dependence of effective complex conductivity of geological mixtures on the electrical properties of the host and inclusion materials, size and shape of inclusions, and the measurement frequency. PS model is coupled in the proposed integrated model to accurately quantify the dielectric dispersion response of formations rich in clay and pyrite. Table 5.2 lists the petrophysical parameters in the PS model. Misra et al. (2016c) used the PS model to interpret multifrequency induction log measurements.

### 5.3 Modified Levenberg-Marquardt inversion algorithm

The nonlinear inverse problem discussed in this section involves estimation of petrophysical parameters that generate least misfit between the measured dielectric dispersion logs and integrated model predictions of multi-frequency effective permittivity and conductivity. In the proposed inversion scheme, the measured data vectors  $\mathbf{Perm}^{\text{meas}}$  and  $\mathbf{Cond}^{\text{meas}}$  containing 4 elements each representing the log-derived effective multifrequency permittivity and conductivity values of formation obtained at the 4 distinct dielectric-dispersion log-acquisition angular frequencies, namely,  $\omega_1$ ,  $\omega_2$ ,

$\omega_3$ , and  $\omega_4$ . The goal is to estimate petrophysical parameter vector  $\mathbf{m}^{\text{PROP}}$  comprising water saturation ( $S_w$ ), formation water conductivity ( $C_w$ ), homogeneity index ( $m$ ), and cementation index ( $\alpha$ ) of a specific depth in the BPS. To that end, the integrated dielectric-dispersion interpretation model, which combines LR, SMD and PS models, is used to generate the modeled data vectors  $\mathbf{Perm}^{\text{mod}}(\mathbf{m})$  and  $\mathbf{Cond}^{\text{mod}}(\mathbf{m})$  comprising model predictions at the 4 distinct dielectric-dispersion log acquisition frequencies for a specific model parameter vector  $\mathbf{m}$  made of estimates for the four unknown model parameters, namely  $S_w$ ,  $C_w$ ,  $m$ , and  $\alpha$ . The measured and modeled data vectors can be expressed as

$$\mathbf{Perm}^{\text{mod/meas}}(\mathbf{m}) = [Perm(\mathbf{m}, \omega_1), Perm(\mathbf{m}, \omega_2), \dots Perm(\mathbf{m}, \omega_4)] \dots \dots \dots (5.3)$$

and

$$\mathbf{Cond}^{\text{mod/meas}}(\mathbf{m}) = [Cond(\mathbf{m}, \omega_1), Cond(\mathbf{m}, \omega_2), \dots Cond(\mathbf{m}, \omega_4)] \dots \dots \dots (5.4)$$

The measured data vectors  $\mathbf{Perm}^{\text{meas}}$  and  $\mathbf{Cond}^{\text{meas}}$  are matched with modeled data vectors  $\mathbf{Perm}^{\text{mod}}(\mathbf{m})$  and  $\mathbf{Cond}^{\text{mod}}(\mathbf{m})$  by varying the estimated model parameter vector  $\mathbf{m}^{\text{est}}$ . The vector  $\mathbf{m}^{\text{est}}$  that generates best fit between the data and prediction represents the characteristic petrophysical properties of a specific depth in the BPS. To that end, the inversion algorithm iteratively computes the vector  $\mathbf{m}^{\text{est}}$  to find the best match. The inversion scheme requires minimizing the quadratic cost function  $C(\mathbf{m})$  at each iteration defined as

$$C(\mathbf{m}) = \|\mathbf{Perm}^{\text{mod}}(\mathbf{m}^{\text{est}}) - \mathbf{Perm}^{\text{meas}}\|_2^2 + \|\mathbf{Cond}^{\text{mod}}(\mathbf{m}^{\text{est}}) - \mathbf{Cond}^{\text{meas}}\|_2^2 \dots \dots \dots (5.5)$$

For purposes of minimization, we defined a cost function vector  $\mathbf{F}(\mathbf{m})$  of 4 elements. Individual components of the vector  $\mathbf{F}(\mathbf{m})$  are referred as  $f_i(\mathbf{m}^k)$ , where

superscript  $k$  is the iteration counter for the inversion scheme,  $\mathbf{m}^k$  is the model parameter vector computed at the  $k$ -th iteration of the inversion, and subscript  $i$  denotes one of the 4 log- acquisition frequencies.  $\mathbf{F}(\mathbf{m}^k)$  is thus expressed as

$$\mathbf{F}(\mathbf{m}^k) = [f_1(\mathbf{m}^k), f_2(\mathbf{m}^k), \dots, f_4(\mathbf{m}^k)]^T \dots\dots\dots(5.6)$$

where  $f_i(\mathbf{m}^k)$  is expressed as

$$f_i(\mathbf{m}^k) = [\mathbf{Perm}^{\text{mod}}(\mathbf{m}^k) - \mathbf{Perm}^{\text{meas}}]_i^2 + [\mathbf{Cond}^{\text{mod}}(\mathbf{m}^k) - \mathbf{Cond}^{\text{meas}}]_i^2 \dots\dots\dots(5.7)$$

where  $i = 1, 2, 3,$  and  $4$ .

We modified the Levenberg-Marquardt algorithm (LMA), for purposes of nonlinear inversion (Aster et al., 2013; Misra and Han, 2016a), by introducing scaling matrix  $\mathbf{W}_s$  into the mathematical formulation of the LMA inversion scheme and  $\mathbf{W}_s$  is a  $4 \times 4$  diagonal matrix. The modified LMA doesn't implement a reference vector  $\mathbf{m}_R$ , which mitigates the non-uniqueness of the inverse problem but constrains the solution space around  $\mathbf{m}$ . The modified inversion scheme is expressed as

$$[(\mathbf{J}(\mathbf{m}^k)\mathbf{W}_s)^T \cdot (\mathbf{J}(\mathbf{m}^k)\mathbf{W}_s) + \lambda\mathbf{I} + \alpha^2\mathbf{I}] \cdot \mathbf{W}_s^{-1} \cdot \Delta\mathbf{m}^k = -(\mathbf{J}(\mathbf{m}^k)\mathbf{W}_s)^T \cdot \mathbf{F}(\mathbf{m}^k) - \alpha^2\mathbf{I} \cdot \mathbf{W}_s^{-1} \cdot \mathbf{m}^k \dots\dots\dots(5.8)$$

where  $\mathbf{m}^k$  is the interpretation model parameter vector computed at the  $k$ -th iteration of the inversion,  $\mathbf{F}(\mathbf{m}^k)$  is the cost function vector,  $\mathbf{J}(\mathbf{m}^k)$  is the Jacobian matrix of  $\mathbf{F}(\mathbf{m}^k)$ ,  $\Delta\mathbf{m}^k$  is the correction vector generated at the  $k$ -th iteration that determines the direction towards the convergence of the interpretation model parameter estimation process,  $\lambda$  is the damping parameter,  $\alpha$  is the regularization parameter,  $\mathbf{I}$  is an identity matrix, and T is matrix transpose operator. The Jacobian matrix  $\mathbf{J}(\mathbf{m}^k)$  is formulated in the same form as it in Chapter 3. And the way to define the bounds of integrated dielectric-dispersion



interpretation model parameters and the jump-back-in step are similar to those in Chapter

3.  $\mathbf{W}_s$  is expressed as

$$\mathbf{W}_s = \begin{pmatrix} 10^{\alpha_1} & \dots & 0 \\ \vdots & \ddots & \vdots \\ 0 & \dots & 10^{\alpha_4} \end{pmatrix} \dots\dots\dots(5.9)$$

where the parameters  $(\alpha_1, \dots, \alpha_4)$  in the diagonal scaling matrix denote the order of magnitude difference between the estimates of the 4 unknown model parameters. The parameters  $\alpha_1, \alpha_2, \alpha_3,$  and  $\alpha_4$  correspond to the water saturation, formation water conductivity, homogeneity index, and cementation index, respectively, and their values are assumed to be 0, 2, 0, and 1, respectively.

Schmitt et al. (2011) reported that the dielectric measurements at 1GHz, which can be modeled using CRI model, lose sensitivity to water salinity for salinity above 60 kppm. Donadille et al. (2016) reported that dielectric dispersion models such as SMD and bimodal lose their sensitivity at even lower water salinity compared with CRI model. All these models exhibit negligible sensitivity for porosity lower than 0.05 p.u. This loss of sensitivity of the forward models to water-filled porosity and salinity breaks down LMA-based inversion schemes. However, the newly developed inversion algorithm proposed in this paper introduces a scaling matrix  $\mathbf{W}_s$  to improve the inversion capabilities for high salinity and low porosity scenarios. For instance, in the synthetic case presented below in this paper, the inversion-derived estimates are unique, accurate, and converge despite the large formation water conductivity of 50 S/m (>300 kppm) for wide range of initial guesses. This is possible due to the implementation of the scaling matrix.

Data misfit is the difference between the modeled data based on the inversion-derived estimates and the measured dielectric-dispersion log data. The data misfit is expressed as a relative error defined as

$$Rel. Err = \left[ \frac{1}{4} \sum_{i=1}^4 \left( \frac{Perm^{mod} - Perm^{meas}}{Perm^{meas}} \right)_i^2 + \left( \frac{Cond^{mod} - Cond^{meas}}{Cond^{meas}} \right)_i^2 \right]^{0.5} \dots\dots\dots(5.10)$$

**5.4 Synthetic case study**

*Synthetic Case 1:*

The inversion scheme was tested on synthetic effective permittivity and conductivity data containing 5% Gaussian noise generated using the integrated dielectric dispersion interpretation model at four dielectric log-acquisition frequencies, namely 22 MHz, 100 MHz, 350 MHz, and 960 MHz. The integrated dielectric dispersion interpretation model combines SMD model, applied at 22 MHz, 100 MHz, and 350 MHz, with LR model, applied only at 960 MHz. Table 5.1 mentions the properties of Synthetic Formation 1 used for generating the synthetic permittivity and conductivity data. The Synthetic Formation 1 identifies a clay-lean, oil-bearing formation. There is no pyrite in the Synthetic Formation 1 and 5% Gaussian noise is added to the synthetic data. The water salinity in the Synthetic Formation is very high (250 kppm), mimicking the high salinity Bakken formation. Inversion-derived estimates of the four unknown integrated model parameters are  $s_w = 0.51$ ,  $C_w = 40.8$  S/m,  $\alpha = 0.605$ , and  $m = 1.715$ , which are close to the original parameter values, listed in Table 5.1, assumed for the Synthetic Formation 1. The inversion-derived estimates and data misfit at each iteration is illustrated in Fig. 5.1. The integrated model prediction based

on our estimates of the four parameters match the synthetic effective permittivity and conductivity with relative error close to  $2 \times 10^{-2}$ .

**Table 5.1 Assumed physical properties of the Synthetic Formation 1. Inversion was performed to estimate the parameters highlighted in grey.**

Parameters	Values
Volume fraction of clay	12 %
Volume fraction of sand	82 %
Porosity of rock	6 %
Bulk conductivity of brine ( $C_w$ )	40 S/m
Water saturation ( $s_w$ )	50 %
Homogeneity index ( $\alpha$ )	0.62
Cementation index ( $m$ )	1.7

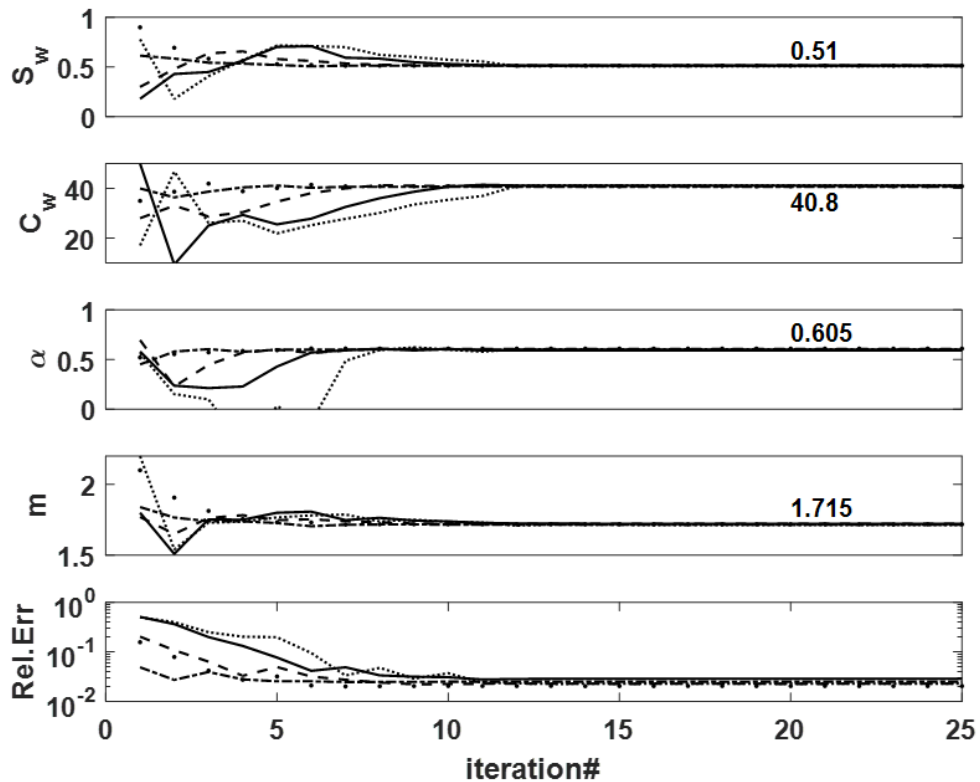


**Figure 5.1 Convergence of inversion-derived estimates of unknown integrated model parameters and relative error as a function of iteration for the inversion of synthetic data with 5% Gaussian noise generated for the Synthetic Formation 1 using the integrated model.**

*Synthetic Case 2:*

The inversion scheme was tested on synthetic effective permittivity and conductivity data containing 5% Gaussian noise generated using the integrated dielectric dispersion interpretation model at four dielectric log-acquisition frequencies, namely 22 MHz, 100 MHz, 350 MHz, and 960 MHz. The integrated dielectric dispersion interpretation model combines PS and SMD model, applied at 22 MHz, 100 MHz, and 350 MHz, with LR model, applied only at 960 MHz. Table 5.2 mentions the properties of Synthetic Formation 2 used for generating the synthetic permittivity and conductivity data. The Synthetic Formation 2 identifies a kaolinite-type nonconductive clay-rich, brine-bearing formation. There is no pyrite in the Synthetic Formation 2 and 5% Gaussian noise is added to the synthetic data. The water salinity in the Synthetic Formation 2 is very high (320 kppm), mimicking the high salinity Bakken formation. Inversion-derived estimates of the four unknown integrated model parameters are  $s_w = 0.845$ ,  $C_w = 50.6$  S/m,  $\alpha = 0.593$ , and  $m = 1.839$ , which are close to the original parameter values, listed in Table 5.2, assumed for the Synthetic Formation 2. The inversion-derived estimates and data misfit at each iteration is illustrated in Fig. 5.2. The integrated model prediction based on our estimates of the four parameters match the synthetic effective permittivity and conductivity with relative error close to  $10^{-2}$ .

**Table 5.2 Assumed physical properties of the Synthetic Formation 2. Inversion was performed to estimate the parameters highlighted in grey.**

Parameters	Values
Volume fraction of clay	43 %
Relative permittivity of clay	5
Surface conductance of clay ( $\lambda_c$ )	$10^{-6}$ S
Radius of spherical clay grains ( $r_c$ )	1 $\mu\text{m}$
Volume fraction of sand	50 %
Surface conductance of sand	$10^{-9}$ S
Radius of sand grains	500 $\mu\text{m}$
Porosity of rock	7 %
Bulk conductivity of brine ( $C_w$ )	50 S/m
Relative permittivity of brine	80
Diffusion coefficient of brine	$10^{-9}$ m <sup>2</sup> /s
Relative permittivity of hydrocarbon	3
Water saturation ( $s_w$ )	85 %
Homogeneity index ( $\alpha$ )	0.6
Cementation index ( $m$ )	1.82

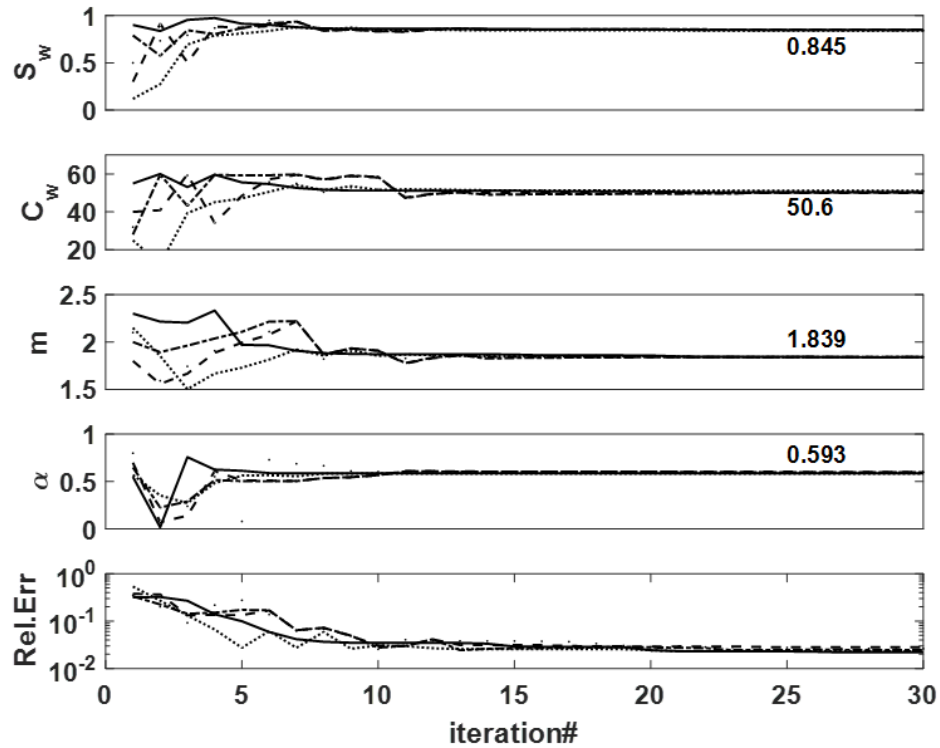


**Figure 5.2 Convergence of inversion-derived estimates of unknown integrated model parameters and relative error as a function of iteration for the inversion of synthetic data with 5% Gaussian noise generated for the Synthetic Formation 2 using the integrated model.**

## 5.5 Application in Bakken Petroleum System

### *Field Case:*

For a clay-lean zone, for e.g. Middle Bakken, the integrated model combines the SMD model, applied at 22 MHz, 100 MHz, and 350 MHz, with the LR model, applied only at 960 MHz. This integrated model inverts the dielectric dispersion log acquired in the Middle Bakken and other similar clay-lean formations. On the other hand, for a clay-rich zone, for e.g. Upper and Lower Bakken formations and parts of Three Forks, the integrated model combines the PS and SMD model, applied at 22 MHz, 100 MHz, and 350 MHz, with the LR model, applied only at 960 MHz. Inversion of multi-frequency dielectric logs was performed to estimate water saturation, formation water conductivity, homogeneity index, and cementation index across 400-foot depth interval in BPS.

For the inversion of synthetic effective permittivity and conductivity data containing 5% Gaussian noise, a regularization parameter is introduced in the mathematical formulation of the modified-LMA scheme to mitigate the non-uniqueness of the problem. However, for the inversion of real subsurface effective permittivity and conductivity data, the non-uniqueness issues could not be solved by introducing a regularization parameter. To that end, global search algorithm was implemented around the modified LMA-based inversion, as described in Fig. 5.3. First of all, 250 initial guesses of the petrophysical parameters are randomly generated in the predefined search space spanning three orders of magnitude. Then the modified-LMA inversion generates the estimates parameters for each of these initial guesses. Following that, a line search method is applied to find the smallest error in the search space. Finally, the inverted

petrophysical parameters corresponding to the smallest error are selected as the estimated values of integrated model parameters,  $S_w$ ,  $C_w$ ,  $m$ , and  $\alpha$ .

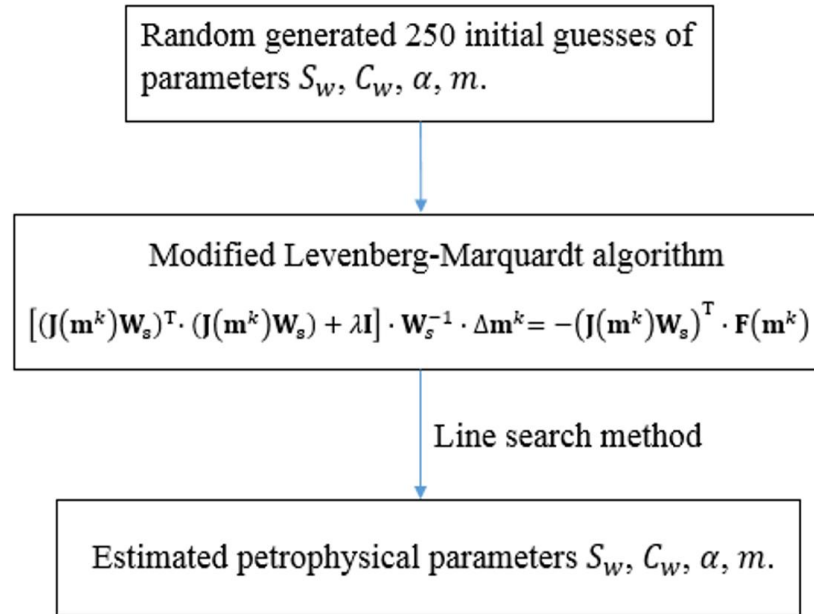


**Figure 5.3 Global-search modified-LMA inversion.**

The field data inversion results are not converged for 250 initial guesses and generates different petrophysical parameter estimation for similar level of accuracy (error). The global minimum among the 250 estimates parameters can be biased to represent the petrophysical properties of the formation because of the noise in the data. So the petrophysical parameters such as water saturation estimates for a specific depth obtained using the proposed interpretation method is not one single value but a range of possible values within a desired accuracy. Fig. 5.4 illustrates the flow chart of the proposed dielectric-dispersion log interpretation method. The first three steps are the same as the aforementioned global search inversion method. Then a range of possible petrophysical parameters values within a desired accuracy which is user defined is determined. In this chapter, we define the desired accuracy to 10% of the global minimum

error. The inverted petrophysical parameters corresponding to the error within the desired accuracy are recorded and the minimum and maximum values of each recorded petrophysical parameter can be decided. Then the range of possible petrophysical parameters values can be generated.

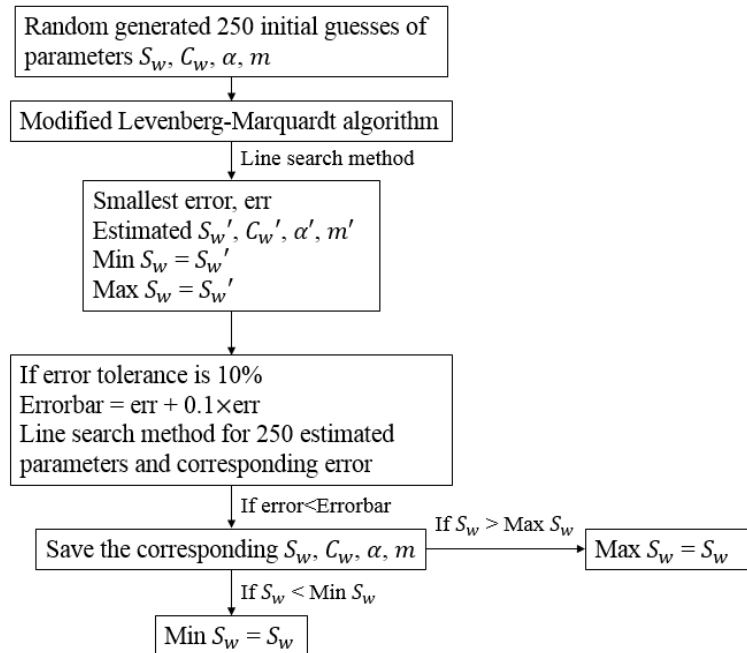


**Figure 5.4 Flow chart of the proposed dielectric-dispersion log interpretation method.**

Three Forks formation has dolostone with laminations of dolo-siltite and interbedded with clay-rich, conglomeratic dolo-mudstone (Gary et al, 2015). Fig. 5.5 presents the inversion result for the depth XX864 ft in the Three Forks formation that is clay lean. Measured data is presented as discrete points and model predictions are present as continuous curves. The measured effective permittivity and conductivity data is matched with the integrated model (SMD+LR) predictions, which provide better data fit compared to SMD+CRI model predictions. Integration of LR model performs



comparatively better than the integration of CRI model because LR model does not assume homogeneity of the formation under investigation. Moreover, inversion with LR model generates the homogeneity index  $\alpha$  providing an improved log-base characterization.

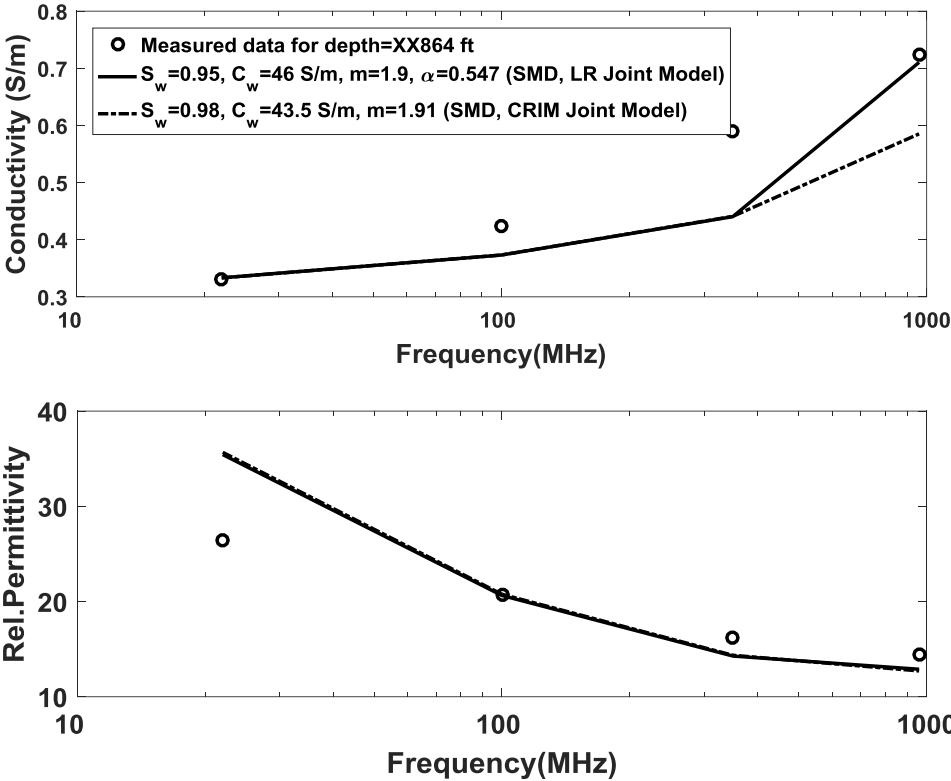


**Figure 5.5 Comparison of effective conductivity and permittivity measurements and model predictions for depth XX864 ft in Three Forks formation.**

The Middle Bakken formation is the most internally complex of the BPS and is primarily bioturbated, silt-dominated, shallow-marine deposits (Gary et al., 2015). Global search inversion is performed along the Middle Bakken. The efficiency of the inversion results is presented for the depth XX736 ft in the Middle Bakken formation that is clay lean. Fig. 5.6, 5.7, 5.8, and 5.9 are 3D error plots showing the inversion-derived water saturation, formation water conductivity, cementation index, and homogeneity index, respectively, for 250 randomly generated sets of initial guesses of

the integrated model parameters during the global search inversion. These figures demonstrate that, unlike service company's dielectric inversion results, water saturation estimates obtained using the proposed interpretation method are not an exact value but a range of possible values within a desired accuracy in a user-specified search space. The estimated cementation index and homogeneity index are more converged for 250 initial guesses compared with estimated water saturation and water conductivity. Fig. 5.10 compares effective conductivity and permittivity log measurements with the integrated model predictions based on the inversion-derived estimates that generates the minimum data misfit within the search space. The estimated ranges of possible petrophysical parameters values within a desired accuracy (10%) are:  $S_w$  is between 0.935 to 0.997,  $C_w$  is between 30.63 S/m to 35.4 S/m,  $m$  is between 1.98 to 2, and  $\alpha$  is between 0.46 to 0.471.

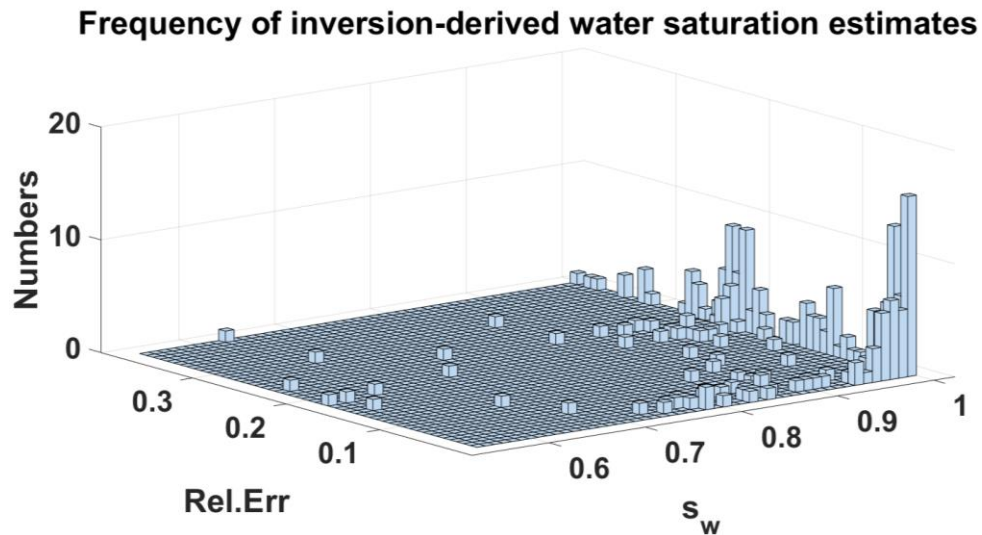


**Figure 5.6** Frequency of inversion-derived  $S_w$  estimates for depth XX736 ft along with data misfit for 250 randomly generated sets of initial guesses of integrated model parameters.

### Frequency of inversion-derived water conductivity estimates

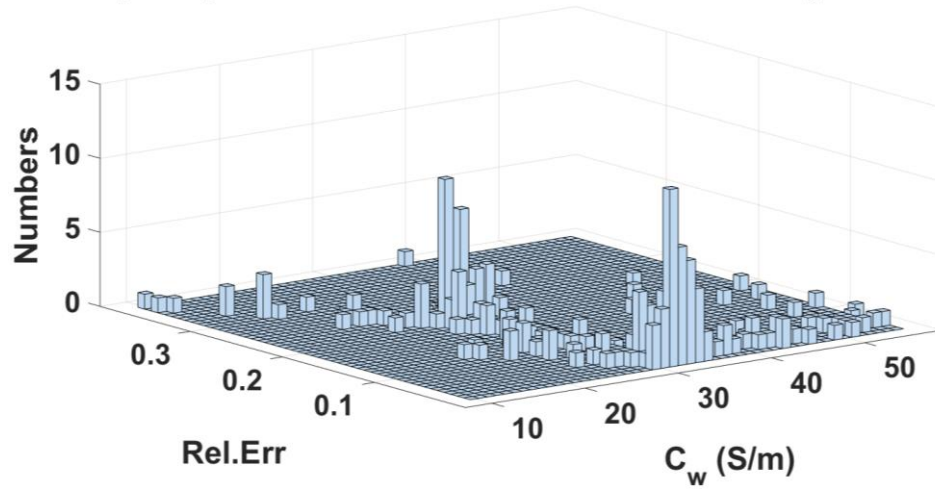


Figure 5.7 Frequency of inversion-derived  $C_w$  estimates for depth XX736 ft along with data misfit for 250 randomly generated sets of initial guesses of integrated model parameters.

### Frequency of inversion-derived cementation index estimates

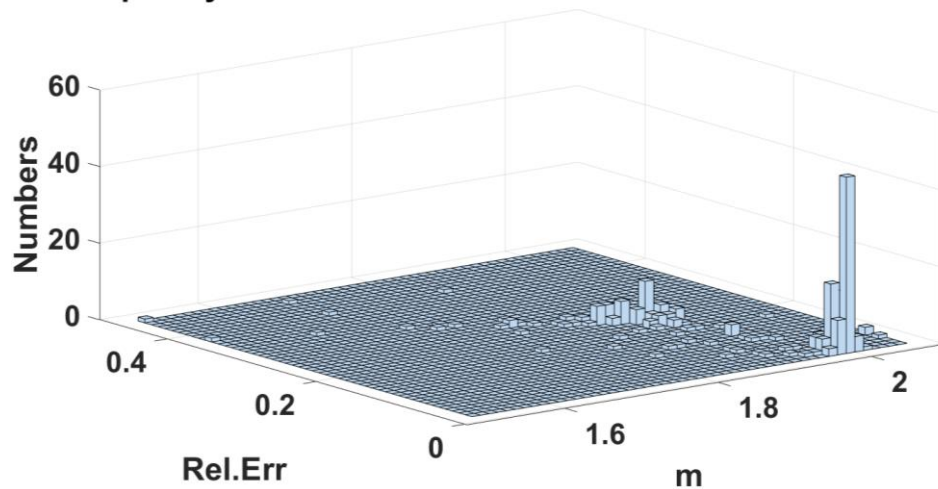
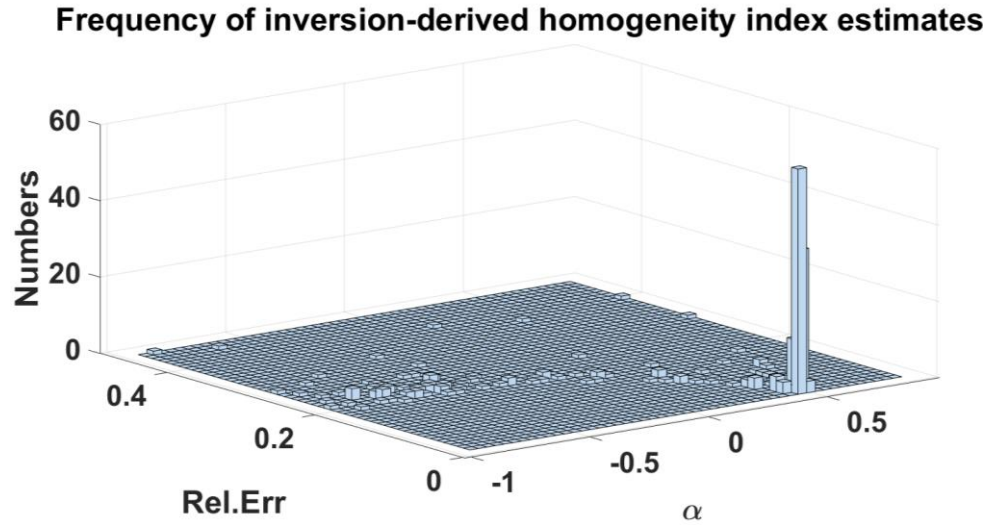
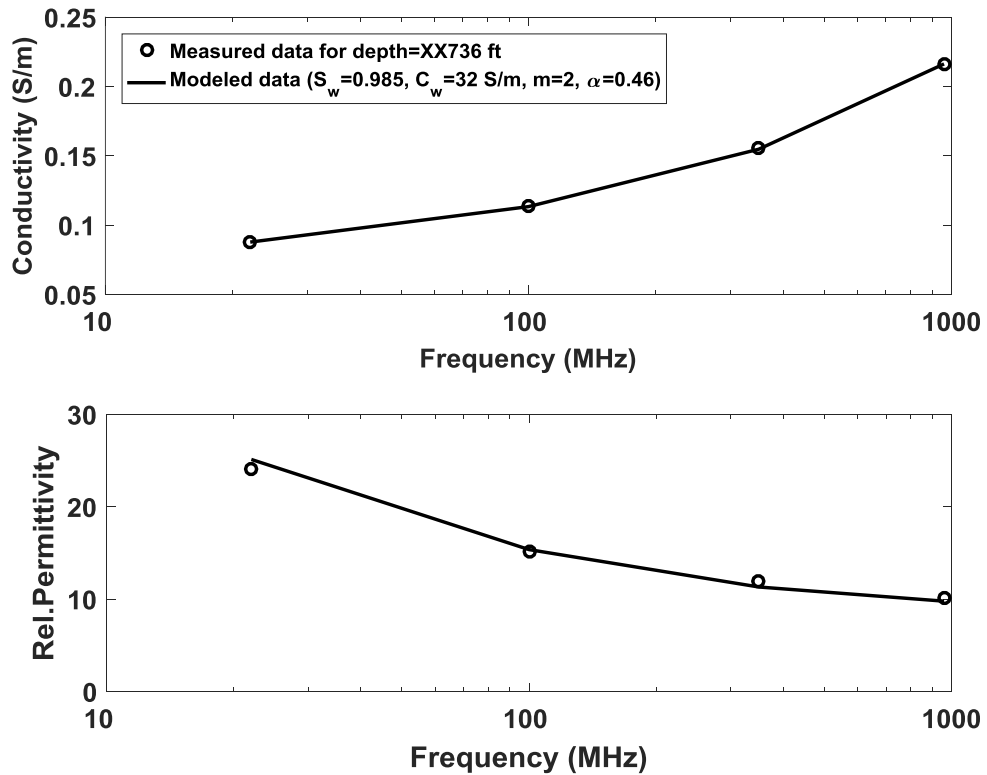


Figure 5.8 Frequency of inversion-derived  $m$  estimates for depth XX736 ft along with data misfit for 250 randomly generated sets of initial guesses of integrated model parameters.



**Figure 5.9** Frequency of inversion-derived  $\alpha$  estimates for depth XX736 ft along with data misfit for 250 randomly generated sets of initial guesses of integrated model parameters.



**Figure 5.10** Comparison of effective conductivity and permittivity measurements and model predictions for depth XX736 ft in the Middle Bakken formation.

The previous two cases were from clay-lean depths, where the global-search inversion scheme is coupled to integrated model that combines SMD and LR models. However, for the clay- and pyrite-rich units, SMD and LR model cannot account for the IP effects of pyrite and clay; thereby, generating inaccurate water saturation estimates. In such cases, we implement the global search inversion algorithm coupled with integrated model that combines PS, SMD and LR models. Efficiency of the inversion results is shown for the depth XX874 ft in the Three Forks formation that is rich in clay and pyrite. Fig. 5.11 compares the effective conductivity and permittivity log measurements against the SMD+LR integrated model predictions and PS+SMD+LR integrated model predictions computed based on the inversion-derived estimates of the model parameters that result in minimum data misfit. For this case, the PS+SMD+LR integrated model is physically consistent; therefore the predictions of PS+SMD+LR integrated model have better data fit as compared to those of SMD+LR integrated model, as shown in Fig 5.11. The water saturation estimate obtained using the SMD+LR integrated model is 100%, whereas that obtained using the PS+SMD+LR model is 82% (80.8% - 85%).

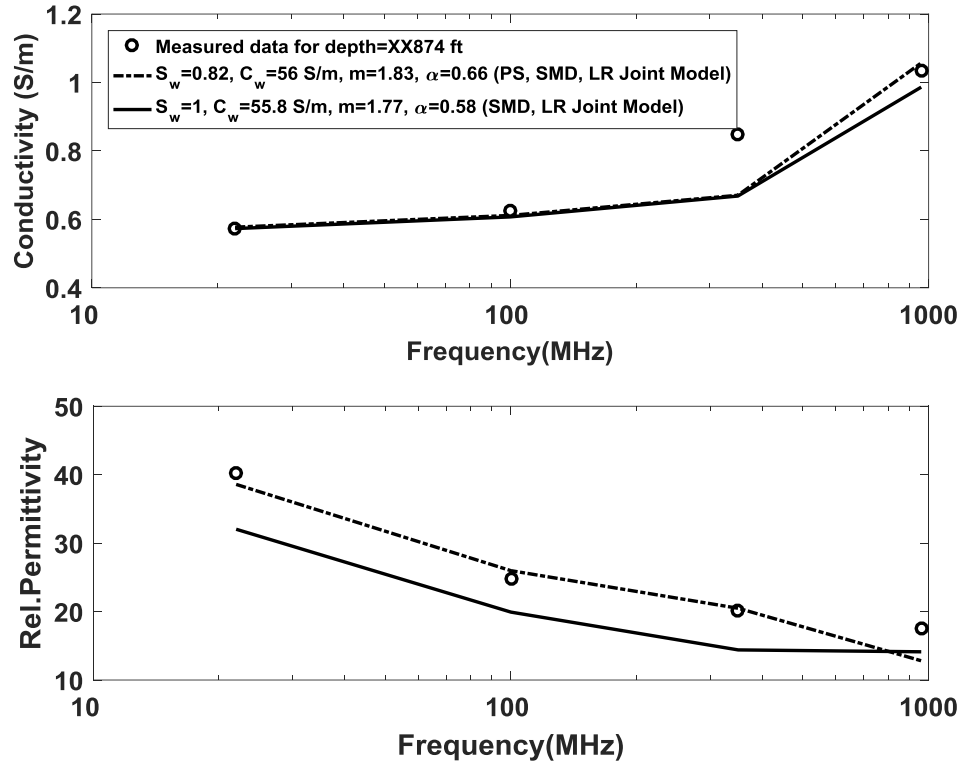


**Figure 5.11 Comparison of effective conductivity and permittivity measurements and model predictions for depth XX874 ft in the Three Forks formation.**

The parameters in PS model are listed in Table 5.2 and some petrophysical parameters are unknown such as radius of spherical clay grains and surface conductance of clay. Since there are only four sets of dielectric data including conductivity and permittivity, the values of radius of spherical clay grains and surface conductance of clay can't be estimated by inversion or will increase the non-uniqueness and uncertainty of the problem. We fixed the values of radius of spherical clay grains,  $r_c$ , and surface conductance of clay,  $\lambda_c$ , ( $\lambda_c = 1 \times 10^{-6} \text{ S}$ ,  $r_c = 1 \mu\text{m}$ ). We found that the inverted petrophysical parameters such as water saturation are not sensitive to the values of radius of spherical clay grains and surface conductance of clay. Table 5.3 illustrates the inversion results of Synthetic Case 2 without 5% Gaussian noise by using different

values of radius of spherical clay grains and surface conductance of clay. The results prove that the estimated petrophysical parameters are close to the formation true petrophysical parameters values for radius of spherical clay grains and surface conductance of clay different from the true radius of spherical clay grains and surface conductance of clay in the Synthetic Formation 2.

**Table 5.3 Inversion results of Synthetic Case 2 without 5% Gaussian noise by using different values of radius of spherical clay grains and surface conductance of clay.**

Clay properties	$S_w$	$C_w$	$\alpha$	$m$
$\lambda_c = 1 \times 10^{-6} \text{ S}, r_c = 1 \text{ } \mu\text{m}$	0.85	50	0.6	1.82
$\lambda_c = 5 \times 10^{-7} \text{ S}, r_c = 2 \text{ } \mu\text{m}$	0.84	53.2	0.594	1.813
$\lambda_c = 5 \times 10^{-7} \text{ S}, r_c = 0.5 \text{ } \mu\text{m}$	0.853	49.6	0.6	1.82
$\lambda_c = 1 \times 10^{-7} \text{ S}, r_c = 0.2 \text{ } \mu\text{m}$	0.841	52.2	0.595	1.813
$\lambda_c = 1 \times 10^{-7} \text{ S}, r_c = 0.1 \text{ } \mu\text{m}$	0.876	46.7	0.604	1.81
$\lambda_c = 5 \times 10^{-6} \text{ S}, r_c = 5 \text{ } \mu\text{m}$	0.847	50.4	0.6	1.821
$\lambda_c = 1 \times 10^{-5} \text{ S}, r_c = 10 \text{ } \mu\text{m}$	0.847	50.5	0.6	1.82

We used this dielectric-dispersion log interpretation method to process multifrequency dielectric data in totally 55 depth of the science well intersecting BPS. Fig. 5.18 shows the range of these petrophysical parameters within a desired accuracy (10%). In some depths such as XX630.5 ft, the estimated water saturation and water conductivity show wide range within a desired accuracy while in other depths such as XX677 ft these petrophysical parameters are converged for 250 initial guesses. Fig. 5.12, 5.13 and 5.14, 5.15 are 3D error plots showing the inversion-derived water saturation, formation water conductivity of depth XX677 ft and XX630.5 ft, respectively, for 250 randomly generated sets of initial guesses of the integrated model

parameters during the global search inversion. In Lodgepole which is a limestone formation and has low porosity (around 3%) and small pore size, the range of water saturation and water conductivity is wide within a desired accuracy. And in upper part of Middle Bakken which exhibits relatively lower formation water conductivity compared with other formations and wide range of pore size distribution, the range of water saturation and water conductivity is also wide.

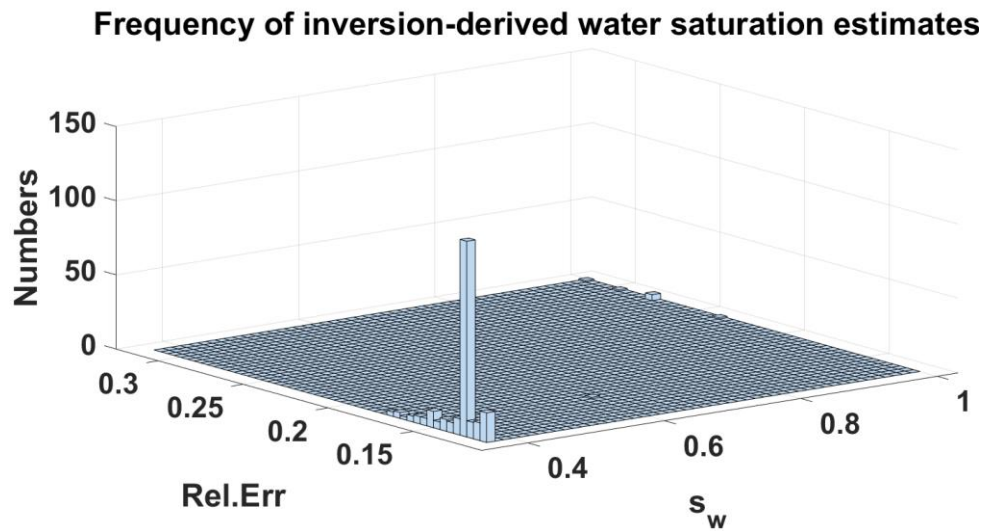


**Figure 5.12** Frequency of inversion-derived  $S_w$  estimates for depth XX677 ft along with data misfit for 250 randomly generated sets of initial guesses of integrated model parameters.



### Frequency of inversion-derived water conductivity estimates

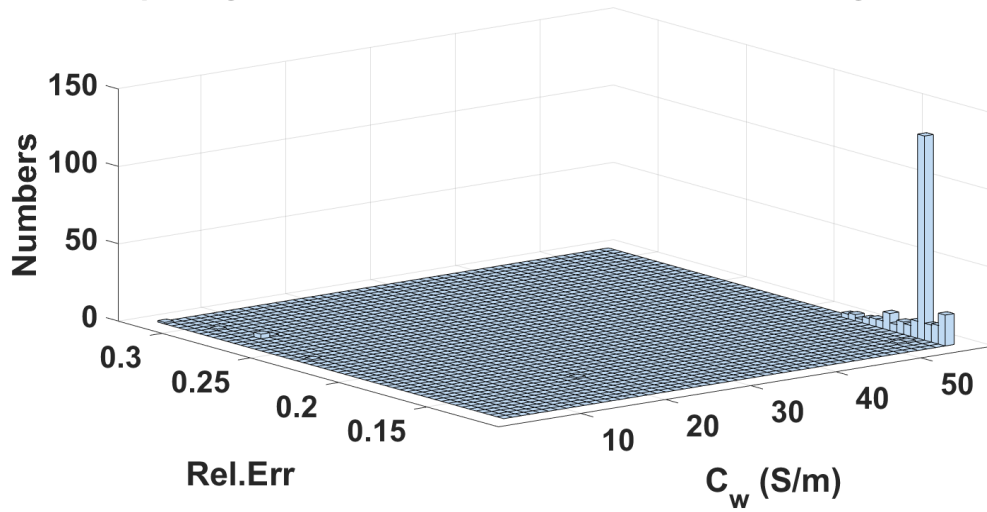


Figure 5.13 Frequency of inversion-derived  $C_w$  estimates for depth XX677 ft along with data misfit for 250 randomly generated sets of initial guesses of integrated model parameters.

### Frequency of inversion-derived water saturation estimates

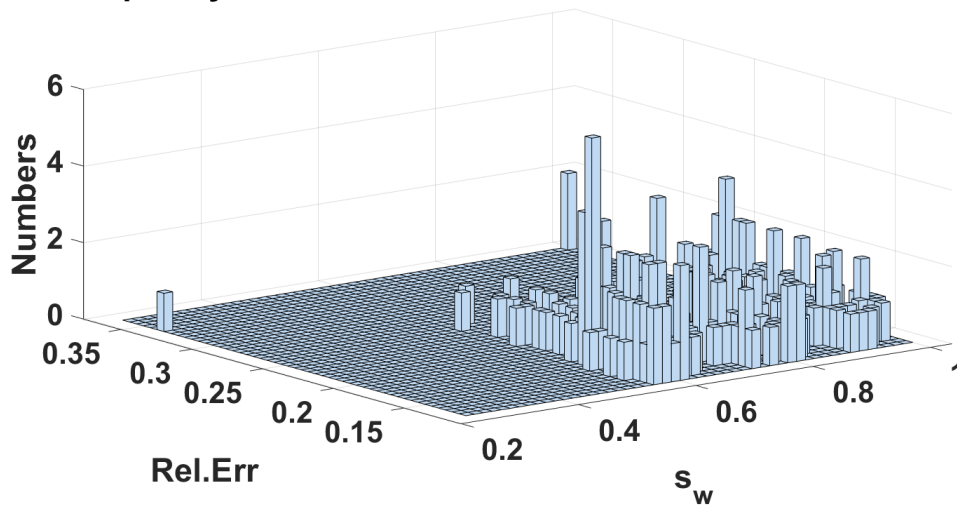
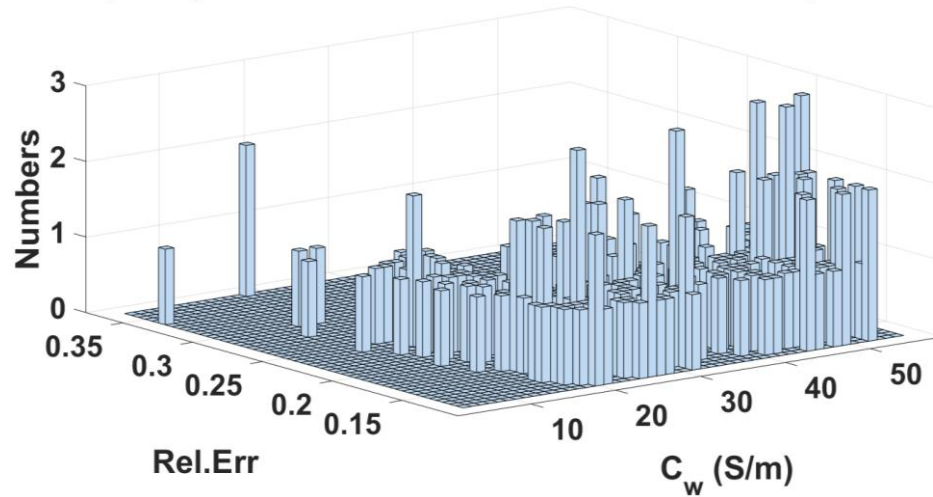


Figure 5.14 Frequency of inversion-derived  $S_w$  estimates for depth XX630.5 ft along with data misfit for 250 randomly generated sets of initial guesses of integrated model parameters.

### Frequency of inversion-derived water conductivity estimates



**Figure 5.15** Frequency of inversion-derived  $C_w$  estimates for depth XX630.5 ft along with data misfit for 250 randomly generated sets of initial guesses of integrated model parameters.

### 5.6 Validation of inversion-derived estimates

#### *Comparison of Water Saturation Estimates in BPS:*

Presence of thin-beds in Three Forks formation mandates the use of triaxial induction resistivity measurement and dielectric dispersion measurements for accurate water saturation estimation. The water saturation obtained from thin-beds analysis of triaxial induction resistivity logs agrees with water saturation reported from Dean Stark analysis in the lower part of Middle Bakken, upper part of Three Forks, and Lodgepole (Gary et al., 2015). In this well, the thin-beds in Three Forks formation, which has smaller size of pores indicated by NMR pore size distribution, cause erroneously high water saturation, which is shown in the comparison of water saturation obtained from traditional induction resistivity or Quanti-ELAN solver and core measurements. Our estimates of water saturation estimates are closer to the core measurements.

The water saturation estimated by Quanti-ELAN solver interpreted most parts of Lodgepole and Three Forks formation are 100% water-bearing zones, which is contrast

to values estimated by other logs and core measurements. The water saturation interpreted by induction logs via Archie equation indicates that most formations are 100% water-bearing except for Upper and Lower Bakken, which is totally inconsistent with core measurements as well as knowledge of the reservoir. The high frequency dielectric dispersion log is well-suited for the estimation of water saturation for the large contrast between the permittivity of water and other components of the formation (Donadille et al., 2016). The dielectric dispersion logs interpreted by the newly developed global search algorithm generate not an exact water saturation but a range of possible values within a desired accuracy in a user-specified search space and our estimation of water saturation shows a good agreement with core measurements.

Fig. 5.16 and 5.17 compares water saturation estimates obtained using various methods. Our estimates of water saturation and those obtained using the service company's dielectric inversion exhibit the best match with Dean-Stark's core water saturation in the Middle Bakken and Three Forks formations. However, in the part of Lodgepole, Scallion, and Upper Bakken formations, our estimates of water saturation are closer to those obtained from NMR logs, which disagrees with the extremely high estimates obtained using the service company's dielectric inversion. Both Lodgepole and Scallion are limestone formations with wide range of pore size distributions and natural fractures, which enhances the reservoir quality. Service company's dielectric inversion and NMR log interpretation generate quite different water saturation estimates. Interestingly, our estimates of water saturation in False Bakken are close to values obtain from induction logs, in contrast to service company's dielectric inversion-derived estimates and NMR interpreted water saturation, which indicate 65%-water-

saturated hydrocarbon-bearing zone. False Bakken is an organic-rich shale formation containing 2 to 4 weight percentage of organic carbon and has wide pore size distribution indicated by NMR T2 distribution curve in Fig. 5.17 in Track 9. Water saturation obtained by NMR logs, which have a relative shallow depth of investigation (DOI) ranging from 1 to 4 inch, is close to 0.2 water saturation unit in lower part of Lodgepole, False Bakken, Scallion, Upper Bakken, upper part of Middle Bakken and Lower Bakken. While in lower part of Middle Bakken, NMR interpreted water saturation is much higher than that in the upper part. In the middle part of Three Forks the NMR interpreted water saturation is high and close to the dielectric dispersion logs interpreted water saturation.

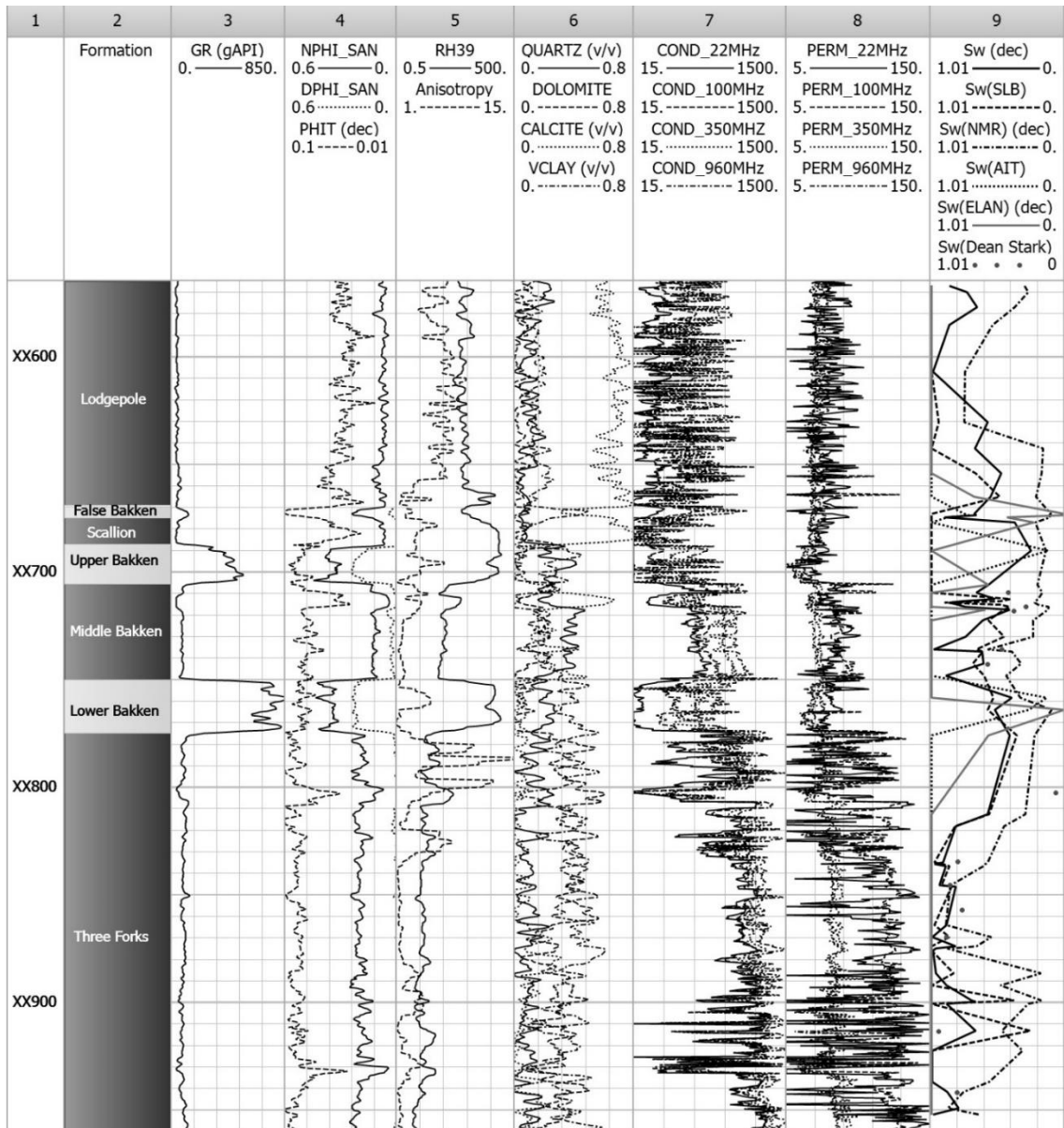


**Figure 5.16** Track 1 is the depth, Track 2 contains the top and bottom of various formations in BPS, Track 3 is the gamma ray, Track 4 contains the neutron porosity, density porosity and ELAN total porosity, Track 5 is the induction resistivity in horizontal direction and formation anisotropy, Track 6 contains the volume fractions of various minerals, Track 7 contains the dielectric dispersion conductivity logs at four frequencies, Track 8 contains the dielectric dispersion permittivity logs at four frequencies, and Track 9 contains water saturation estimated using various methods, wherein the red curve is water saturation estimate obtained using the proposed global-search inversion and the blue curve is that obtained by Schlumberger dielectric inversion.

### *Interpretation of the Newly Generated Logs:*

The estimated values of water saturation and formation water salinity in Middle Bakken are in the ranges of 0.5 to 1 and 205 kppm to 250 kppm, respectively. While the water salinity values (reported as formation water conductivity in logs) in other formations are much higher, in the range of 300 kppm to 360 kppm. Gary et al. (2015) observed that log-derived water saturation estimates correlate better with the Dean-Stark's core water saturation values computed using fluid salinity of 360 kppm and oil density of 0.802 g/cm<sup>3</sup>. In Bakken formation, water from wells producing oil is about an order of magnitude more saline than modern sea water (Peterman et al., 2014). Wang et al. (2012) also reported that the formation water salinity in Bakken can be as high as 150 kppm to 300 kppm. The measurements of macroscopic thermal neutron capture cross-section, referred as sigma measurements is strongly depend on the formation water salinity. Donadille et al (2016) developed a joint inversion of the dielectric dispersion and sigma measurements for more accuracy estimation of formation water salinity to solve the sensitivity loss of water conductivity (salinity) at high salinity for dielectric dispersion measurements. Nonetheless, the newly developed LMA-based inversion algorithm proposed in this paper introduces the scaling matrix  $\mathbf{W}_s$  to enable robust inversion without a loss in forward model sensitivity for high formation water conductivity, as demonstrated is the synthetic case discussed in this paper.

There is a good agreement between the formation water conductivity estimated by our dielectric dispersion interpretation method and obtained by the service company's dielectric inversion in Middle and Lower Bakken formation, as shown in Track 4 of Fig. 5.17. For other formations, our estimated formation water is more saline than that

obtained by service company’s dielectric inversion. Unlike the formation water salinity obtained by service company dielectric inversion in the Lodgepole formation that fluctuates a lot in a short depth interval, our estimates of water salinity exhibit a relatively stable trend within each formation.

The inversion-derived homogeneity index ( $\alpha$ ) obtained using our method indicates the presence of layering and heterogeneity in the Lower Three Forks and Middle Bakken formation. In agreement with the inversion-derived homogeneity index, Middle Bakken does exhibit a range of grain size and sorting from poorly sorted, argillaceous siltstone to moderately well sorted fine-grained sandstone. H-Index1 (Eq. 5.11) and H-Index2 (Eq. 5.12) are two formation homogeneity indices calculated based on mineral contents are illustrated in Fig. 5.17 in Track 6. A reduction in values of H-Index1 and H-Index2 from 1 indicates an increase in heterogeneity. In Fig. 5.17, homogeneity reduces with increase in depth as indicated by H-Index2 due to an increase in clay content. In Middle Bakken formation, inversion-derived and mineral-content-based homogeneity indices show similar trends and appear to be correlated. H-Index2 that indicates increase in heterogeneity due to increase in clay shows good correlation with  $\alpha$ . Moreover, the anisotropy calculated from RTScanner that indicates an increase in layering correlates well with  $\alpha$ .

$$H - Index1 = \frac{V_{Quartz}}{V_{Quartz} + V_{Calcite} + V_{Dolomite}} \dots\dots\dots(5.11)$$

$$H - Index2 = \frac{V_{Quartz} + V_{Calcite} + V_{Dolomite}}{V_{Quartz} + V_{Calcite} + V_{Dolomite} + V_{Clay}} \dots\dots\dots(5.12)$$

The inversion-derived cementation index ( $m$ ) indicates enhanced tortuosity and cementation in the Upper and Lower Bakken formations, which can be explained based

on the high kerogen content (>20%) and low values of effective porosity. The Upper and Lower Bakken formation also show wide range of pore size distribution illustrated in Fig. 5.17 in Track 9 that conforms with the enhanced tortuosity/cementation estimated by our proposed interpretation method. The  $m$  values are also high in False Bakken and Scallion formations that have a great volume fraction of narrow pore sizes, as shown in Fig. 5.17 Track 9. The inversion-derived  $m$  estimates increase with increase in isolated porosity, as shown in Fig. 5.17 Track 8. Fig. 5.18 reports the estimated water saturation, formation water conductivity, homogeneity index and cementation index ranges within a desired accuracy, which can be obtained by the method described in Fig. 5.4.



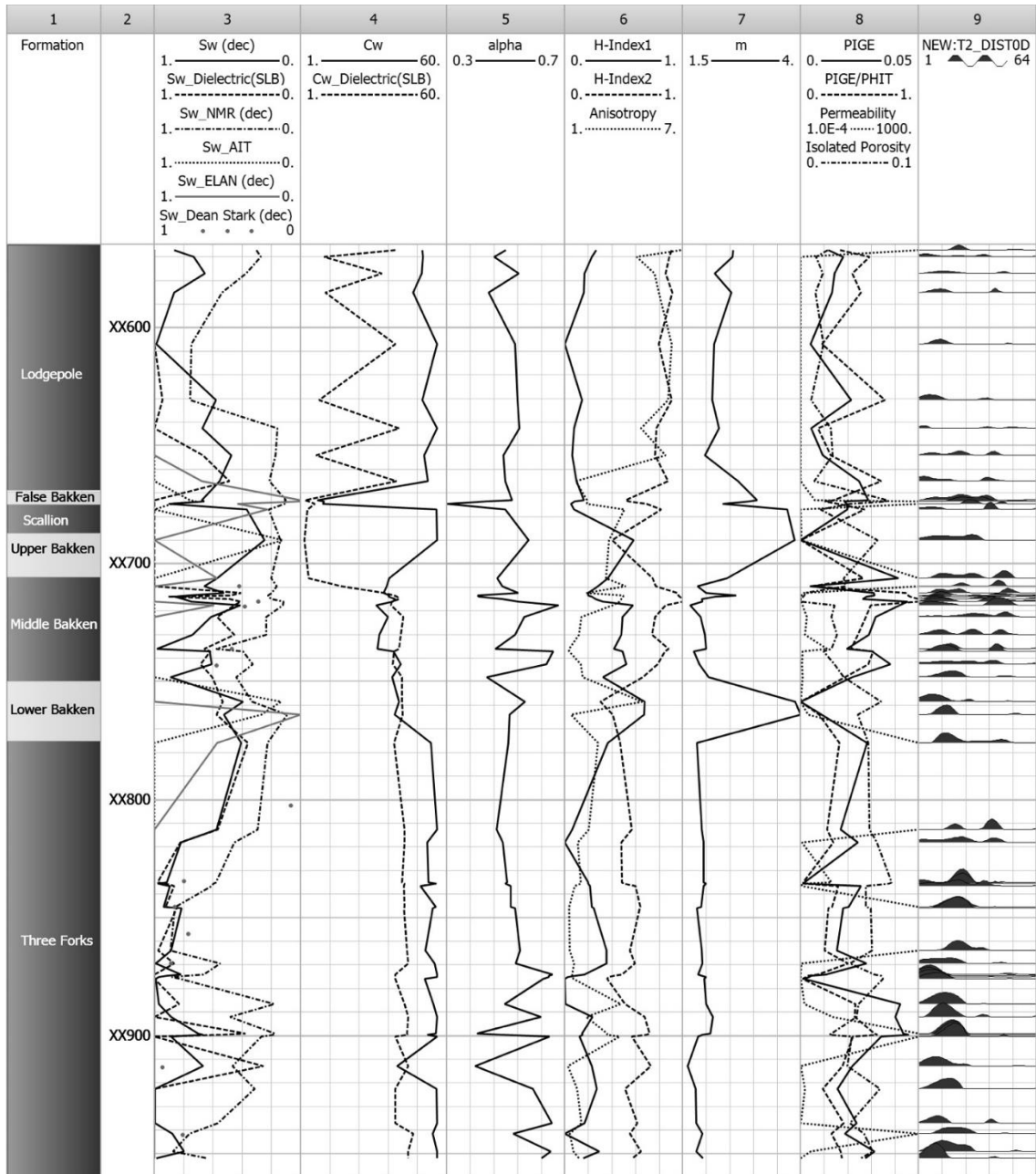
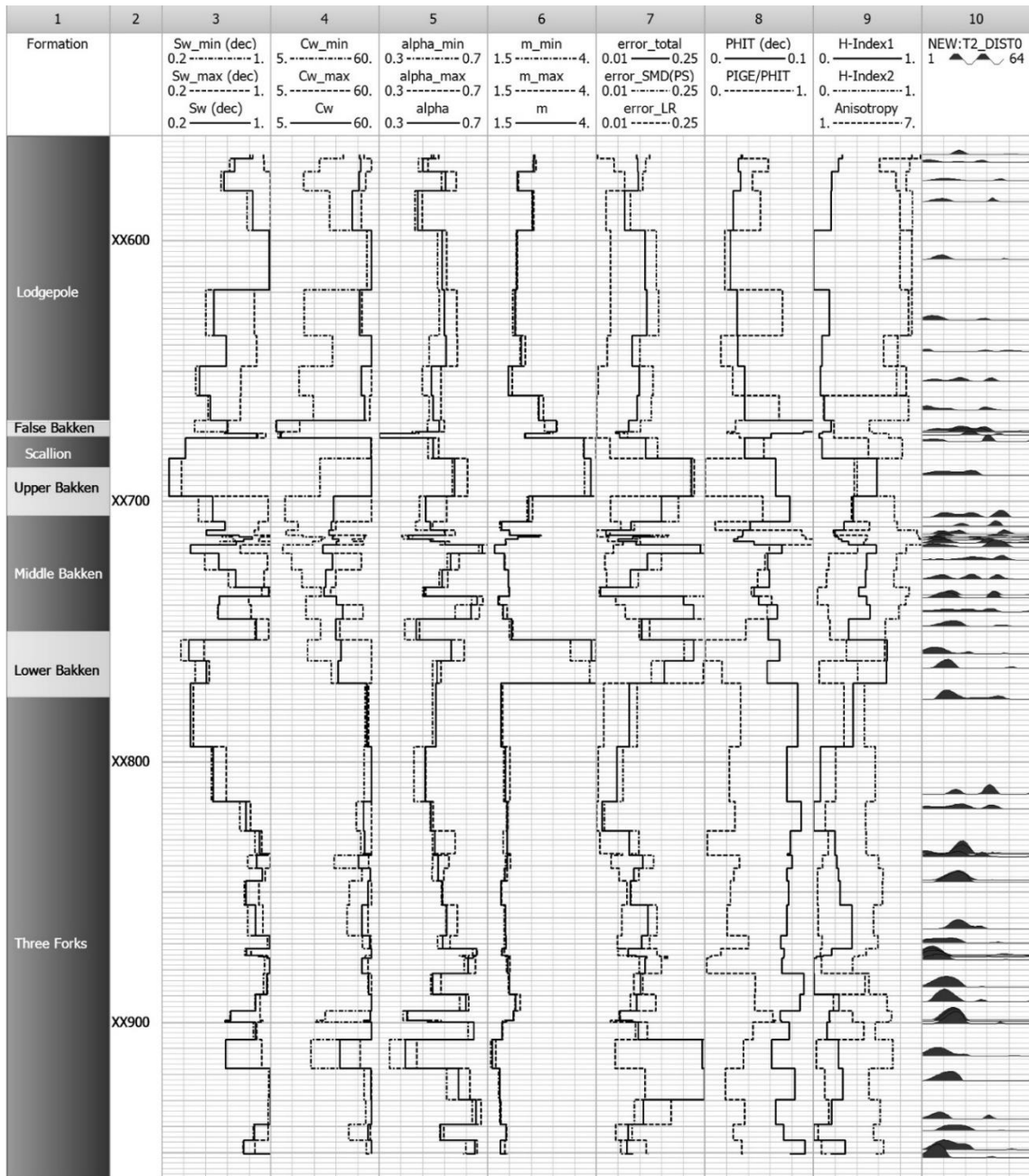


Figure 5.17 Track 1 contains the top and bottom of various formations in BPS, Track 2 is the depth, Track 3 contains water saturation estimated using various methods, wherein the red curve is water saturation estimate obtained using the proposed global-search inversion and the blue curve is that obtained by Schlumberger dielectric inversion, Track 4 is the formation water conductivity estimate and the black curve is that obtained by Schlumberger dielectric inversion, Track 5 is the inversion-derived homogeneity index, Track 6 is the formation homogeneity index calculated using mineral contents, Track 7 is the inversion-derived cementation index, Track 8 contains the permeability and isolated porosity (total-effective) of the formation, Track 9 is NMR T2 distribution.



**Figure 5.18** Track 1 contains the top and bottom of various formations in BPS, Track 2 is the depth, Track 3 contains estimated water saturation range within a desired accuracy, Track 4 is the range of estimated formation water conductivity, Track 5 is the range of estimated inversion-derived homogeneity index, Track 6 is the range of estimated cementation index, Track 7 contains the relative error of the inversion of field data using the integrated model and the relative error of the SMD and LR, respectively, Track 8 contains the total porosity and the ratio of effective porosity and total porosity of the formation, Track 9 is the formation homogeneity index calculated using mineral contents, Track 10 is NMR T2 distribution.

## Chapter 6: Conclusion

- (1) The unified inversion scheme is tested in few synthetic cases in which different relaxation models are coupled into the inversion scheme and results show that the proposed inversion scheme is robust for various levels of Gaussian noise ranging from 0% to 5%.
- (2) The unified inversion scheme is negligibly sensitive to the initial guesses of the relaxation-model parameters exhibiting convergence and accuracy up to 3-orders of magnitude of the initial guesses.
- (3) Consistent estimates of water saturation, surface conductance and average radius of clay grains, and formation water conductivity can be obtained by jointly processing the broadband effective permittivity and conductivity logging data acquired at 4 to 9 discrete log-acquisition frequencies.
- (4) The proposed open source dielectric dispersion log inversion-based interpretation method ensures consistent estimation of water saturation, formation water salinity, homogeneity index, and cementation index in clay-lean and clay-rich units. The proposed interpretation methodology is robust because (1) the inversion performs a global search, (2) the inversion is coupled to a forward model that integrates Lichtenecker–Rother model, Stroud-Milton-De model, and PS model, a mechanistic pyrite-clay dispersion model, and (3) a scaling matrix is implemented in the inversion scheme to improve the inversion results at high salinity and low porosity.
- (5) The estimated water saturation by the newly developed dielectric dispersion log interpretation method gets better agreements with values obtained by Dean Stark

analysis and NMR log interpretation as compared to the water saturation estimated by service company's dielectric interpretation. Nonetheless, for several depths, Schlumberger's inversion, NMR interpretation, Dean-Stark's core water saturation, and our inversion-derived estimates are in good agreement.

## References

- Al-Ameri, A., I. Bandyopadhyay, A. H. Balbaheeth, M. Bittar, A. Aki, and R. Essam, R., 2015, Improved formation evaluation with inversion techniques using logging while drilling azimuthal deep resistivity sensor – A Case Study: Presented at the 56<sup>th</sup> Annual Logging Symposium, SPWLA.
- Al Marzooq, A., T. Al Ghamdi, A. Salim, K. H. Sassi, M. Badri, and P. Saldungaray, 2014, An integrated workflow using spectroscopy, dielectric dispersion, and NMR for the characterization of shale plays—application to a Silurian shale: Presented at the 55<sup>th</sup> Annual Logging Symposium, SPWLA.
- Altman, R., B. Anderson, J. Rasmus, M. G. Lüling, 2008, Dielectric effects and resistivity dispersion on induction and propagation-resistivity logs in complex volcanic lithologies: a case study: Presented at the 49<sup>th</sup> Annual Logging Symposium, SPWLA.
- Aster, R., B. Borchers, and C. Thurber, 2005, Parameter estimation and inverse problems: Elsevier Academic.
- Binley, A., L. D. Slater, M. Fukes, and G. Cassiani, 2005, Relationship between spectral induced polarization and hydraulic properties of saturated and unsaturated sandstone: *Water Resources Research*, **41**(12), W12417.
- Börner, F. D., and J. H. Schön, 1991, A Relation between the Quadrature Component of Electrical Conductivity and the Specific Surface Area of Sedimentary Rocks: *The Log Analyst*, **32**(5), 612-613.
- Cao, Z., Y. Chang, and Y. Luo, 2005, Inversion study of spectral induced polarization based on improved genetic algorithm: *Progress in Electromagnetics Research Symposium (PIERS) Online*, **1**, 266–270;
- Chen, J., A. Kemna, and S. Hubbard, 2008, A comparison between Gauss-Newton and Markov-chain Monte Carlo-based methods for inverting spectral induced-polarization data for Cole-Cole parameters: *Geophysics*, **73**(6), F247-F259.
- Cole, K. S., and R. H. Cole, 1941, Dispersion and absorption in dielectrics I. Alternating current field: *Journal of Chemical Physics*, **1**, 341–351.
- de Lima, O. A. L., and M. M. Sharma, 1990, A grain conductivity approach to shaly sandstones: *Geophysics*, **55**(10), 1347-1356.
- de Lima, O. A., & Sharma, M. M. (1992). A generalized Maxwell-Wagner theory for membrane polarization in shaly sands. *Geophysics*, **57**(3), 431-440.
- Donadille, J. M., Leech, R., and Pirie, I., 2016, Water Salinity Determination Over an Extended Salinity Range Using a Joint Interpretation of Dielectric and Neutron

Cross-Section Measurements, Paper SPE-181366, presented at the SPE Annual Technical Conference and Exhibition, Dubai, UAE, 26-28 September. DOI: 10.2118/181366-MS.

- Fuller, B. D., & Ward, S. H. (1970). Linear system description of the electrical parameters of rocks. *IEEE Transactions on Geoscience Electronics*, 8(1), 7-18.
- Glinskikh, V. N., G. V. Nesterova, and M. I. Epov, 2014, Forward modeling and inversion of induction logs from shaly sand reservoirs using petrophysical conductivity models: *Russian Geology and Geophysics*, **55**(5), 793-799.
- Gurin, G., K. Titov, Y. Ilyin, and A. Tarasov, 2015, Induced polarization of disseminated electronically conductive minerals: A semi-empirical model: *Geophysics Journal International*, **200**, 1555-1565, doi: 10.1093/gji/ggu490.
- Havriliak, S., and S. Negami, 1966, A complex plane analysis of  $\alpha$ -dispersions in some polymer systems: *Journal of Polymer Science Part C: Polymer Symposia*, **14**, 99–117.
- Han, M., Cuadros, J., Suarez, C.A.P., Decoster, E., Faivre, O., Mosse, L., and Seleznev, N., 2012, Continuous Estimate of Cation Exchange Capacity from Log Data: A New Approach Based on Dielectric Dispersion Analysis, *Transactions, SPWLA 53rd Annual Logging Symposium*, Cartagena, Colombia, June 16-20.
- Han, Y., Misra, S., and Simpson, G, 2017a, Dielectric Dispersion Log Interpretation in Bakken Petroleum System: Presented at the SPWLA 58th Annual Logging Symposium.
- Han, Y., and Misra, S, 2017b, Improved water-saturation estimates derived from inversion-based interpretation of broadband electromagnetic dispersion logs in organic-rich shale formations: 87th Annual International Meeting, SEG, Expanded Abstracts, 3458-3462.
- Hizem, M., H. Budan, B. Deville, O. Faivre, L. Mosse, and M. Simon, 2008, Dielectric Dispersion – A new wireline petrophysical measurement: Presented at the Annual Technical Conference and Exhibition, SPE.
- Kemna, A., E. Räckers, and L. Dresen, 1999, Field applications of complex resistivity tomography: 69th Annual International Meeting, SEG, Expanded Abstracts, 331–334.
- Kemna, A., 2000, Tomographic inversion of complex resistivity: Theory and application: Ph.D. thesis, Ruhr-University Bochum.
- Kemna, A., H. M. Münch, K. Titov, E. Zimmermann, and H. Vereecken, 2005, Relation of SIP relaxation time of sands to salinity, grain size and hydraulic conductivity: 11th

European Meeting of Environmental and Engineering Geophysics, EAGE, Extended Abstracts, P054.

- Kemna, A., A. Binley, G. Cassiani, E. Niederleithinger, A. Revil, L. Slater, K. H. Williams, A. F. Orozco, F. H. Haegel, A. Hördt, S. Kruschwitz, V. Leroux, K. Titov, and E. Zimmermann, 2012, An overview of the spectral induced polarization method for near-surface applications: *Near Surface Geophysics*, **10**(6), 453-468.
- Kim, H. J., and Y. Kim, 2011, A unified transformation function for lower and upper bounding constraints on model parameters in electrical and electromagnetic inversion: *Journal of Geophysics and Engineering*, **8**(1), 21-26.
- Lazović, G., Z. Vosika, M. Lazarević, J. Simić-Krstić, and Đ. Koruga, 2014, Modeling of bioimpedance for human skin based on fractional distributed-order modified cole model: *FME Transactions*, **42**(1), 74-81.
- Lesmes, D. P., and S. P. Friedman, 2005, Relationships between the electrical and hydrogeological properties of rocks and soils: *Hydrogeophysics*, Springer, 87-128.
- Lin, Y., S. Gianzero, and R. W. Strickland, 1984, Inversion of induction logging data using the least squares technique: Presented at the 25<sup>th</sup> Annual Logging Symposium, SPWLA.
- Little, J. D., D. R. Julander, L. C. Knauer, J. T. Aultman, J. L. Hemingway, 2010, Dielectric dispersion measurements in California heavy oil reservoirs: Presented at the 51<sup>st</sup> Annual Logging Symposium, SPWLA.
- Loke, M. H., 2001, Tutorial: 2-D and 3-D electrical imaging surveys: Course Notes for USGS Workshop 2-D and 3-D Inversion and Modeling of Surface and Borehole Resistivity Data, Torrs, CT.
- Marshall, D. J., and T. R. Madden, 1959, Induced polarization, a study of its causes: *Geophysics*, **24**(4), 790-816.
- Mezzatesta, A. G., C. C. Payton, K. M. Strack, and L. A. Tabarovsky, 1994, Simultaneous inversion of galvanic and induction logging measurements to improve resolution: Presented at the Latin American and Caribbean Petroleum Engineering Conference. doi:10.2118/26976-MS.
- Misra, S., C. Torres-Verdín, D. Homan, and J. Rasmus, 2015, Complex electrical conductivity of mudrocks and source-rock formations containing disseminated pyrite: Presented at the Unconventional Resources Technology Conference.
- Misra, S., C. Torres-Verdín, A. Revil, J. Rasmus, and D. Homan, 2016a, Interfacial polarization of disseminated conductive minerals in absence of redox-active species—Part 1: Mechanistic model and validation: *Geophysics*, **81**(2), E139-E157.

- Misra, S., C. Torres-Verdín, A. Revil, J. Rasmus, and D. Homan, 2016b, Interfacial polarization of disseminated conductive minerals in absence of redox-active species—Part 2: Effective electrical conductivity and dielectric permittivity: *Geophysics*, **81**(2), E159-E176.
- Misra, S., M. G. Luling, J. Rasmus, D. Homan, and T. D. Barber, 2016c, Dielectric effects in pyrite-rich clays on multi-frequency induction logs and equivalent laboratory core measurements: Presented at the SPWLA 57<sup>th</sup> Annual Logging Symposium.
- Misra, S., and Y. Han, 2016a, Petrophysical interpretation of multi-frequency electromagnetic measurements in clay- and conductive-mineral-rich mudrocks: Presented at the Unconventional Resources Technology Conference.
- Misra, S., and Y. Han, 2016b, Improved oil-in-place estimates in clay- and pyrite-bearing shales based on inversion of multi-frequency electromagnetic measurements: Presented in AAPG Eastern Section Meeting.
- Pelton, W. H., S. H. Ward, P. G. Hallof, W. R. Sill, and P. H. Nelson, 1978, Mineral discrimination and removal of inductive coupling with multifrequency IP: *Geophysics*, **43**(3), 588-609.
- Peterman, Z. E., Thamke, J., Neymark, L.A., Oliver, T.A., and Futa, K., 2014, Bakken Formation Water Salinity and the Role of Ion Filtration, Williston Basin, presented at Rocky Mountain (66th Annual) and Cordilleran (110th Annual) Joint Meeting, Bozeman, USA, May 19-21.
- Pirrone, M., N. Bona, M. T. Galli, F. Pampuri, O. Faivre, M. Han, M. Hizem, and L. Mosse, 2011, An innovative dielectric dispersion measurement for better evaluation of thin layered reservoirs applied in a south Italy well: Presented at the 10<sup>th</sup> Offshore Mediterranean Conference and Exhibition.
- Revil, A., and N. Florsch, 2010, Determination of permeability from spectral induced polarization in granular media: *Geophysical Journal International*, **181**(3), 1480-1498.
- Revil, A., 2012, Spectral induced polarization of shaly sands: Influence of the electrical double layer: *Water Resources Research*, **48**(2), W02517, doi: 10.1029/2011WR011260.
- Revil, A., J. D. Eppehimer, M. Skold, M. Karaoulis, L. Godinez, and M. Prasad, 2013, Low-frequency complex conductivity of sandy and clayey materials: *Journal of Colloid and Interface Science*, **398**, 193–209.
- Revil, A., Florsch, N., & Mao, D. (2015). Induced polarization response of porous media with metallic particles—Part 1: A theory for disseminated semiconductors. *Geophysics*.



- Revil, A., Murugesu, M., Prasad, M., & Le Breton, M. (2017). Alteration of volcanic rocks: A new non-intrusive indicator based on induced polarization measurements. *Journal of Volcanology and Geothermal Research*.
- Roy, I. G., 1999, An efficient non-linear least-squares 1D inversion scheme for resistivity and IP sounding data: *Geophysical Prospecting*, **47**, 527-550.
- Sabouroux, P., and D. Ba, 2011, Epsimu, a tool for dielectric properties measurement of porous media: Application in wet granular materials characterization: *Progress in Electromagnetic Research B*, **29**, 191-207.
- Schmitt, D. P., Al-Harbi, A., Saldungaray, P., Akkurt, R., and Zhang, T., 2011, Revisiting Dielectric Logging in Saudi Arabia: Recent Experiences and Applications in Development and Exploration Wells, Paper SPE-149131, presented at SPE/DGS Saudi Arabia Section Technical Symposium and Exhibition, Al-Khobar, Saudi Arabia, 15-18 May.
- Sen, P. N., C. Scala, and M. H. Cohen, 1981, A self-similar model for sedimentary rocks with application to the dielectric constant of fused glass beads: *Geophysics*, **46**(5), 769-783.
- Stroud, D., G. W. Milton, and B. R. De, 1986, Analytical model for the dielectric response of brine-saturated rock: *Physical Review B*, **34**, 5145-5153.
- Schurr, J. M., 1964, On the theory of the dielectric dispersion of spherical colloidal particles in electrolyte solution: *The Journal of Physical Chemistry*, **68**(9), 2407-2413.
- Seigel, H. O., 1959, Mathematical formulation and type curves for induced polarization: *Geophysics*, **24**(3), 547-565.
- Simpson, G., Hohman, J., Pirie, I., and Horkowitz, J., 2015, Using Advanced Logging Measurements to Develop a Robust Petrophysical Model for the Bakken Petroleum System, Transactions, SPWLA 56th Annual Logging Symposium, Long Beach, California, USA, July 18-22.
- Slater, L. D., D. Ntarlagiannis, and D. Wishart, 2006, On the relationship between induced polarization and surface area in metal-sand and clay-sand mixtures: *Geophysics*, **71**(2), A1-A5.
- Šumi, F., 1965, Prospecting for non-metallic minerals by induced polarization: *Geophysical Prospecting*, **13**(4), 603-616.
- Tarasov, A., and K. Titov, 2013, On the use of the Cole-Cole equations in spectral induced polarization: *Geophysical Journal International*, **195**(1), 352-356.

- Torres-Verdin, C., V. L. Druskin, S. Fang, L. A. Knizhnerman, and A. Malinverno, 2000, A dual-grid nonlinear inversion technique with applications to the interpretation of dc resistivity data. *Geophysics*, **65**(6), 1733-1745.
- Thiel, M., D. Omeragic, and T. Habashy, 2012, Robust nonlinear parametric Gauss-Newton inversion for well-logging applications: Presented at the SEG Annual Meeting.
- Wang, D., Butler, R., Zhang, J., and Seright, R., 2012, Wettability Survey in Bakken Shale using Surfactant Formulation Imbibition, SPE-153853, presented at SPE Improved Oil Recovery Symposium, Tulsa, Oklahoma, USA, 14-18 April.
- Wong, J., 1979, An electrochemical model of the induced-polarization phenomenon in disseminated sulfide ores: *Geophysics*, **44**(7), 1245-1265.
- Xiang, J., N. B. Jones, D. Cheng, and F. S. Schlindwein, 2001, Direct inversion of the apparent complex-resistivity spectrum: *Geophysics*, **66**(5), 1399-1404.
- Zhou, J., H. Li, M. Rabinovich, and B. D'Arcy, 2016, Interpretation of azimuthal propagation resistivity measurements: modeling, inversion, application and discussion: Presented at the 57<sup>th</sup> Annual Logging Symposium, SPWLA.

## Appendix: Nomenclature

$\varepsilon^*$	=	Complex permittivity
$\varepsilon_\infty$	=	High-frequency permittivity
$\varepsilon_0$	=	Low-frequency permittivity
$\varepsilon_w^*$	=	Complex water permittivity
$\varepsilon_o$	=	Hydrocarbon permittivity
$\alpha$	=	Exponent in Havriliak-Negami model
$\beta$	=	Exponent in Havriliak-Negami model
$\Phi$	=	Total porosity of geomaterials
$\Phi_w$	=	Water-filled porosity
$\tau$	=	Central relaxation time (s)
$f$	=	Frequency of EM measurement (Hz)
$\omega$	=	Angular frequency of EM measurement (rad/s)
$Z^*$	=	Complex impedance
$R_0$	=	DC (low frequency) resistance ( $\Omega$ )
$m$	=	Chargeability
$c$	=	Cole-Cole model exponent
$\rho^*$	=	Complex resistivity
$\rho_0$	=	Low-frequency resistivity
$\sigma^*$	=	Complex conductivity
$\sigma_0$	=	Low-frequency conductivity
$\sigma_\infty$	=	High-frequency conductivity
$s_w$	=	Water saturation

$C_w$	=	Brine conductivity
$\lambda_c$	=	Surface conductance of clay
$r_c$	=	Radius of clay
$r_i$	=	Radius of pyrite
$R(\mathbf{m}, \omega)$	=	Relaxation model
$\mathbf{m}$	=	Model parameter vector
$\mathbf{m}^{\text{est}}$	=	Estimated model parameter vector
$\mathbf{m}^k$	=	Model parameter vector computed at the $k$ -th iteration
$\Delta\mathbf{m}^k$	=	Correction vector
$\mathbf{D}^{\text{mod}}(\mathbf{m})$	=	Modeled data vector
$\mathbf{D}^{\text{mod}}(\mathbf{m}^{\text{est}})$	=	Modeled data vector based on estimated model parameter vector
$\mathbf{D}^{\text{meas}}$	=	Measured data vector
$\mathbf{Perm}^{\text{meas}}$	=	Log-derived effective permittivity
$\mathbf{Cond}^{\text{meas}}$	=	Log-derived conductivity
$\mathbf{Perm}^{\text{mod}}(\mathbf{m})$	=	Modeled effective permittivity
$\mathbf{Cond}^{\text{mod}}(\mathbf{m})$	=	Modeled conductivity
$C(\mathbf{m})$	=	Quadratic cost function
$\mathbf{F}(\mathbf{m})$	=	Cost function vector
$f_i(\mathbf{m}^k)$	=	Individual components of cost function vector
$\mathbf{J}(\mathbf{m}^k)$	=	Jacobian matrix of $\mathbf{F}(\mathbf{m}^k)$
$\mathbf{I}$	=	Identity matrix
$\mathbf{w}$	=	Weight factor vector
$\mathbf{W}_d$	=	Data weight matrix

- $\mathbf{W}_s$  = Scaling matrix  
 $\sigma$  = Standard deviation vector  
 $\lambda$  = Damping parameter  
 $\nu$  = Constant factor

### Subscripts

- $l$  = Size of model parameter vector  
 $n$  = Size of data vector  
 $i$  = One of the  $n$  frequencies of measurements  
 $r$  = Relative

### Superscripts

- $k$  = Iteration number  
mod = Modeled  
meas = Measured  
est = Estimated